

# Spectroscopy and modeling of $^{171}\text{Yb}$ Rydberg states for high-fidelity two-qubit gates

Michael Peper,<sup>1</sup> Yiyi Li,<sup>1</sup> Daniel Y. Knapp,<sup>1,2,\*</sup> Mila Bileska,<sup>1,2</sup> Shuo Ma,<sup>1,2</sup> Genyue Liu,<sup>1</sup> Pai Peng,<sup>1</sup> Bichen Zhang,<sup>1</sup> Sebastian P. Horvath,<sup>1</sup> Alex P. Burgers,<sup>1,†</sup> and Jeff D. Thompson<sup>1,‡</sup>

<sup>1</sup>*Department of Electrical and Computer Engineering,  
Princeton University, Princeton, NJ 08544, USA*

<sup>2</sup>*Department of Physics, Princeton University, Princeton, NJ 08544, USA*

(Dated: June 4, 2024)

We present multichannel quantum defect (MQDT) models for highly excited  $^{174}\text{Yb}$  and  $^{171}\text{Yb}$  Rydberg states with  $L \leq 2$ . The models are developed using a combination of existing literature data and new, high-precision laser and microwave spectroscopy in an atomic beam, and validated by detailed comparison with experimentally measured Stark shifts and magnetic moments. We then use these models to compute interaction potentials between two Yb atoms, and find excellent agreement with direct measurements in an optical tweezer array. From the computed interaction potential, we identify an anomalous Förster resonance that likely degraded the fidelity of previous entangling gates in  $^{171}\text{Yb}$  using  $F = 3/2$  Rydberg states. We then identify a more suitable  $F = 1/2$  state, and achieve a state-of-the-art controlled-Z gate fidelity of  $\mathcal{F} = 0.994(1)$ , with the remaining error fully explained by known sources. This work establishes a solid foundation for the continued development quantum computing, simulation and entanglement-enhanced metrology with Yb neutral atom arrays.

## I. INTRODUCTION

Rydberg-mediated interactions between neutral atoms in optical tweezer arrays are enabling for quantum computing, simulation and quantum-enhanced metrology [1–4]. To realize high-fidelity operations, a detailed understanding of the properties of the Rydberg states and their interactions is required. Alkali atoms such as Rb or Cs can be described by simple quantum defect models, which have been validated by extensive spectroscopy [5–11]. This allows the wavefunctions, and in turn, matrix elements, interaction potentials and decay rates to be computed [12–14]. Experimental studies have confirmed the predicted interaction potentials [15–17] and decay rates [18–20]. A particularly stringent test of the interaction model comes from spectroscopy of so-called macrodimer states [21–24].

Many recent experiments have focused on divalent alkaline-earth-like atoms, in particular Sr [25–28] and Yb [29–32]. Tweezer arrays of  $^{88}\text{Sr}$  Rydberg atoms have been used to study many-body dynamics [33, 34] and entanglement-enhanced optical clocks [35, 36]. On the other hand,  $^{171}\text{Yb}$  is ideal for use as a qubit for quantum computing, with demonstrated long coherence times for the pure nuclear spin qubit with  $I = 1/2$  [30–32], mid-circuit measurement and atom reloading [37, 38] and hardware efficient error correction strategies [39, 40].

A challenge to the continued development of divalent atomic qubits, particularly those based on  $^{171}\text{Yb}$ , is the

relative lack of spectroscopic information and models for the behavior of the Rydberg states. The Rydberg states of divalent atoms are more complex than alkali atoms, because of the presence of singlet and triplet Rydberg series, interactions between series converging to other ionization thresholds (*i.e.*, series perturbers), and hyperfine coupling (in the case of isotopes with nuclear spin  $I > 0$ , such as  $^{87}\text{Sr}$  and  $^{171}\text{Yb}$ ). These states can be described in the framework of multichannel quantum defect theory (MQDT) [41, 42], which in turn allows the computation of matrix elements, interaction potentials and decay rates [43, 44].

Single-channel approximations have been used to predict interaction potentials in both  $^{174}\text{Yb}$  and  $^{88}\text{Sr}$ , which both have no nuclear spin ( $I = 0$ ) [43, 45]. Moreover, relatively complete MQDT descriptions of  $^{88}\text{Sr}$  have been developed and used to study lifetimes and branching ratios [43], and MQDT models have been developed to fit spectroscopic data for certain Rydberg series in  $^{174}\text{Yb}$  [46–50]. The energies of certain Rydberg series in  $^{87}\text{Sr}$  ( $I = 9/2$ ) have also been determined [51] and used to predict  $C_6$  coefficients using an MQDT formalism [52]. However, to the best of our knowledge, there is no comprehensive spectroscopy or MQDT model of the Rydberg states of  $^{171}\text{Yb}$ , and no MQDT interaction models for divalent atoms have been experimentally verified at a level approaching the precision of alkali atom models.

In this article, we present four main results. First, we present refined MQDT models for the Rydberg states of  $^{174}\text{Yb}$  with  $L \leq 2$  (Section II). This set of states is sufficient to accurately predict the interactions and polarizability of the  $L = 0$  states that are most frequently used in experiments. This extends prior work [46, 49, 50, 53–61] by incorporating new spectroscopic measurements and re-fitting all of the MQDT models simultaneously with a global fit for improved consistency and accuracy. Furthermore, we determine singlet-triplet mixing angles by comparison to experimental measurements of

\* Current address: Department of Physics and Astronomy, Laser-Lab, Vrije Universiteit Amsterdam, de Boelelaan 1081, 1081 HV Amsterdam, The Netherlands

† Current address: Department of Electrical and Computer Engineering, College of Engineering, University of Michigan, Ann Arbor, MI 48109, USA.

‡ jdthompson@princeton.edu

the static dipole polarizability, which are undetermined by the state energies alone [62]. We find excellent agreement with measured Rydberg state energies, polarizabilities and magnetic moments.

Next, we extend these models to describe  $^{171}\text{Yb}$  states with  $L \leq 2$  by including the hyperfine interaction (Sec. III). The models are refined and validated by comparison to extensive laser and microwave spectroscopy of  $^{171}\text{Yb}$  Rydberg states from an atomic beam apparatus. We also test the MQDT model matrix elements by comparison to measured static dipole polarizabilities and magnetic moments, finding excellent agreement.

Third, we use the  $^{171}\text{Yb}$  MQDT models to compute the interaction potential for Rydberg atom pairs, which we verify against direct measurements using pairs of atoms in an optical tweezer array (Sec. IV). We show that the  $^{171}\text{Yb}$   $F = 3/2$  Rydberg state that was previously used to implement entangling gates [31, 40] has a surprisingly small Förster defect ( $< 10$  MHz) over a large range of effective principal quantum number  $\nu$ . This gives rise to an imperfect blockade, and we conjecture that it is responsible for the discrepancy between the measured ( $\mathcal{F} = 0.980(1)$ ) and predicted ( $\mathcal{F}_{th} = 0.989$ ) gate error in Ref. [40].

Finally, in Sec. V we leverage these models to predict that certain  $F = 1/2$  states should have a larger Förster defect, giving rise to a cleaner blockade and improved gate fidelity. We then experimentally demonstrate improved gates with  $\mathcal{F} = 0.994(1)$ . Importantly, the dominant remaining errors are well-understood (arising from Rydberg state decay and Doppler shifts), which is promising for future improvements in gate fidelity with increased laser power.

This work solidifies the foundation for future quantum computing, simulation and quantum-enhanced metrology applications of  $^{171}\text{Yb}$  Rydberg atoms. The same approach may be applied to other atoms with multiple interacting Rydberg series, including  $^{87}\text{Sr}$  [63], or lanthanide atoms such as Ho [64] or Er [65].

## II. MULTICHANNEL QUANTUM DEFECT MODEL OF $^{174}\text{Yb}$

Fig. 1a illustrates the basic principle of MQDT, in the context of  $^{174}\text{Yb}$  (the most abundant isotope, with nuclear spin  $I = 0$ ). The ground state of  $^{174}\text{Yb}$  has the electronic configuration  $[\text{Xe}]4f^{14}6s^2$ , and the states of primary interest are singly-excited states  $[\text{Xe}]4f^{14}6snl$ , where  $n, l$  are the principal quantum number and orbital angular momentum of the excited electron (the Xe core and  $4f^{14}$  electrons are omitted henceforth, unless otherwise noted). These states are approximately described in  $LS$  coupling by the term symbol  $^{2S+1}L_J$  with total electron spin  $S = \{0, 1\}$ ,  $L = l$ , and total electronic angular momentum  $J$ . In single-channel quantum defect theory, these states form isolated series converging to the ground state of the  $^{174}\text{Yb}^+$  ion with the electron

configuration  $6s^1$ . The energy of the states in this series is  $E_n = I_{6s} - R/\nu_{6s}^2$ , where  $\nu_{6s} = n - \mu$  is the effective quantum number, and  $\mu(n, L, J)$  is the quantum defect that captures the interaction with the core for that series, with only weak dependence on  $n$ .

This picture is complicated by low-lying excited states in  $\text{Yb}^+$ , which give rise to doubly-excited states in the energy range of interest (*e.g.*,  $[\text{Xe}]4f^{14}6pnl$ ). These doubly-excited states are part of additional Rydberg series converging to higher thresholds (Fig. 1a), and couple to the singly-excited Rydberg states of interest through configuration interactions, which mix series with the same  $J$  and parity. This alters the energy spectrum through level repulsion (*i.e.*, series perturbers), which gives rise to sharp variations in  $\mu$  with  $n$ , and corresponding modifies the wavefunctions needed to compute quantities of interest such as matrix elements, interactions and lifetimes. This effect can be described quantitatively using MQDT, treating the interacting series as a set of coupled channels and parameterizing the interactions with a small number of mixing angles or a  $K$ -matrix [66, 67]. MQDT is essential to accurately explain the Rydberg series of atoms with low-lying core excited states such as noble gases [62, 68–71], divalent atoms [43, 72–75], or lanthanides [64, 65, 76], as well as more complex systems like molecules [42, 77, 78]. Compared to lighter divalent atoms such as Sr, Yb has a relatively larger number of contributing channels, because of the density of low-energy excitations of the ion core to states with electron configuration  $4f^{13}5d6s$ . We outline the mathematical details of the MQDT approach in Appendix A.

In the case of  $^{174}\text{Yb}$ , prior studies have reported spectroscopy and MQDT models of  $S, P, D$  and  $F$  Rydberg series [29, 46–49] (a comprehensive summary can be found in Ref. [50]). We have improved these models by performing additional microwave spectroscopy of some  $P$  Rydberg states between  $n = 30 - 50$  (using an atomic beam apparatus, App. B), and performing a simultaneous fit of all models to all of the available spectroscopic data, which is able to better leverage the higher precision of microwave measurements between Rydberg states. A summary of the model predictions and spectroscopic energy levels for the  $S$  and  $P$  states is shown in Fig. 1b. While certain series are relatively flat and could be adequately described by a single-channel approximation in the limit of large  $n$ , we note that the  $^3P_0$  and  $^3P_1$  series are very strongly perturbed, and require a full MQDT treatment.

Our main contribution to the  $^{174}\text{Yb}$  models is to incorporate singlet-triplet mixing in the  $L = 1$  and  $L = 2$  Rydberg series. Interactions between series converging to the same ionization threshold do not affect the energy spectrum [62], but can significantly alter matrix elements. To determine the singlet-triplet mixing between the  $^1P_1$  and  $^3P_1$  series, we measure the static dipole polarizability for the  $^1S_0$  series, near its crossing with  $^3P_1$  (Fig. 1c). By adjusting the single-triplet mixing angle in the MQDT model, we can accurately capture the resonance-like fea-

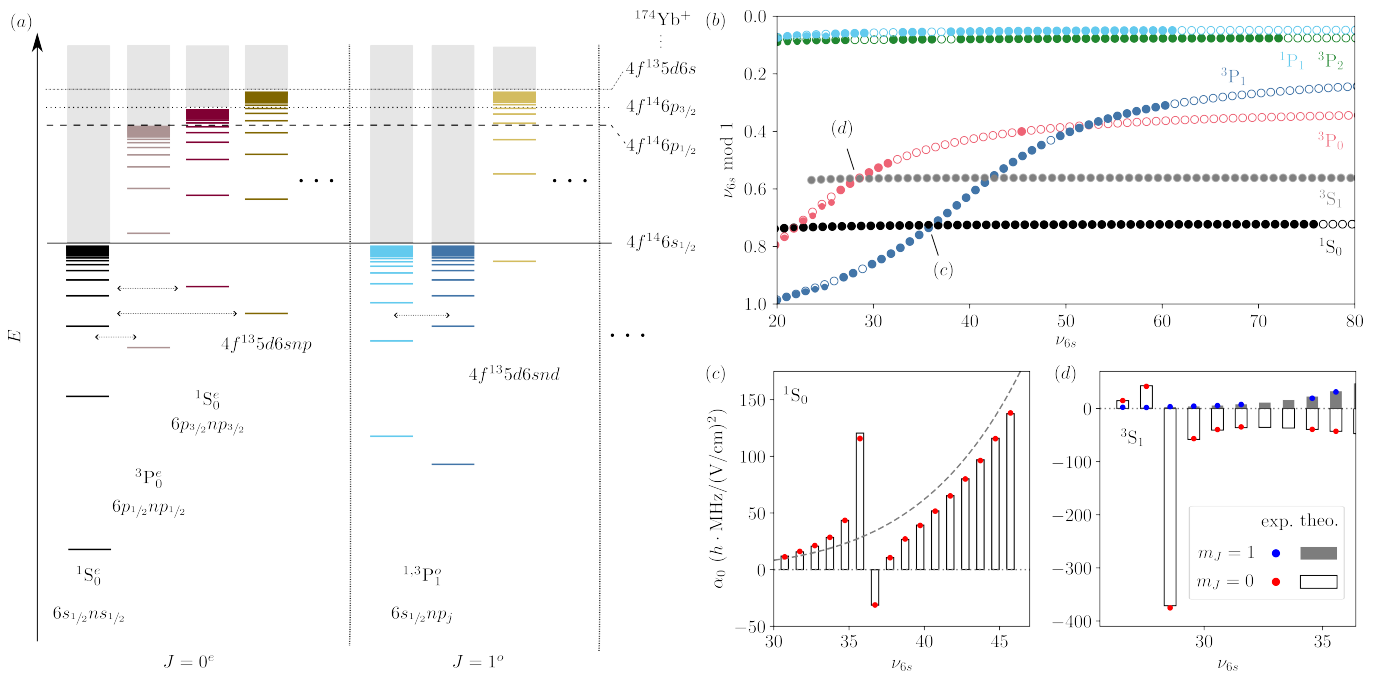


Figure 1. (a) Schematic diagram of several Rydberg series  $^{174}\text{Yb}$ , illustrating the principle of MQDT. Both singly-excited ( $6s_{1/2}nl$ ) and doubly-excited (e.g.,  $6pnl$ ) series are included, converging to different thresholds corresponding to excited states of the  $^{174}\text{Yb}^+$  ion (note that in this schematic diagram, the energy level spacings are not to scale, and only the subset of channels most relevant for the presented MQDT models are included). The Rydberg series are sorted by total angular momentum  $J$  and parity (even/odd denoted by  $e/o$  superscripts).  $LS$  coupling term symbols are written where possible (i.e.,  $^1S_0$ ). Configuration interactions mix series with the same  $J$  and parity, as indicated by the horizontal arrows. (b) Lu-Fano-like plot of the  $L = 0$  and  $L = 1$  Rydberg series of  $^{174}\text{Yb}$ , showing the fractional part of the quantum defect ( $\nu_{6s} \bmod 1$ ) as a function of the effective principal quantum number,  $\nu_{6s}$ . The open circles show the eigenstates predicted by the MQDT model, while the filled circles show experimentally determined energies. (c) Static dipole polarizability  $\alpha_0$  of the  $n^1S_0$  series close to a level crossing with the  $n^3P_1$  series (red points: experiment, bars: MQDT prediction). The gray, dashed line indicates the expected  $\nu^7$  scaling in the absence of singlet-triplet mixing. (d) Static dipole polarizability of the  $n^3S_1$  series near a crossing with  $n^3P_0$ . The experimental data for the polarizability of the  $m_J = 0$  (red) and  $m_J = 1$  (blue) states agrees well with the theoretical predictions from the MQDT model.

ture, which deviates strongly from the usual  $\nu^7$  polarizability trend [79]. The final model predicts a triplet character of the  $^1P_1$  Rydberg series that varies between 6.30(3)% for  $n = 40$  and 2.96(16)% for  $n = 100$ , which is consistent with previous estimates based on measurements of diamagnetic shifts [57], but considerably more precise (Appendix D 2).

We perform a similar analysis for the mixing angle between the  $^1D_2$  and  $^3D_2$  series, using literature data for the magnetic moments of these states [59]. We find a triplet character of  $n^1D_2$  of approximately 15% (Appendix D 5).

As an additional check of the model, we characterize the scalar and tensor polarizability of the  $n^3S_1$  Rydberg series near its crossing with  $^3P_0$ , finding excellent agreement (Fig. 1d).

A complete tabulation of the model parameters is presented in Tab. II to VI, and the compiled spectroscopic data is available in Tabs. XII to XXIII. A more detailed description of the developed MQDT models is presented in Appendix D.

### III. MQDT MODEL OF $^{171}\text{Yb}$

In contrast to  $^{174}\text{Yb}$ ,  $^{171}\text{Yb}$  has a non-zero nuclear spin of  $I = 1/2$ . The absence of hyperfine coupling in low-lying  $J = 0$  manifolds (i.e.,  $^1S_0$  or  $^3P_0$ ) results in an ideal nuclear spin qubit [30, 31, 63]. Counterintuitively, the Rydberg states of  $^{171}\text{Yb}$  have a fairly strong hyperfine coupling, which arises from the interplay of hyperfine coupling in the  $\text{Yb}^+$  core and the exchange interaction between the core and Rydberg electrons. This coupling is necessary to implement entangling gate operations on the pure nuclear spin qubit [31, 40], but also significantly complicates the description of the Rydberg series [51, 70, 80, 81]. We note that the role of hyperfine coupling in  $^{171}\text{Yb}$  qubits is almost opposite to alkali atoms, where the ground state has strong hyperfine coupling, while direct hyperfine coupling of the Rydberg state can be largely neglected [82].

In the context of MQDT, hyperfine effects can be represented as a coupling between multiple Rydberg series with the same parity and total angular momentum  $F$ ,

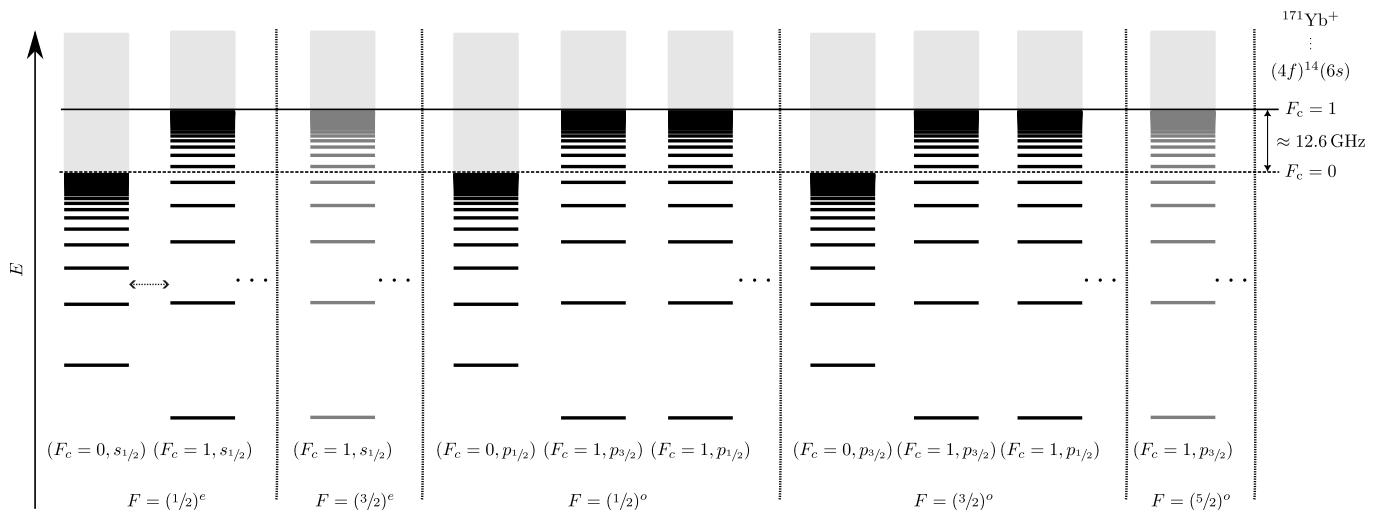


Figure 2. Schematic energy level diagram of the  $L = 0$  and  $L = 1$  Rydberg states of  $^{171}\text{Yb}$ , indicating Rydberg series converging to the two hyperfine states of the  $^{171}\text{Yb}^+ 6s^2S_{1/2}$  ground state. Channels converging to electronically excited states of the ion core are not shown, but are included in the MQDT models. The series are labeled by their good quantum numbers  $F$  and parity (labelled as  $e$  or  $o$ ).

converging to different thresholds corresponding to the hyperfine-split ion core states (Fig. 2). In the case of  $^{171}\text{Yb}^+$ , the  $6s^2S_{1/2}$  ground state is split into two hyperfine states with total angular momentum  $F_c = 0$  and  $F_c = 1$ , separated by  $A_{HF} = 12.642812$  GHz [83]. For the range of  $\nu$  relevant for quantum information applications ( $40 \lesssim \nu \lesssim 100$ ), the hyperfine interaction energy is comparable to the spacing between principal quantum levels, resulting in strong channel mixing when there is more than one series with the same  $F$  and parity [84]. For example, the  $6sns$  states in  $^{171}\text{Yb}$  give rise to two coupled  $F = 1/2$  series converging to  $F_c = 0$  and  $F_c = 1$ , and a single  $F = 3/2$  series converging to the  $F_c = 1$  threshold.

The effect of hyperfine-induced channel mixing has been experimentally studied previously in several species, including  $^{87}\text{Sr}$  [51, 81, 85, 86] and  $^{135,137}\text{Ba}$  [47, 73]. However, only a small number of measurements of  $^{171}\text{Yb}$  Rydberg states have been reported [31, 87–89].

Here, we present a spectroscopic characterization of the Rydberg states of  $^{171}\text{Yb}$  with  $L \leq 2$ , obtained by laser and microwave spectroscopy, as well as comprehensive MQDT models for these states, using the formalism introduced in Refs. [44, 86]. The MQDT models are based on those for  $^{174}\text{Yb}$ , extended to incorporate channels converging to the hyperfine-split states using a frame transformation. However, all model parameters are re-fit directly to the  $^{171}\text{Yb}$  spectroscopic data. The results for  $L = 0$  and  $L = 1$  states are presented in this section, and the models for the  $L = 2$  states and additional spectroscopic data are presented in Appendix E. In Sec. III C, we demonstrate the accuracy of the model by measuring the polarizability of selected states and comparing with the MQDT predictions. Additional discussion of the models and validation against literature measurements can be

found in Appendix E.

### A. $L = 0$ states

There are three Rydberg series with  $L = 0$  in  $^{171}\text{Yb}$  (Fig. 2). At low  $\nu$ , where hyperfine coupling is a small perturbation compared to the singlet-triplet splitting, these series are described in the  $LS$  basis as a single  $^1S_0$  series with  $F = 1/2$ , and two  $^3S_1$  series with  $F = \{1/2, 3/2\}$ . Very close to the threshold,  $jj$ -coupling is more appropriate: one  $F = 1/2$  series results from adding the outer electron spin ( $s = 1/2$ ) to the  $F_c = 0$  ion core, while the other  $F = 1/2$  and  $F = 3/2$  series are connected to  $F_c = 1$ . While these descriptions are equivalent for the  $F = 3/2$  series, the  $F = 1/2$  eigenstates cannot be simply described in either basis in between these limits, necessitating an MQDT model for these states.

We have experimentally measured the energy of most  $L = 0$   $F = 1/2$  states with  $25 < \nu < 120$  using laser spectroscopy as described in Appendix B. The measured  $L = 0$  Rydberg state energies and associated MQDT model predictions are shown in Fig. 3 *a*. The agreement is excellent: the  $F = 1/2$  states have a root-mean-squared deviation of 2.3 MHz from the model, consistent with the  $3\sigma$  uncertainty of 10 MHz of the wavelength meter used to determine the laser frequencies.

We have also measured the magnetic moments of a subset of states, shown in Fig. 3 *c*. For low  $\nu$ , the magnetic moments are close to the Landé  $g$ -factors for  $LS$ -coupled states, but they deviate significantly above  $\nu = 40$ .

The primary characteristic of the  $F = 1/2$  series is the avoided crossings in the energy spectrum. These can be understood from the channel structure of Fig. 2: strong channel mixing and level repulsion occur when the sep-



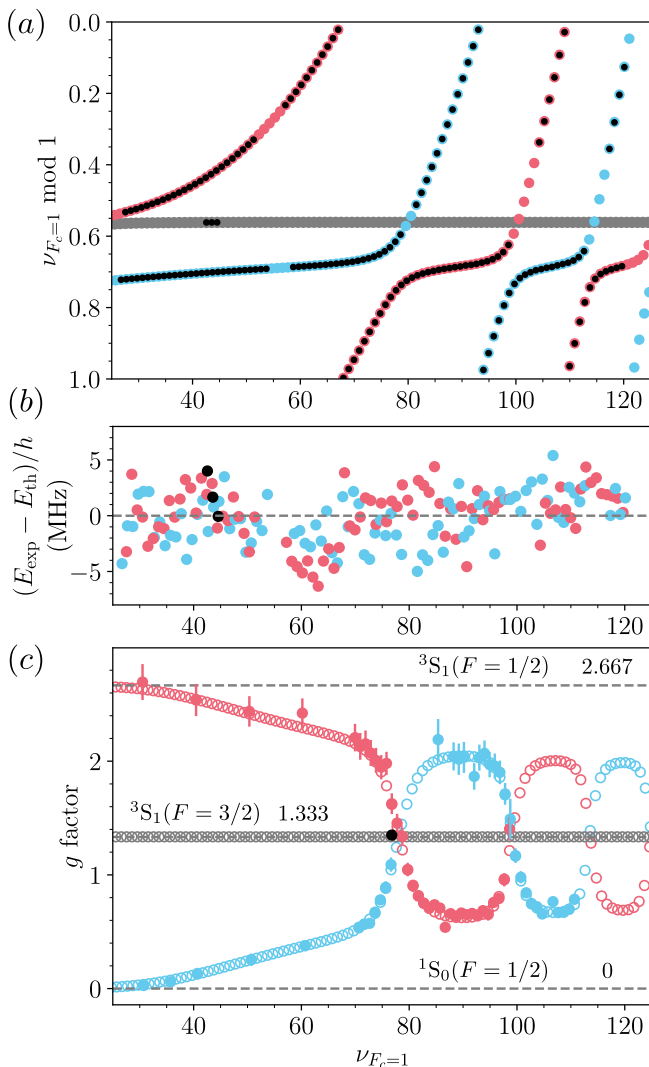


Figure 3. (a) Lu-Fano-type plot of  $^{171}\text{Yb}$   $|\nu, L=0, F=1/2\rangle$  Rydberg states (red, blue) and  $|\nu, L=0, F=3/2\rangle$  states (gray). The black points correspond to experimentally observed states, whereas the colored points denote bound states in the MQDT model. For  $\nu < 70$ , we refer to the red states as “triplet connected” and the blue states as “singlet connected” based on their dominant character in  $LS$  coupling. This description breaks down at higher principal quantum numbers. (b) Deviation between measured and modeled bound state energies. (c) Measured (filled circles) and predicted (empty circles)  $g$ -factors. The gray dashed lines indicate the Landé  $g$  factors in pure  $LS$  coupling.

aration between Rydberg levels is comparable to the ion core hyperfine splitting. For  $^{171}\text{Yb}$ , the  $\Delta n = 1, 2$  and 3 level crossings occur at  $\nu \approx 80, 100$  and 115, respectively, though we note that the wavefunction character is already affected far below the first avoided crossing at  $\nu = 80$ . The physical mechanism for this mixing is the exchange interaction between the inner and outer electrons.

The coloring of the curves in Fig. 3 is a guide to the

eye. The transition from  $LS$ - to  $jj$ -coupled states makes it challenging to introduce an unambiguous partition of all of the  $F = 1/2$  states into two series. Throughout this paper, we identify specific states by  $F, l$  and the effective principal quantum number  $\nu$  specified to two decimal places, (e.g.,  $|\nu = 54.28, L=0, F=1/2, m_F=1/2\rangle$ ). In this description,  $L$  is the Rydberg electron angular momentum in the  $6snl$  channels. In the specific case of the  $F = 1/2$  S states, we also find it convenient to refer to the states with  $\nu < 70$  as being “triplet-connected” or “singlet-connected” based on their dominant character in  $LS$  coupling.

Hyperfine coupling does not affect the  $F = 3/2$  series, which follows the same behavior as the  $^3S_1$  series in  $^{174}\text{Yb}$ , converging to the  $F_c = 1$  ionization limit. We have measured the energies of several  $F = 3/2$  states to confirm this behavior (Fig. 3a).

The MQDT model parameters and tables of measured energy levels are presented in Tab. VII and Tab. XXIV and Tab. XXV, respectively.

## B. $L = 1$ states

There are seven  $L = 1$  series in  $^{171}\text{Yb}$ . In  $LS$  coupling, they can be described as  $^3P_0(F = 1/2)$ ,  $^1P_1(F = \{1/2, 3/2\})$ ,  $^3P_1(F = \{1/2, 3/2\})$  and  $^3P_2(F = \{3/2, 5/2\})$ . In  $^{174}\text{Yb}$ , spin-orbit coupling mixes the two  $J = 1$  series as discussed in Section II; in  $^{171}\text{Yb}$ , hyperfine coupling additionally mixes the three  $F = 1/2$  series and the three  $F = 3/2$  series (Fig. 2).

We have experimentally measured the energies of a number of  $|\nu, L=1, F=1/2\rangle$  and  $|\nu, L=1, F=3/2\rangle$  states, using microwave transitions from  $|\nu, L=0, F=1/2\rangle$  states (for details, refer to Appendix B). The results are shown in Fig. 4, along with previously published measurements of low- $\nu$  states from three-photon laser spectroscopy [88, 89].

As in the case of the  $|\nu, L=0, F=1/2\rangle$  series, we begin with the  $^{174}\text{Yb}$  MQDT models of  $^{1,3}P_1$  and  $^3P_0$  (for  $F = 1/2$ ) and  $^{1,3}P_1$  and  $^3P_2$  (for  $F = 3/2$ ) presented in Appendix D and refine the model by a global fit to the observed state energies of the  $|\nu, L=1, F=1/2\rangle$  and  $|\nu, L=1, F=3/2\rangle$  Rydberg states. A comparison of the experimental state energies and the MQDT model energies is presented in Lu-Fano-type plots in Fig. 4(a) and (b) for  $F = 1/2$  and  $F = 3/2$ , respectively.

The behavior of the  $L = 1$  states is considerably more complex than the  $L = 0$  states, because the hyperfine coupling acts on states that were already strongly perturbed in  $^{174}\text{Yb}$ . As a result, the MQDT models for the  $F = 1/2$  and  $F = 3/2$   $L = 1$  series have 8 and 10 channels, respectively.

Unlike the  $L = 0$  series, we observe systematic deviations between the experimental and modeled energies. The high accuracy of the microwave measurements (100 kHz) makes it clear that the deviations are systematic as opposed to random. Particularly, the dispersion-

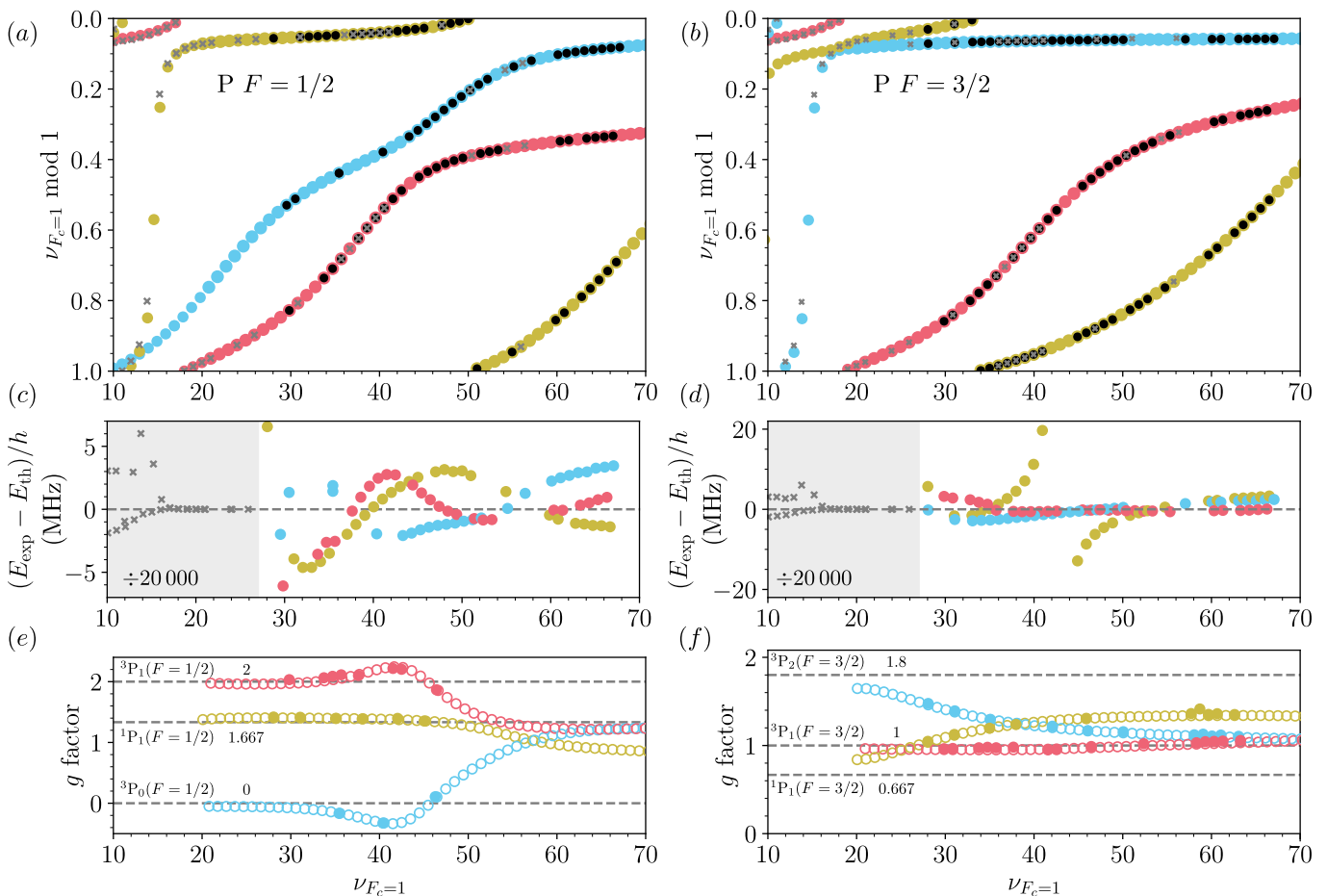


Figure 4. (a) and (b) Lu-Fano-type plot of  $^{171}\text{Yb}$   $|\nu, L = 1, F = 1/2\rangle$  and  $|\nu, L = 1, F = 3/2\rangle$  Rydberg states, respectively. The black points correspond to experimentally observed states by microwave spectroscopy, as described in Appendix B. The gray crosses are three-photon laser spectroscopy data from Ref. [89]. The colored points denote the MQDT model bound states (the colors are chosen to guide the eye). (c) and (d) Deviation between measured and modeled bound state energies. The deviations of the laser spectroscopy measurements are divided by a factor of 20 000, and are not shown for states that were also observed by microwave spectroscopy. (e) and (f) Measured (filled circles) and predicted (empty circles)  $g$ -factors. The gray dashed lines indicate the Landé  $g$  factors in pure  $LS$  coupling.

like feature in the fit residuals observed near  $\nu \approx 43$  for  $F = 3/2$  suggests the existence of an additional perturbing Rydberg series. The perturbing Rydberg state could come from unaccounted hyperfine splitting of excited states of the ion core, or from interactions with the  $L = 3$  Rydberg channels with  $(F = 3/2)^o$ . The significant deviations for states with  $\nu < 16$  suggest an additional perturber in that energy range, as well.

To confirm the accuracy of the MQDT wavefunctions, we also compare the predicted magnetic moments to experimental measurements (Figs. 4 (e) and (f)). As with the  $L = 0$  series, the moments align with the Landé  $g$ -factors for  $LS$  coupling at low principal quantum number, and deviate significantly at large  $\nu$  because of the combination of singlet-triplet mixing and hyperfine interaction. In particular, the MQDT model predicts negative  $g$ -factors for a range of  $|\nu, L = 1, F = 1/2\rangle$  states. We have experimentally confirmed the sign of the negative  $g$ -factors in two cases by observing the mag-

netic field dependent shifts of  $\sigma$  and  $\pi$  transitions from  $|\nu, L = 0, F = 1/2, m_F = \pm 1/2\rangle$  initial states.

There is only a single  $F = 5/2$  series with  $L = 1$ , which converges to the  $F_c = 1$  threshold. We have not directly measured any  $^{171}\text{Yb}$   $L = 1, F = 5/2$  states, but model this series using the MQDT model for the  $^3P_2$  series presented for  $^{174}\text{Yb}$  in the previous section. The parameters of this model are optimized from the fit to the observed  $|\nu, L = 1, F = 3/2\rangle$  Rydberg states, which contain a contribution from the  $^3P_2$   $F = 3/2$  states.

A summary of all measured  $L = 1$  states is presented in Tabs. XXVI and XXVIII. The MQDT model parameters are summarized in Tab. VIII and Tab. IX.

### C. Verification of MQDT models with Stark shifts

As with  $^{174}\text{Yb}$ , we probe the accuracy of Rydberg state energies and matrix elements obtained

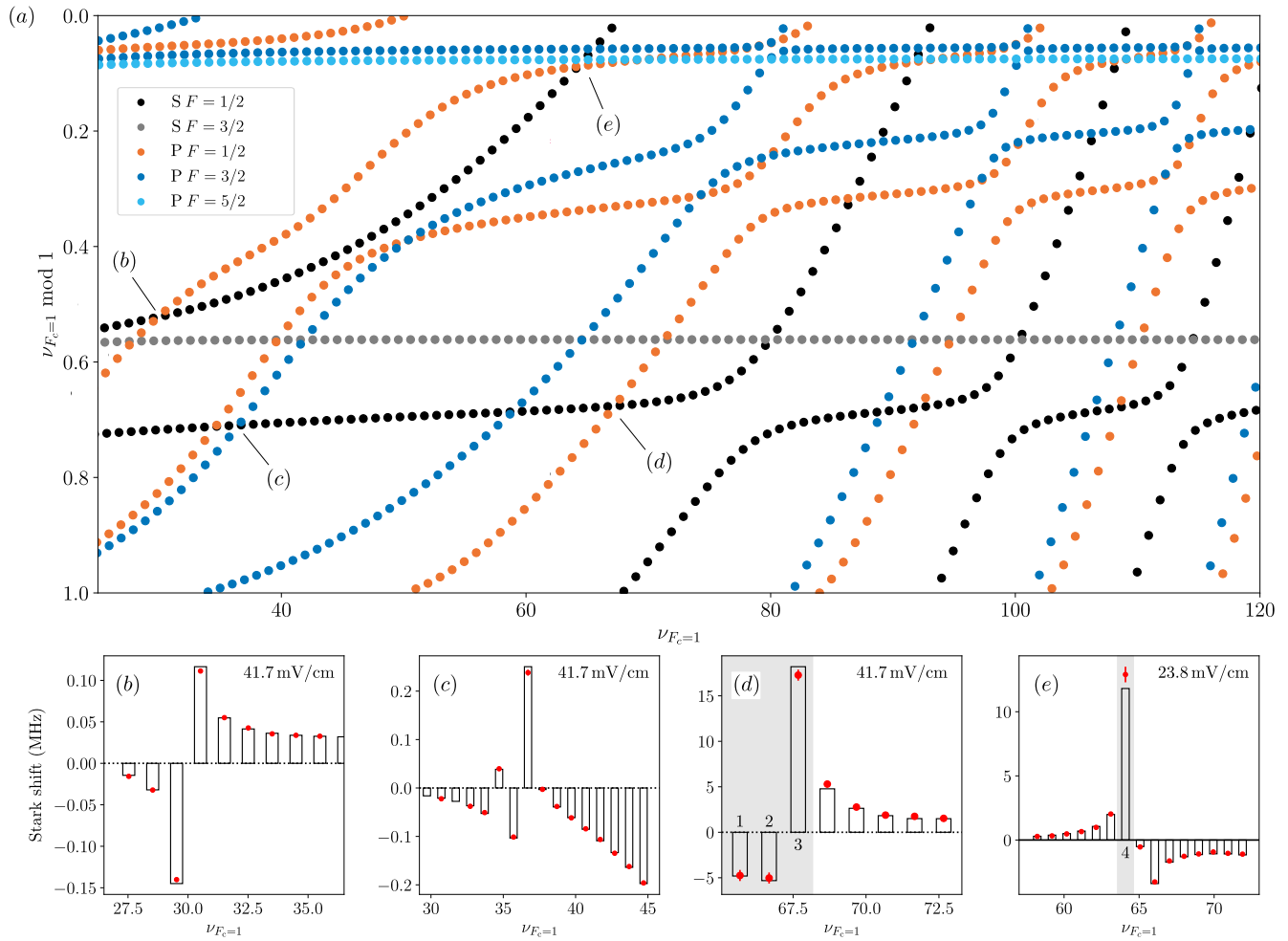


Figure 5. (a) Combined plot summarizing the MQDT model energies for all  $L = 0$  and  $L = 1$  Rydberg series in  $^{171}\text{Yb}$ . (b–e) Measured (red) and predicted (black bars) Stark shifts of selected  $L = 0$   $F = 1/2$  series in the vicinity of crossings with  $L = 1$  Rydberg series, at locations indicated by markers in panel (a). The Stark shift is reported at the electric field strength indicated in each panel. The gray shaded states correspond to near-degeneracies with significantly non-quadratic Stark shifts. A detailed comparison of the shifts of these states to a non-perturbative model is shown in Fig. 16.

from our MQDT models by measuring the dc Stark shift of  $|\nu, L = 0, F = 1/2\rangle$  states near degeneracies with  $|\nu, L = 1, F = 1/2\rangle$  and  $|\nu, L = 1, F = 3/2\rangle$  Rydberg states (Fig. 5a). The measured Stark shifts are in excellent agreement with the theoretical predictions, indicating good MQDT models for all relevant states, producing both accurate energies and channel contributions. Certain states with near-degenerate opposite parity states do not have quadratic Stark shifts even at very small electric fields, so we make the comparison between experiment and theory using the magnitude of the Stark shift at a particular field, instead of the usual static dipole polarizability. For these states, we also compare the measured field-dependent shift with a non-perturbative calculation, and find excellent agreement (Fig. 16). In Appendix F, we also summarize the predicted polarizability trends of the  $L = 0$  Rydberg states of both  $^{171}\text{Yb}$  and  $^{174}\text{Yb}$ .

#### IV. RYDBERG-RYDBERG INTERACTIONS IN $^{171}\text{Yb}$

A precise understanding of the interaction potential is important to realize high-fidelity gate operations. In this section, we use the developed MQDT model to predict the interaction potential for a pair of  $^{171}\text{Yb}$  atoms, then validate the model using direct experimental measurements in an optical tweezer array. The calculation builds on established techniques for performing similar calculations in alkali atoms, based on numerically diagonalizing the multipolar interaction Hamiltonian in a large basis of pair states [90, 91]. In the context of alkali atoms, this approach has been experimentally validated by spectroscopic measurements in optical tweezers [15, 16] and optical lattices [24]. We follow the formalism extending these techniques to states described by MQDT that was introduced previously in Refs. [44, 52].

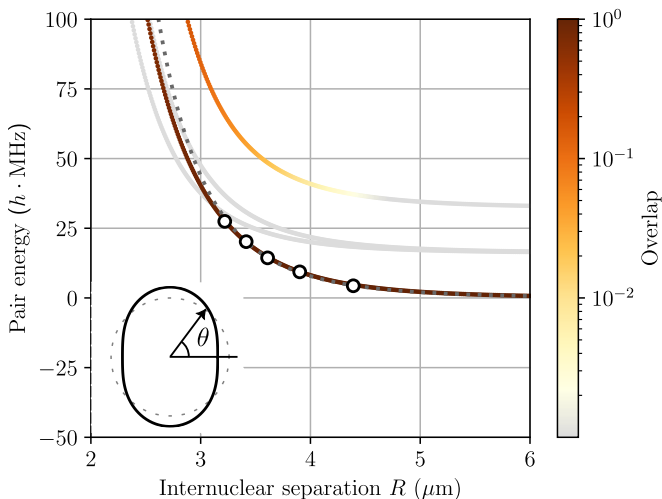


Figure 6. Predicted pair-interaction potentials for a target Rydberg state  $|t\rangle = |54.28, L=0, F=1/2, m_F=-1/2\rangle$ , together with measured energy shifts (white circles). The magnetic field strength is 4.88(6) G, corresponding to a Zeeman splitting of 16.1 MHz, and is oriented at  $\theta = \pi/2$  to the inter-atomic axis. The color of the curves denotes the overlap of each eigenstate with the target pair state  $|t\rangle^{\otimes 2}$ . The gray, dashed line shows the asymptotic  $1/R^6$  scaling. *Inset*: predicted angle-dependence of the  $C_6$  coefficient.  $\theta$  is the angle between the magnetic field and the inter-atomic axis.

We first consider the interaction potential between a pair of atoms in a  $|\nu, L=0, F=1/2, m_F\rangle$  state. For concreteness, we focus on the triplet-connected  $|54.28, L=0, F=1/2, m_F\rangle$  states. The calculated pair potentials for the four combinations of  $m_F$  sublevels is shown in Fig. 6. The predicted pair potential closely follows the expected van der Waals form  $V(R) = C_6/R^6$ , with  $C_6 \approx h \cdot 34 \text{ GHz}(\mu\text{m})^6$ . For comparison, we note that the  $C_6$  coefficient for the Rb  $nS_{1/2}$  state with the most similar  $\nu$  ( $n=57$ ) is  $C_6 \approx h \cdot 76 \text{ GHz}(\mu\text{m})^6$  [91].

We test the theoretical prediction by directly measuring the van der Waals shift using a pair of atoms in optical tweezers with separations from 3.3–4.5  $\mu\text{m}$ . The measured energy shift is in excellent agreement with the predicted pair potential after scaling the experimental interatomic separation by a factor of 0.97 relative to the expected values based on the design magnification of the optical system used to project and image the tweezer array (Fig. 6). Additional details about the measurement technique are described in Appendix C.

We note that there is a nearby  $F=3/2$   $D$  state with a detuning of only 68 MHz at zero magnetic field. As this state is also laser-accessible from  $^3P_0$ , it could cause problems for blockade gates if its van der Waals interaction has the opposite sign from the target state, pushing it into resonance. We are unable to predict the  $D$  state interactions, because we do not yet have an MQDT model for the  $F$  states. However, we note that this problem can be avoided by using the next lowest triplet-connected  $S$  state with  $\nu = 53.30$ , where the nearest  $D$  state is de-

tuned by more than 600 MHz.

The predicted  $C_6$  coefficient has an anisotropy of 46% (Fig. 6, inset). In alkali atoms, the van der Waals interaction between atoms in  $S$  states is usually highly isotropic, because of the small spin-orbit coupling in the  $P$  states participating in the interaction [92]. For example, the  $C_6$  coefficient for the  $50^2S_{1/2}$  state in Rb has an anisotropy of approximately 1%. The large anisotropy in this  $^{171}\text{Yb}$  state is attributed to the large spin-orbit coupling in Yb (scaling as  $Z^4$ ), and series perturbations that lift the degeneracy between  $J$  manifolds (as shown in Fig. 1b for the  $^{174}\text{Yb}$   $P$  series), which has the same effect as spin-orbit coupling. The anisotropy also results in off-diagonal  $C_6$  interactions that mix different  $m_F$  levels. As seen from the color scale in Fig. 6, the  $|m_F=1/2, m_F=1/2\rangle$  state acquires a significant  $|m_F=-1/2, m_F=-1/2\rangle$  character once the van der Waals shift becomes comparable to the Zeeman splitting. This effect is suppressed if the interatomic spacing is parallel to the magnetic field, as a consequence of the dipole-dipole selection rules [92].

We have computed the  $C_6$  coefficient for all of the  $F=1/2$  series, and summarized the results in Fig. 21. The  $C_6$  coefficient for the triplet-connected  $F=1/2$  series follows the expected  $\nu^{11}$  scaling in the range  $\nu \lesssim 65$ . The singlet-connected  $F=1/2$  series has a much smaller  $C_6$  coefficient in this range, with the exception of isolated states with accidental hyperfine-induced Förster resonances. This is consistent with previous estimates of a small  $C_6$  for the  $^{174}\text{Yb}$   $^1S_0$  series using a single-channel approximation [93].

Next, we consider an  $F=3/2$  target state. Specifically, we consider the state  $|54.56, L=0, F=3/2, m_F=+3/2\rangle$ , which was used to implement two-qubit gates in Ref. [40]. The computed pair potential is shown in Fig. 7a. Unlike the  $F=1/2$  state shown in Fig. 6, the pair potential for this  $F=3/2$  state deviates strongly from the idealized  $C_6/R^6$  van der Waals scaling, because of a previously unknown Förster resonance with a pair state made up of  $L=1$  states with  $F=3/2$  and  $F=5/2$ . At zero magnetic field, this pair state is detuned by only approximately 3 MHz from the  $|54.56, L=0, F=3/2\rangle^{\otimes 2}$  pair state. The complex series of crossings results from different magnetic sublevels being pushed into exact resonance by the interaction, in a finite magnetic field of  $B \approx 5$  G. Similar behavior is observed for the  $m_F=-3/2$  states, though the resulting spectrum is slightly less complex as the Zeeman shift has the same sign as the van der Waals interaction.

We have also experimentally measured the interaction shifts for this state. We are able to identify all pair states from this complex spectrum with an overlap of more than 10% with the target state, and find good agreement for both  $m_F=+3/2$  and  $m_F=-3/2$  using the same rescaling factor of the interatomic separation (0.97) used in Fig. 6. In the case of  $m_F=+3/2$ , we observe deviations of 1–2 MHz for one of the eigenstates. This is comparable in magnitude to the fit residuals in the  $F=3/2$   $P$  series MQDT model (Fig. 4; the  $F=3/2$  state that contributes



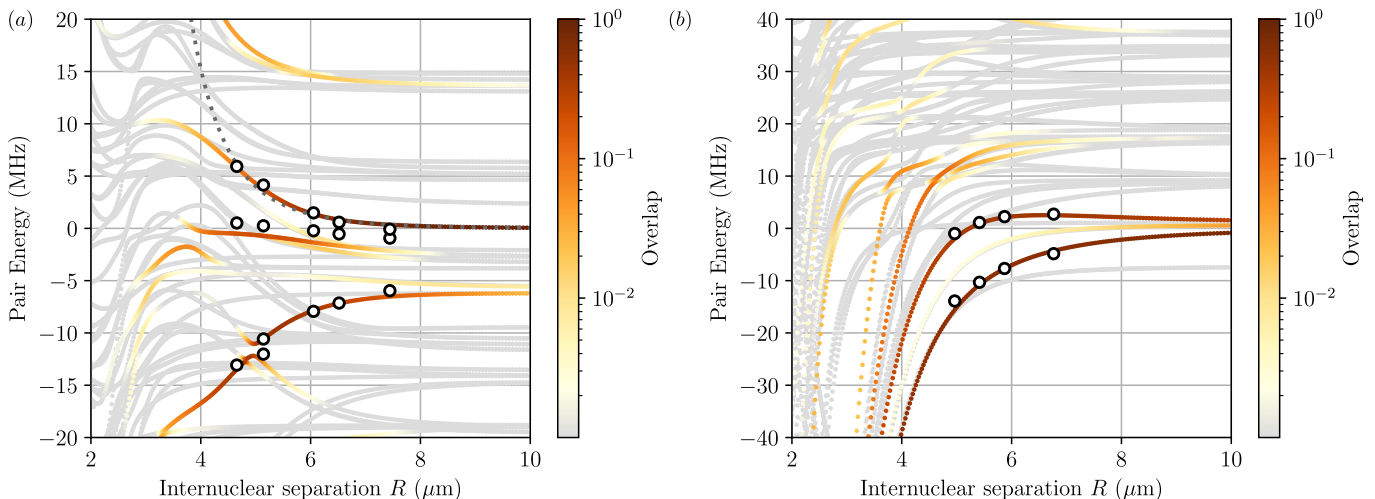


Figure 7. Predicted pair-interaction potentials for a target state  $|54.56, L=0, F=3/2, m_F\rangle$  with (a)  $m_F = 3/2$  and (b)  $m_F = -3/2$ , at a magnetic field of 5.03(6) G ( $\theta = \pi/2$ ). The color of the curves denotes the overlap with the target pair state. The white circles indicate experimentally observed resonances as described in the text. The gray dashed line in panel (a) shows the asymptotic  $1/R^6$  scaling.

to the Förster resonance is in the blue-colored series in that figure).

This Förster resonance is not an accidental degeneracy for the  $|54.56, L=0, F=3/2\rangle$  state, but rather a systematic trend: almost all  $|\nu, L=0, F=3/2\rangle$  states with  $\nu > 30$  have a Förster defect less than 10 MHz (Fig. 22). While Förster resonances are sometimes sought to increase the strength of the Rydberg-Rydberg interaction at long range [94, 95], such a near-degenerate resonance is problematic for two-qubit gates because it results in a large number of weakly allowed transitions near zero energy at short separations, allowing Rydberg excitation within the blockade radius [96]. This effect is sometimes referred to as *Rydberg spaghetti*. At the same time, Förster resonances increase the long-range tail of the interactions, preventing parallel implementation of gates in a qubit array [97]. Understanding the existence of this Förster resonance resolves several observations from Ref. [40], including an unknown contribution to the error budget of about 1%, and the need to use a large separation (43  $\mu\text{m}$ ) between adjacent dimers to achieve the highest gate fidelity.

## V. IMPROVED TWO-QUBIT GATES

We now demonstrate improved gate performance using the  $|54.28, L=0, F=1/2\rangle$  state. Previous demonstrations of entangling gates in  $^{171}\text{Yb}$  used  $F=3/2$  states [31, 40]. The highest reported fidelity is  $\mathcal{F} = 0.980(1)$ , which is approximately 1% lower than the predicted fidelity of  $\mathcal{F} = 0.989$  based on error sources that were understood at the time [40]. We conjecture the additional errors were the result of unwanted Rydberg excitation to nearby pair states (Fig. 7), and that the

$F=1/2$  state with a cleaner interaction potential will lead to higher fidelity.

We implement a two-qubit gate using the same approach as Ref. [40]. Briefly, we prepare an array of four pairs of atoms (with a spacing of  $d = 2.4 \mu\text{m}$  between atoms within a pair, and  $D = 24 \mu\text{m}$  between pairs) and implement CZ gates in parallel using a variant of the time-optimal two-qubit gate [98]. The gate is driven using a UV laser at 302 nm, with a power of 20 mW in a beam with a  $1/e^2$  radius of 12  $\mu\text{m}$  to achieve a Rabi frequency of  $\Omega = 2\pi \times 2.5$  MHz between  $^3P_0$   $m_F = +1/2$  and Rydberg state with  $m_F = -1/2$ . Because of geometric constraints, the laser is linearly polarized perpendicular to the magnetic field, such that only half of the power contributes to the  $\sigma^-$  transition that drives the gate. We estimate the fidelity using the randomized circuit characterization approach of Ref. [40, 99], with interleaved global single-qubit gates. With these parameters, we observe a CZ gate fidelity of  $\mathcal{F} = 0.994(1)$  (Fig. 8).

This result improves on the previous best gate in  $^{171}\text{Yb}$  by a factor of 3.3. Importantly, the error budget for the gate in Fig. 8a is now in excellent agreement with a model based on independently measured sources of error (Fig. 8b) [40]. The dominant contributions are the finite lifetime of the Rydberg state (measured to be  $T_r = 56(4) \mu\text{s}$ , contributing an error of  $\epsilon = 3.3 \times 10^{-3}$ ) and Doppler shifts ( $\epsilon = 1.4 \times 10^{-3}$  at an atomic temperature during the gate of  $T = 2.9 \mu\text{K}$ ). We also estimate the impact of other sources of error, including unwanted excitation of the other  $m_F$  sublevel of the Rydberg state ( $\epsilon = 4.8 \times 10^{-4}$ ), site-to-site and shot-to-shot laser intensity variation ( $\epsilon = 2.0 \times 10^{-4}$ ), a finite Rydberg blockade strength ( $\epsilon = 1.9 \times 10^{-4}$ ; the pulse is not compensated for the finite blockade [97, 98]), and fast laser phase and amplitude noise ( $\epsilon_{PM} = 5.8 \times 10^{-5}$  and

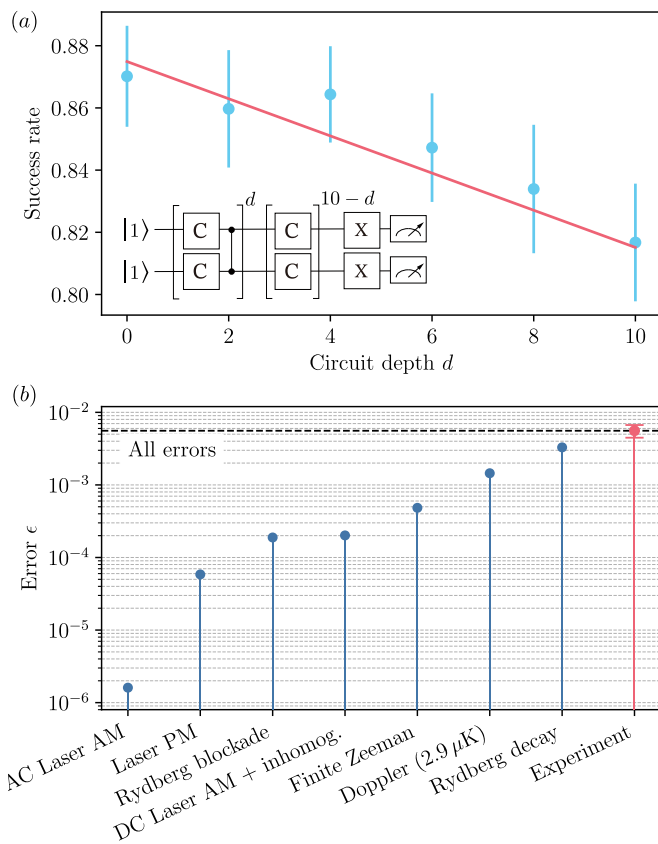


Figure 8. (a) Randomized circuit characterization of the time-optimal CZ gate, using a variable depth  $d$ . The fitted error rate is  $\epsilon = 5.6(1.1) \times 10^{-3}$  per two-qubit gate. (b) Numerical simulation of contributions to the gate error, including the finite Rydberg state lifetime, Doppler shifts from atomic motion, off-resonant excitation of neighbouring  $m_F$  sublevels in finite magnetic fields, shot-to-shot and site-to-site laser amplitude variations, finite Rydberg blockade, and fast laser phase (PM) and amplitude noise (AM). The total simulated error rate with all sources applied simultaneously is  $\epsilon = 5.7 \times 10^{-3}$  (black dashed line), in good agreement with the experimentally measured error rate (red point).

$\epsilon_{AM} = 1.6 \times 10^{-6}$ , respectively). Since the dominant errors can be suppressed by increasing the gate speed (*i.e.*, with additional laser power), these results suggest that significantly higher gate fidelities are within reach for  $^{171}\text{Yb}$ .

## VI. DISCUSSION AND CONCLUSION

We have presented detailed spectroscopy and modeling of the Rydberg states of both  $^{174}\text{Yb}$  and  $^{171}\text{Yb}$  with  $L \leq 2$ . The models are validated with experimental measurements of Stark shifts, magnetic moments and Rydberg interactions. To the best of our knowledge, this is the most comprehensive validation of an MQDT model for a complex atom, and allows key properties for Rydberg atom quantum computing and simulation to be

predicted with the level of accuracy that is routine for alkali atoms. This will provide vital input for future experiments in quantum computing and simulation with Yb, or with Yb-alkali mixtures. Moreover, the calculation technique is a template for exploring other atoms in the lanthanide group, such as Ho or Er [64, 65].

We used this model to identify the likely cause of previously unattributed errors in entangling gates using  $F = 3/2$  Rydberg states. We also predicted a more suitable Rydberg state with  $F = 1/2$ , leading to an improved gate fidelity of  $\mathcal{F} = 0.994(1)$ , with errors reduced by a factor of 3.3 compared to the previous best gate demonstration using  $^{171}\text{Yb}$  [40].

We identify several avenues for future work. The first is including states with  $L \geq 3$ , which are needed to accurately predict the interactions of  $D$  states, which can create blockade violations for  $S$  states. The second is to extend the model to predict Rydberg state lifetimes and decay branching ratios, which will involve more careful fitting of MQDT models to low- $n$  perturbers and including matrix elements between different core electron states [43]. While low- $n$  perturbers have little effect on the Rydberg character of high- $n$  states, they can have a large impact on the lifetime and decay branching ratio by providing a new decay pathway via the population of the perturbing state [20, 43].

Another area of interest is the behavior of autoionizing states, of the form  $6p_{1/2}nl$ . These states have found use for Rydberg atom detection [100, 101], coherent control [102, 103] and in quantum error correction [39]. To our knowledge, only the  $^{174}\text{Yb } ^3S_1$  autoionizing series has been characterized [102]. A systematic study, including  $^{171}\text{Yb}$ , would be beneficial for applications relying on use of these states.

Finally, we note that these models may have applications beyond quantum computing. Ytterbium clocks are among the most precise in the world [104], and Rydberg states can be used for generating entanglement to enhance precision [35, 36]. It has also been proposed to use Rydberg states for *in situ* absolute calibration of the temperature through the blackbody radiation spectrum [105], which would warrant more precise validation of the modeled matrix elements.

## ACKNOWLEDGMENTS

We gratefully acknowledge helpful conversations with Adam Kaufman and Aruku Senoo, and Prof. Herbert Rinneberg for providing a copy of Ref. [89]. This work was supported by the Army Research Office (W911NF-1810215), the Office of Naval Research (N00014-20-1-2426), DARPA ONISQ (W911NF-20-10021), the National Science Foundation (QLCI grant OMA-2120757, and NSF CAREER PHY-2047620), the Sloan Foundation and the Gordon and Betty Moore Foundation (Grant DOI 10.37807/gbmf12253).

## Appendix A: MQDT formalism

MQDT was introduced by Seaton [41] and reformulated with the concept of frame transformations by Fano [42]. It has been used as a powerful tool for modelling effective multi-electron systems such as noble gas [62, 68], and alkaline-earth(-like)[43, 47] atoms, or the H<sub>2</sub> molecule [42]. Here, we follow the semi-empirical variant of MQDT [106] and for the evaluation of multipole moments, we follow mostly the formalism summarized in Ref. [44]. In the following, we will briefly introduce the basic concepts.

We introduce different types of channels (1)  $\alpha$ , also referred to as “close-coupling” channels and (2)  $i$ , asymptotic and mostly Coulombic, “collision” channels. The short-range, non-Coulombic interaction of the Rydberg electron and the ion core are encoded in eigenchannel quantum defects  $\mu_\alpha$  and the channels are coupled by the unitary transformation matrix  $U_{i\alpha}$ . Following standard derivations [106], we find that in the MQDT framework

$$\sum_{\alpha} \tilde{A}_{\alpha} U_{i\alpha} \sin[\pi(\nu_i + \mu_{\alpha})] = 0 \quad (\text{A1})$$

has to be satisfied, which has non-trivial solutions for the bound state energies  $\nu_i$  when

$$\det |U_{i\alpha} \sin[\pi(\mu_{\alpha} + \nu_i)]| = \det |F_{i\alpha}| = 0. \quad (\text{A2})$$

For the case of considerable spin-orbit interaction, it is sometimes convenient to introduce an intermediate basis  $\bar{\alpha}$  of purely  $LS$  coupled channels and to express the collision channels  $i$  in terms of  $jj$ -coupled channels [68, 107]. In this case, we can decompose  $U_{i\alpha}$  as:

$$U_{i\alpha} = U_{i\bar{\alpha}} V_{\bar{\alpha}\alpha}, \quad (\text{A3})$$

where  $U_{i\bar{\alpha}}$  corresponds to the  $LS$ - $jj$  frame transformation

$$\begin{aligned} U_{i\bar{\alpha}} &= \langle ((S_c L_c) J_c (s \ell) j) J | ((S_c s) S (L_c \ell) L) J \rangle \\ &= [S, L, J_c, j]^{1/2} \begin{Bmatrix} S_c & L_c & J_c \\ s & \ell & j \\ S & L & J \end{Bmatrix} \end{aligned} \quad (\text{A4})$$

from Eq. (6.4.2) of Ref. [108] and  $[a, b, \dots]^{1/2} = \sqrt{(2a+1)(2b+1)\dots}$ .

The second matrix  $V_{\bar{\alpha}\alpha}$  accounts for configuration interaction by introducing couplings between the  $\bar{\alpha}$  channels.  $V_{\bar{\alpha}\alpha}$  is typically expressed as a series of rotations by Euler angles  $\theta_{ij}$  around channels  $i$  and  $j$  (see Eq. (15) of Ref. [109])

$$V_{\bar{\alpha}\alpha} = \prod \mathcal{R}(\theta_{ij}). \quad (\text{A5})$$

We treat energy-dependence of the eigenchannel quantum defects as

$$\mu_{\alpha}(\epsilon) = \mu_{\alpha}^{(0)} + \epsilon \mu_{\alpha}^{(2)} + \epsilon^2 \mu_{\alpha}^{(4)} \dots, \quad (\text{A6})$$

and similarly for  $\theta_{ij}$

$$\theta_{ij}(\epsilon) = \theta_{ij}^{(0)} + \epsilon \theta_{ij}^{(2)} \dots, \quad (\text{A7})$$

with  $\epsilon = 1/\nu^2$  [68]. Bound states are found at the intersection of the surface spanned by Eq. (A2) and the curve

$$\nu_i = \left( \frac{I_i - I_j}{R_M} + \frac{1}{\nu_j^2} \right)^{-1/2}, \quad (\text{A8})$$

where  $\nu_i$  and  $\nu_j$  are effective principal quantum numbers relative to the  $i$ th and  $j$ th ionization limit  $I_i$  and  $I_j$ , respectively, and  $R_M$  is the mass-reduced Rydberg constant. Once a bound state has been found, we can evaluate  $\tilde{A}_{\alpha,b}$  by

$$\tilde{A}_{\alpha,b} = C_{i\alpha} / \left[ \sum_{\alpha} C_{i\alpha}^2 \right]^{1/2}. \quad (\text{A9})$$

where  $C_{i\alpha}$  is the cofactor of the  $i$ th row and  $\alpha$ th column of the matrix  $F_{i\alpha}$ , and in the evaluation of Eq. (A9), channel  $i$  can be chosen for convenience. For the bound state  $b$ , the channel contributions in terms of collision channels  $i$  in  $jj$  coupling are then calculated using [68]

$$A_{i,b} = (-1)^{l_i+1} (\nu_{i,b})^{3/2} \sum_{\alpha} U_{i\alpha} \cos[\pi(\nu_{i,b} + \mu_{\alpha})] \tilde{A}_{\alpha,b} / N_b, \quad (\text{A10})$$

where  $N_b$  ensures the normalization [41] of the wavefunction and is given by [68]

$$\begin{aligned} N_b^2 &= \sum_{i,\alpha} \nu_{i,b}^3 U_{i\alpha} \cos[\pi(\nu_{i,b} + \mu_{\alpha})] \tilde{A}_{\alpha,b} \\ &+ \sum_{\alpha} \left( \frac{d\mu_{\alpha}}{dE} \right) \tilde{A}_{\alpha,b}^2 \\ &+ \frac{1}{\pi} \sum_{i,\alpha,\beta} \left( \frac{dU_{i,\alpha}}{dE} \right) U_{i,\beta} \sin[\pi(\mu_{\alpha} - \mu_{\beta})] \tilde{A}_{\alpha,b} \tilde{A}_{\beta,b}. \end{aligned} \quad (\text{A11})$$

From the obtained channel fraction in  $jj$  coupling, we can infer the channel fractions in  $LS$  coupling by

$$A_{\bar{\alpha},b} = \sum_i U_{i\bar{\alpha}} A_{i,b}. \quad (\text{A12})$$

In this framework, the task lies in the determination of a set of  $\mu_{\alpha}$  and  $U_{i\alpha}$ , that reproduce a set of properties

of Rydberg states of interest. In cases where multiple Rydberg channels converge to the same ionization limit, state energies are not sufficient to determine a unique set of MQDT parameters and further experimental observables such as  $g$ -factors, polarizabilities, or lifetimes are needed to refine the MQDT models [47, 62].

Single atom matrix elements of operator  $\hat{\zeta}$  acting on the channel function  $|\Phi_i\rangle$  and leaving the orbital angular momentum  $l$  of the Rydberg electron unchanged are evaluated by

$$\hat{\zeta}_{b,b'} = \sum_{i,i'} (A^T)_{b,i} \langle \Phi_i | \hat{\zeta} | \Phi_{i'} \rangle O_{ib,i'b'} A_{i',b'} \quad (\text{A13})$$

where

$$O_{ib,i'b'} = \frac{2\sqrt{\nu_{ib}\nu_{i'b'}} \sin(\beta_{ib} - \beta_{i'b'})}{(\nu_{ib} + \nu_{i'b'}) (\beta_{ib} - \beta_{i'b'})} \quad (\text{A14})$$

is a radial overlap integral [44].

For the case of the multipole operator  $\hat{Q}^{(kq)} = r^k Y_{k,q}(\Omega)$ , the contribution of the core electrons is neglected and only the contribution of the Rydberg electron is considered [44]

$$\mathcal{Q}_{b,b'}^{(kq)} = \sum_{i,i'} (A^T)_{b,i} \langle \Phi_i | Y_{k,q} | \Phi_{i'} \rangle R_{ib,i'b'}^{(k)} A_{i',b}. \quad (\text{A15})$$

## 1. Introduction of hyperfine interaction in the ion core

For isotopes with non-zero nuclear spin, the hyperfine interaction in the ion core has to be considered. Here, we follow the formalism introduced in earlier work [70, 85, 86]. By introducing a frame transformation to include the hyperfine interaction, we can extend the formalism introduced in the previous subsection. Eq. (A2) is then replaced by

$$\det |U_{i_F, \alpha_F} \sin[\pi(\mu_{\alpha_F} + \nu_{i_F})]| = 0. \quad (\text{A16})$$

Because the hyperfine interaction in the ion core is small compared to the non-Coulombic interactions in the ‘‘close-coupling’’ region, we can treat the hyperfine interaction in this region as a perturbation and the close-coupling parameters  $\mu_\alpha$  and  $U_{i\alpha}$  will only be slightly affected. Therefore, we can construct the MQDT models for isotopes with non-zero nuclear spin from MQDT parameters obtained from even isotopes with nuclear spin  $I = 0$ . In this work, we use the MQDT models and parameters obtained for  $^{174}\text{Yb}$  and introduce hyperfine coupling of the ion core with

$$U_{i_F, \alpha_F} = U_{i_F, i} U_{i, \alpha_F} \quad (\text{A17})$$

where  $U_{i_F, i}$  is the frame transformation

$$U_{i_F, i} = \langle (((J_c I) F_c j) F) | (J_c j) J I F \rangle \\ = (-1)^{I+j+F_c+J} [J, F_c]^{1/2} \begin{Bmatrix} I & J_c & F_c \\ j & F & J \end{Bmatrix}, \quad (\text{A18})$$

which uses Eq. (6.4.2) of Ref. [108].

However, in the asymptotic region, the hyperfine interaction of the ion core will become comparable to spin-orbit interaction and electron binding energy. In this regime, even in the absence of spin-orbit coupling, the total spin  $S$  is not a good quantum number. The remaining good quantum numbers of the Rydberg state are the total angular momentum  $F$ , and parity.

In our analysis, we only consider the hyperfine splitting in the  $6s^2 S_{1/2}$  ground state of the  $^{171}\text{Yb}^+$  ion. We neglect the hyperfine splitting of excited states of the  $^{171}\text{Yb}^+$ -ion core. This is likely a good approximation because the excited states are energetically far above the channels converging to the  $^{171}\text{Yb}^+$  ground state considered in this work. A small isotope dependence [52] and hyperfine-induced mixing of channels can yield variations in the close-coupling parameters. Therefore, we perform an additional optimization of the MQDT parameters for  $^{171}\text{Yb}$ , but use the  $^{174}\text{Yb}$  MQDT parameters as a starting point for the fitting procedure of the physical observables of  $^{171}\text{Yb}$  for an improved modelling.

## 2. Magnetic-field-induced Zeeman shifts and couplings

We calculate magnetic-field-induced Zeeman shifts and couplings of Rydberg atoms using the paramagnetic interaction Hamiltonian

$$H_{\text{PM}} = -\vec{\mu} \cdot \vec{B} = \{\mu_B [\vec{L}_c + \vec{\ell} + g_s(\vec{S}_c + \vec{s})] - \mu_I \vec{I}\} \cdot \vec{B} \quad (\text{A19})$$

using the expressions presented in Ref. [44] for the general case of Rydberg states with hyperfine interaction in the ion core. We also include the diamagnetic interaction Hamiltonian [110] as

$$H_{\text{DM}} = \frac{1}{8m_e} |\vec{d} \times \vec{B}|^2. \quad (\text{A20})$$

The diamagnetic interaction can be expressed in terms of spherical harmonics (compare, e.g., Ref [90])

$$\frac{1}{8m_e} |\vec{d} \times \vec{B}|^2 = \frac{e^2}{12m_e} r^2 \sqrt{4\pi} \left( Y_{0,0} - \sqrt{\frac{1}{5}} Y_{2,0} \right) B^2. \quad (\text{A21})$$



## Appendix B: Atomic beam spectroscopy apparatus

The spectroscopic data presented in this article are obtained by laser and radiofrequency (RF) spectroscopy on an atomic beam of  $^{174}\text{Yb}$  or  $^{171}\text{Yb}$  atoms. The atomic beam is generated by heating a sample of ytterbium to a temperature of  $310^\circ\text{C}$  in an oven with a collimator opening of approximately 1 cm. The atomic beam is further collimated by a pinhole with a diameter of 3 mm, approximately 12 cm after the oven collimator and 9 cm before the spectroscopy region.

Transitions to S and D Rydberg states are driven by a two-photon laser transition through the intermediate  $6s6p^1P_1$  state. The laser light needed for the transition with wavelengths of 399 nm ( $6s^2^1S_0 \rightarrow 6s6p^1P_1$ ) and 394-399 nm ( $6s6p^1P_1 \rightarrow$  Rydberg state) is generated by frequency doubling the output of tunable titanium-sapphire (Ti:sapph) lasers in a resonantly enhanced frequency doubling cavity. The isotope shifts on the  $6s^2^1S_0 \rightarrow 6s6p^1P_1$  transition [111] are used for an isotope selective excitation into the Rydberg state.

To minimize Doppler shifts on the two-photon laser transitions, counter-propagating laser beams are applied to the atomic beam at a  $90^\circ$  angle. Laser pulses with length of 1-3  $\mu\text{s}$  are generated by acousto-optic modulators. The laser frequencies are monitored by measuring the frequency of the fundamental output of the Ti:sapph laser using a HIGHFINESSE WS8-10 wavelength meter with a specified  $3\sigma$  uncertainty of 10 MHz. At regular intervals, the wavelength meter is referenced to a 399 nm laser that is frequency locked to a ultra-low-expansion cavity.

Transition between Rydberg states are driven using RF with frequencies in the range of 10-175 GHz. The RF radiation is obtained from a WINDFREAK TECHN., LLC SYNTHHD PRO (up to 24 GHz) dual-channel microwave generator or by using a combination of active x4 (MARKI MICROWAVE AQA-2156, 21-56 GHz) and/or passive x4 (MARKI MICROWAVE MMQ-40125H, 40-175 GHz) frequency multipliers. The microwave generator is referenced to a stable 10 MHz reference signal obtained from a GPS disciplined Rb atomic clock (STANFORD RESEARCH SYSTEMS FS725). RF pulses with duration of 1-8  $\mu\text{s}$  are obtained by amplitude modulating the output of the microwave generator before frequency multiplication using PIN absorptive modulators (HEWLETT PACKARD 33008C or 11720A). The obtained RF radiation is coupled into the vacuum chamber through vacuum viewports. All laser radiation is switched off for the duration of the RF pulses. The power of the RF radiation is controlled using either a digital step attenuator (ANALOG DEVICES ADRF5740) or a WR-10 direct-reading attenuator (MI-WAVE 510W/387). All stated Rydberg-Rydberg transitions have been measured at varying RF powers and extrapolated to “zero” RF power to remove frequency shifts caused by AC-Stark shifts.

To control the electric field in the spectroscopy region,

we apply voltages to two segmented circular electrodes (4 segments each) separated by 3 cm. Stray electric fields are compensated at the beginning of each day, by minimizing the quadratic Stark shift of the  $6s130s\ 130^1S_0$  Rydberg state of  $^{174}\text{Yb}$ . We observe day-to-day fluctuations of the required electric compensation fields of less than 3 mV/cm. Magnetic fields are controlled by three pairs of coils placed outside the vacuum chamber, arranged in Helmholtz configuration. The magnetic fields are calibrated by RF spectroscopy of the Zeeman splittings on a  $n'^3S_1 \leftarrow n^1S_0$  transition, and assuming a  $g$ -factor of the mostly unperturbed  $n^3S_1$  Rydberg series to be  $g(^3S_1) = g_s \approx 2.0023$ .

Population in Rydberg states is detected by state-selective pulsed-field ionization (see, e.g., [79]). High-voltage (HV) pulses with a maximum voltage of 2.5 kV are generated by switching between a low-voltage (during Rydberg spectroscopy) and a HV input using HV MOSFET switches (BEHLKE HTS 31-03-GSM) and are applied to a set of the electrodes. The resulting maximum field of  $\approx 833\text{ V cm}^{-1}$  limits the lowest detectable Rydberg states in our setup to an effective principal quantum number  $\nu \approx 26$ . The resulting  $\text{Yb}^+$  ions are accelerated towards and detected on a time-resolved microchannel-plate ion detector (HAMAMATSU F13446-11) and recorded on an oscilloscope.

## Appendix C: Measuring Rydberg interactions in optical tweezers

We measure the distance-dependent interactions between single  $^{171}\text{Yb}$  Rydberg atoms trapped in optical tweezer arrays using the setup described in Ref. [40]. Similar approaches have been previously used to measure  $C_6$  coefficients of Rydberg-pair states in Rb [15] and angle-dependent dipole-dipole interaction strengths [16]. We initialize pairs of atoms in the  $|1\rangle \equiv |m_F = +1/2\rangle$  sublevel of the  $6s6p^3P_0$  metastable state. Static magnetic fields are applied at  $90^\circ$  ( $\theta = \pi/2$ ) with respect to the internuclear separation. Transitions into Rydberg pair states are subsequently driven by a two-photon transition detuned by  $\Delta E$  from the asymptotic case of two isolated Rydberg atoms. Pairs of atoms transferred into Rydberg states are blown out of the optical tweezers by driving a transition (369 nm) into an autoionizing state [102]. Remaining atoms in the  $|1\rangle$  state are depumped into the  $^1S_0$  ground state for fluorescence imaging. The excitation of a Rydberg-pair state is inferred by conditioning the remaining atom population after a given experimental sequence on pair-wise atom loss. An exemplary pair-state spectrum close to the  $|54.28, L = 0, F = 1/2, -1/2\rangle^{\otimes 2}$  asymptotic pair state is given in Fig. 9c. For a given optical tweezer separation, we observe an increase in pairwise atom loss when tuning the two-photon transition over a Rydberg pair state. The pair-state resonance shifts to larger two-photon detuning when reducing the tweezer separation, indicating

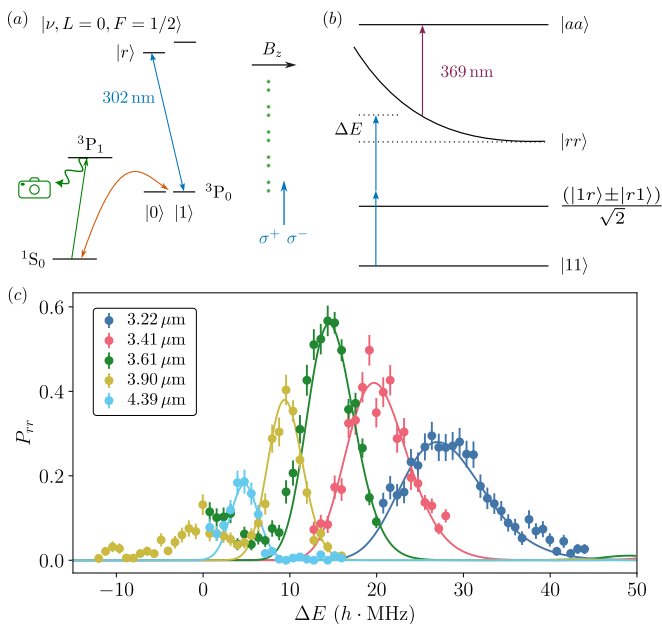


Figure 9. (a) Single-atom transition scheme for measuring interactions between pairs of Rydberg atoms in an optical tweezer setup [40]. The  $^{171}\text{Yb}$  atoms are prepared states in the  $|1\rangle$  sublevel of the  $^3P_0$  metastable state. Transitions into the  $|\nu, L = 0, F\rangle$  Rydberg state are driven by a single-photon transition (302 nm). For rearrangement and readout, the atoms are imaged by collecting the fluorescence on the  $|^1S_0\rangle \leftrightarrow |^3P_1\rangle$  transition. (b) Scheme for measuring Rydberg-Rydberg interactions between pairs of single atoms trapped in optical tweezer arrays. (c) Experimental pair-state spectra (solid dots), obtained by recording the probability of pair-wise loss from tweezers in fluorescence image as a function of two-photon detuning and tweezer separation. The experimental spectra are compared to simulated pair spectra  $S(E)$  (solid lines) obtained from Eq. (C1), as explained in the text.

a larger interaction between the two Rydberg atoms. We fit the observed pair-state spectra using a Gaussian line shape model. The resulting center frequency of the fits are presented in Fig. 6 and Fig. 7.

On top of the shift of the pair-state resonance, we also observe a broadening. We attribute the observed broadening to the spatial fluctuations of the single atoms in the optical tweezers ( $T \approx 3 \mu\text{K}$ ). Due to the spatial fluctuations of the atoms, the linewidth of the pair-state resonance is affected by the gradient of the interaction potential, which increases towards shorter internuclear separations. To model the effect of fluctuating internuclear separations in the optical tweezers, we simulate the pair-state spectra  $S(E)$

$$S(E) \propto \sum_{\Phi} \mathcal{G}(E - E_{\Phi}(R), \sigma_E) \mathcal{T}(R - \tilde{R}, \sigma_R) \mathcal{O}_{\Phi, \Phi'}(R), \quad (\text{C1})$$

where the sum runs over all relevant pair state  $\Phi$  coupled to the target state  $\Phi'$ ,  $E_{\Phi}(R)$  is the internuclear-separation-dependent pair-state energy,  $\tilde{R}$  is the mean

internuclear separation,  $\mathcal{G}(E - E_{\Phi}(R), \sigma_E)$  is a function describing the experimental linewidth of the spectrum in the absence of any broadening,  $\mathcal{T}(R - \tilde{R}, \sigma_R)$  is a function describing the distribution of internuclear separation around a mean separation  $\tilde{R}$ , and  $\mathcal{O}_{\Phi, \Phi'}(R)$  is the overlap coefficient.

For the case presented in Fig. 9c, the line broadening can be reproduced by assuming a normal distribution in the internuclear separations with standard deviation of 100 nm. This is close to the expected distance fluctuations of approximately 50 nm between two atoms confined in optical tweezers with radial and axial trap frequencies of  $\omega_r = 60 \text{ kHz}$  and  $\omega_z = 10 \text{ kHz}$ , respectively.

## Appendix D: Additional spectroscopic data and models for $^{174}\text{Yb}$

In this appendix, we give additional details of the spectroscopic measurements and MQDT model development for  $^{174}\text{Yb}$ . We also make comparisons between the MQDT model and previously measured quantities, including singlet-triplet mixing in the  $^1,^3P_1$  and  $^1,^3D_2$  series, and diamagnetic shifts in the P series.

### 1. $^3S_1$ and $^1S_0$

For the  $n^1S_0$  Rydberg series of  $^{174}\text{Yb}$ , we adapt the six-channel MQDT model presented in previous work [49]. We refit the MQDT model parameters of the  $^1S_0$ ,  $^1,^3D_2$ ,  $^1,^3P_1$  Rydberg series in a simultaneous, 42-parameter fit to the previously measured [46, 49, 50, 53–56, 58] and newly measured data presented in Tabs. XII to XIX, leveraging the higher precision microwave measurements between S, D, and P Rydberg states. The resulting MQDT models are presented in Tabs. II to IV.

For the  $n^3S_1$  with  $n > 28$ , we adapt the single-channel quantum defect model with a Rydberg-Ritz expansion for the energy-dependent quantum defect presented in Ref. [29].

### 2. $^1P_1$ and $^3P_1$

Here we introduce a six-channel MQDT model for the  $^1,^3P_1$  Rydberg series of  $^{174}\text{Yb}$ . Compared to the five-channel model presented in Ref. [50], we introduce a sixth perturbing channel, which lies energetically above the first ionization limit of  $^{174}\text{Yb}$ . In addition, we introduce singlet-triplet mixing between the  $^1P_1$  and  $^3P_1$  explicitly, by introducing a rotation to the  $U_{i\alpha}$  matrix,  $\theta_{12}$  whose value is constrained by the Stark shift of the  $^1S_0$  state, as explained in Sec. II.

We extend the previously measured state energies of  $^1,^3P_1$  [50, 56] (Tab. XIX), by measuring microwave transition frequencies between  $n^1,^3P_1$  and  $n'^1,^3D_2$  or  $n'^1S_0$

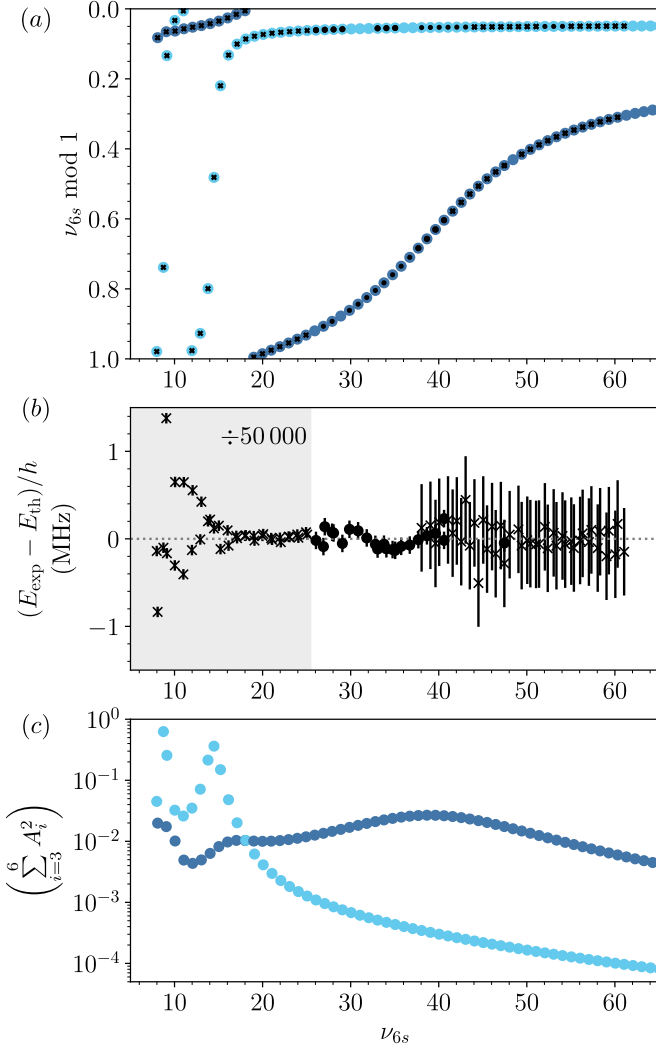


Figure 10. (a) Lu-Fano-type plot of the  $^{174}\text{Yb } 1,3P_1$  Rydberg series. The theoretical bound states with dominant singlet and triplet character are indicated by light and dark blue dots, respectively. Experimentally observed states are indicated by black crosses (Refs.[50, 56]) and black dots (this work). (b) Deviation between experimental and theoretical state energies. The energy deviations and error bars in the gray shaded area are scaled by a factor of 50 000 to improve visibility of the much smaller errors observed on the microwave transitions. (c) Perturbing channel fraction  $\sum_{i=3}^6 A_i^2$  of the dominantly singlet (light blue) and triplet (dark blue) Rydberg states.

Rydberg states in the range of  $31 \leq n \leq 43$ , as summarized in Tabs. XVII and XVIII. In the fitting procedure, we optimize the 42 parameters of the  $1S_0$ ,  $1,3D_2$ ,  $1,3P_1$  MQDT models in a simultaneous fit to the data presented in Tabs. XII to XIX. The resulting MQDT models are presented in Tabs. II to IV.

The presented MQDT model correctly predicts the energies of the highly excited  $n^{1,3}P_1$  Rydberg states. However, below  $\nu < 15$ , significant deviations between the experimental and theoretical energies occur. This could

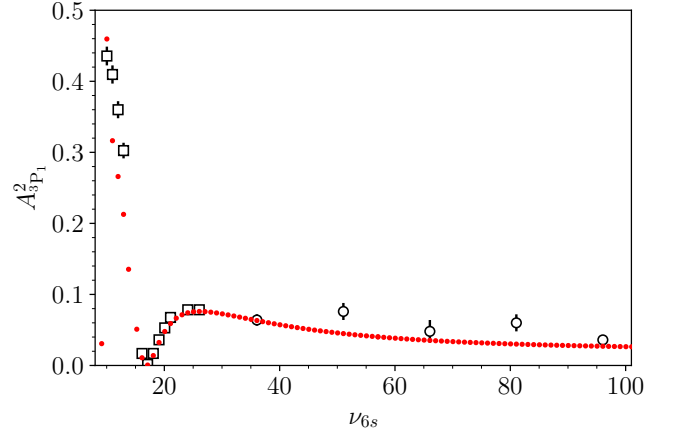


Figure 11.  $6sn^3P_1$  character ( $A_{3P_1}^2$ ) in  $6sn^1P_1$  Rydberg states of  $^{174}\text{Yb}$ . The open black squares correspond to experimental values obtained by measurements of the hyperfine-structure of  $^{171}\text{Yb}$  and  $^{173}\text{Yb } 1,3P_1$  Rydberg states from Ref. [89]. The open black circles correspond to experimental values obtained by measuring diamagnetic shifts taken from Ref. [57]. The full red circles correspond to theoretical values of  $A_{3P_1}^2$  as obtained from the MQDT model presented in Tab. IV.

be due to unaccounted perturbing channels, either directly in the low- $\nu$  regime, or in the high- $\nu$  regime, with the current MQDT model parameters overcompensating trends in the quantum defects for the more accurately determined Rydberg states at high  $\nu$ .

The breakdown of pure  $LS$  coupling in the  $1,3P_1$  Rydberg channels is quantified by measuring the static dipole polarizabilities of  $n^1S_0$  Rydberg states in the vicinity of a near degeneracy with dominantly  $n^3P_1$  Rydberg states, as discussed in the main text. To obtain the best agreement between the experimental and theoretical static polarizabilities of the  $n^1S_0$  Rydberg states, an energy dependent singlet-triplet mixing angle (refer to Eq. (A7)) had to be introduced. The resulting MQDT parameters are presented in Tab. IV.

With the obtained  $J = 1$  (odd parity) MQDT model for  $^{174}\text{Yb}$  and using Eq. A12, we can estimate the  $6sn^3P_1$  channel contribution into the nominally  $n^1P_1$  Rydberg states. The resulting values are presented in Fig. 11 and compared to values obtained from previous measurements of diamagnetic shifts, as presented in Ref. [57] and from previous hyperfine-structure measurements in  $^{171}\text{Yb}$  and  $^{173}\text{Yb}$ , as presented in Ref. [89]. The theoretically obtained values for the triplet contribution to the  $n^1P_1$  Rydberg states agree well with the previously reported values between  $20 \leq n \leq 100$ , but with significantly reduced uncertainties, highlighting the sensitivity of measuring matrix elements through Stark shifts close to near degeneracies.

As an additional check of the validity of the model, we compare the predicted Zeeman and diamagnetic shifts in very large magnetic fields to a previous experimental

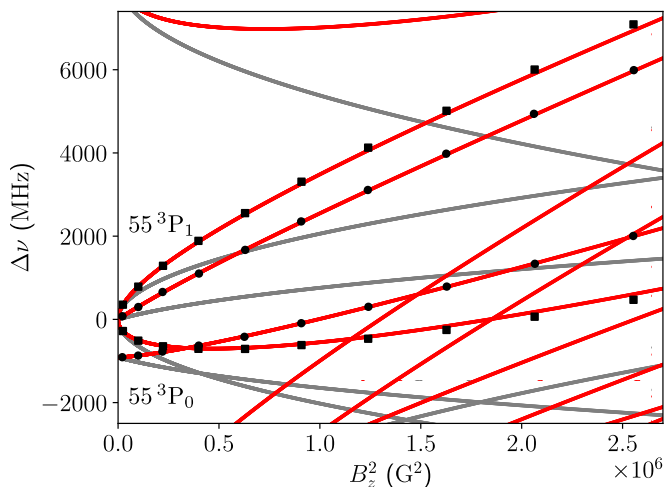


Figure 12. Zeeman shifts of  $^{174}\text{Yb}$  Rydberg states near the  $55\ ^3P_1$  state. The red and gray curves correspond Zeeman shift calculations with and without diamagnetism, respectively. The near degeneracy of the  $55\ ^3P_0$  and  $55\ ^3P_1$  states, leads to a strong interaction between the  $55\ ^3P_1(m_J = 0)$  and  $55\ ^3P_0(m_J = 0)$  sublevels. The black circles and squares correspond to experimentally observed Zeeman shifts extracted from Fig. 3 of Ref. [57] for the  $m_J = 0$  and  $m_J = \pm 1$  sublevels, respectively.

measurement from Ref. [57]. In that work, the measured energies were fit with a phenomenological model to extract the singlet-triplet splitting for that  $n$ . In Fig. 12, we show the prediction of the MQDT model with no free parameters, finding excellent agreement.

### 3. $^3P_2$

Here, we introduce a four-channel MQDT model for  $^3P_2$  Rydberg states of  $^{174}\text{Yb}$ . In comparison to the previously presented three-channel MQDT model from Ref. [48], we introduce an additional channel with a perturbing state above the first ionization limit.

The MQDT model parameters are optimized in a weighted least-square procedure. The Rydberg state energies includes in the fitting procedure include previously measured state energies of  $^3P_2$  by laser [56] and microwave spectroscopy [50], as well as newly measured microwave transition frequencies between  $n\ ^3P_2$  and  $n'\ ^3D_2$  Rydberg states in the range of  $31 \leq n \leq 43$ . The included Rydberg state energies are summarized in Tab. XXI and Tab. XX. The resulting MQDT model parameters are presented in Tab. V.

As depicted in Fig. 13(a) and (b), the newly introduced MQDT model for  $^3P_2$  captures the energies of the highly excited  $n\ ^3P_2$  Rydberg state quantitatively, but only qualitatively captures the energies of the states in the strongly perturbed range below  $\nu \approx 15$ .

Fig. 13c, depicts the contribution of the core excited channels, which are below  $10^{-3}$  for states with  $\nu > 20$ ,

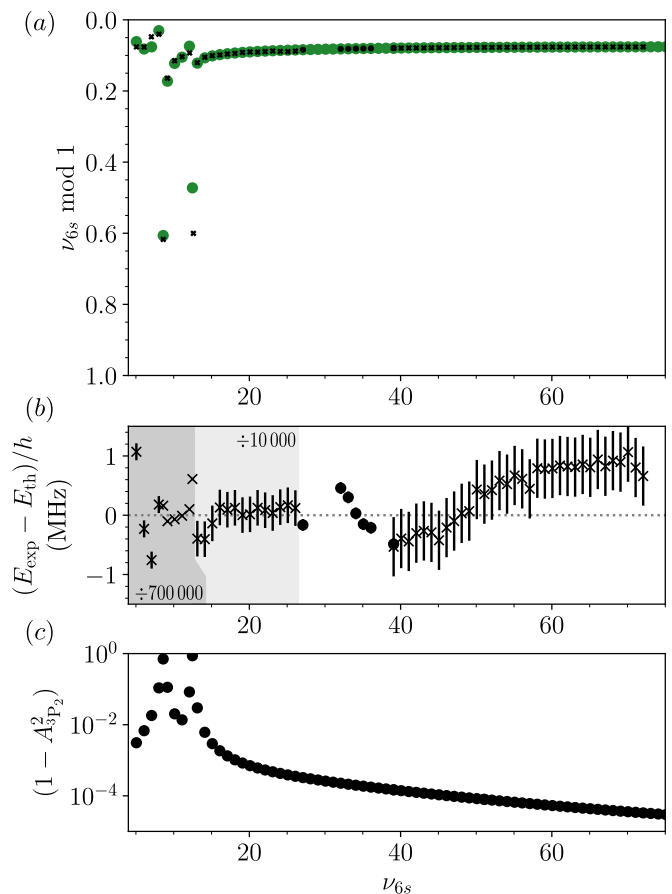


Figure 13. Lu-Fano-type plot of the  $^{174}\text{Yb}\ ^3P_2$  Rydberg series. The theoretical bound states are indicated by green dots. Experimentally observed states are indicated by black dots (Refs.[50, 56]) and dots (this work). (b) Deviation between experimental and theoretical state energies. The energy deviations and error bars in the light (dark) gray shaded area are scaled by a factor of 10 000 (700 000) to improve visibility of the much smaller errors observed on the microwave transitions. (c) Perturber fraction  $(1 - A_{3P_2}^2)$  of the Rydberg states in the  $(J = 2)^\circ$  Rydberg series.

confirming a mostly unperturbed  $^3P_2$  Rydberg series. Series perturbers can shorten the lifetime of Rydberg states even at high  $n$ , by introducing an additional decay channel proportional to  $\sum A_i \Gamma_i$ , where  $\Gamma_i$  is the decay rate of the perturbing states. Since  $\Gamma_i$  for low-lying atomic states can be substantially faster than for Rydberg states, even a small admixture can significantly alter the lifetime. We note that Ref. [29] measured the lifetime of the  $74\ ^3P_2$  state to be  $83(5)\ \mu\text{s}$ , which is close to but slightly shorter than the lifetime predicted for a P state of  $^{87}\text{Rb}$  with a similar quantum number (approximately  $200\ \mu\text{s}$  at  $T = 300\ \text{K}$  [112]). This is qualitatively consistent with the modeled small but non-zero perturbation of this series. A quantitative assessment will require predictions for matrix elements and decay rates of the perturbing states, which is a subject for future work.

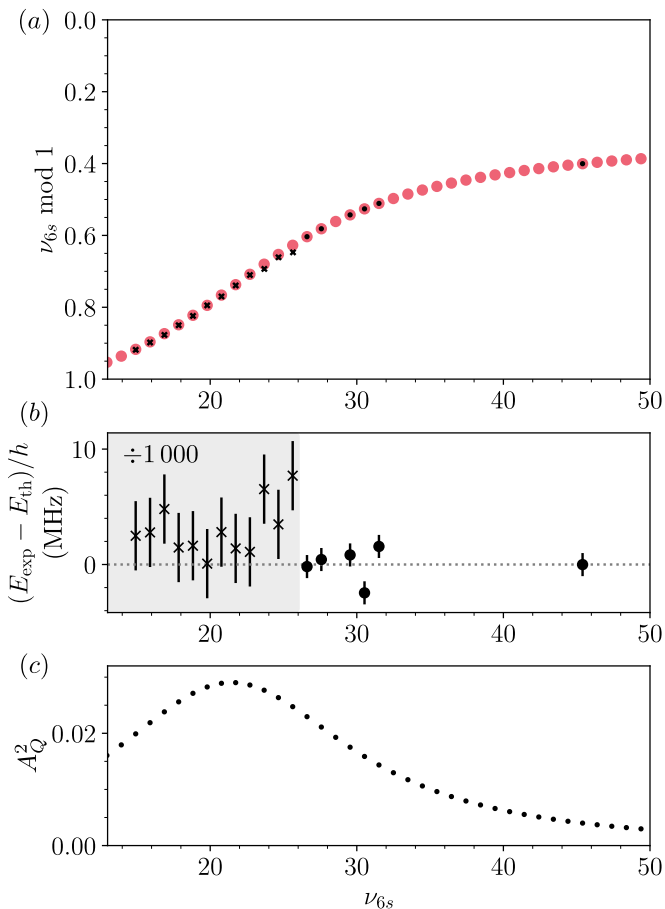


Figure 14. Lu-Fano-type plot of the  $^{174}\text{Yb } ^3P_0$  Rydberg series. The theoretical bound states are indicated by red dots. Experimentally observed states are indicated by black crosses (Ref.[56]) and dots (this work). (b) Deviation between experimental and theoretical state energies. The energy deviations and error bars in the gray shaded area are scaled by a factor of 1000 to improve visibility of the much smaller errors observed on the microwave transitions. (c)  $Q$  channel contribution  $A_Q^2$  to the  $n^3P_0$  Rydberg states.

#### 4. $^3P_0$

Here, we present a two-channel MQDT model for the  $n^3P_0$  Rydberg states of  $^{174}\text{Yb}$ . A two-channel model suffices to reproduce the observed states at high- $n$ , though we believe additional channels will eventually be necessary to explain the full series. We have no direct information about the nature of the perturbing series and refer to it as  $Q$ . The MQDT model parameters are optimized in a weighted least-square fit to both previously measured state energies by laser spectroscopy [56] and newly measured state energies from microwave spectroscopy, summarized in Tab. XXIII and Tab. XXII, respectively.

The  $n^3P_0$  Rydberg states are inaccessible by direct one-photon microwave transitions from laser accessible  $n^1S_0$  and  $n^{1,3}D_2$  Rydberg states. Instead, we perform spectroscopy on  $n^3P_0$  Rydberg states of  $^{174}\text{Yb}$ , by utiliz-

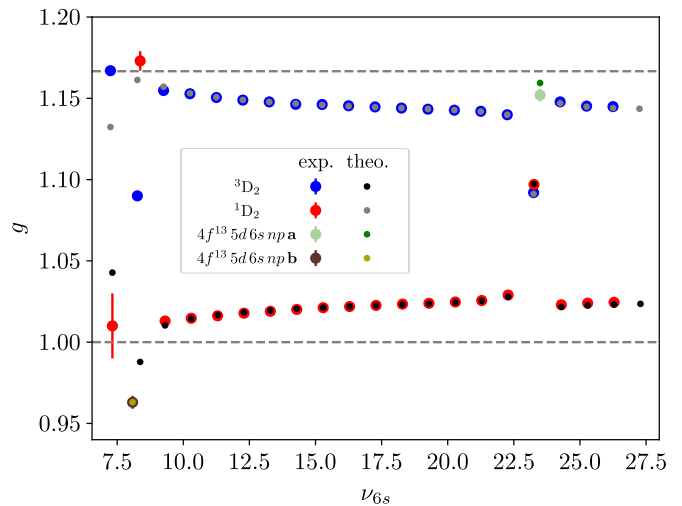


Figure 15.  $g$ -factors of the  $^{1,3}D_2$  and its perturbers as taken from Ref. [59] and calculated with the MQDT presented in Tab. III. The gray dashed lines indicate the values for  $g$  factors in pure  $LS$  coupling.

ing the Autler-Townes splitting on a probe transition. To this extent, we monitor the resonant population transfer on the two-photon  $n^3D_2 \rightarrow n'^3S_1$  microwave transition as a function of the frequency of a simultaneously applied microwave pulse coupling the  $n^3S_1 \rightarrow n''^3P_0$  transition. The observed  $n^3P_0 \leftrightarrow n'^3D_2$  intervals are summarized in Tab. XXII. We recorded a total of six transitions to  $n^3P_0$  Rydberg states in the range of  $31 \leq n \leq 49$ , which were particularly necessary to determine the energy dependence of the strongly perturbed  $^3P_0$  series. The results of this measurement, together with previous three-photon laser spectroscopy [56] are presented in Tab. XXII and Tab. XXIII, respectively.

The obtained MQDT model is summarized in Tab. VI and presented in a Lu-Fano-like plot in Fig. 14. The MQDT model represents the experimental data well within the experimental uncertainties over a range of  $18 \leq n \leq 50$ .

The contributions of perturbing channel  $Q$  into the  $n^3P_0$  Rydberg states is presented in Fig. 14c. The channel contribution is spread out over a wide range of principal quantum numbers and reaches a maximum value of approximately 3% at  $n = 26$ . This is consistent with a significantly reduced lifetime of the  $74^3P_0$  Rydberg state ( $14(4) \mu\text{s}$ ) observed in Ref. [29]. Further refinement of the MQDT model for this series at low- $n$  will be useful to understand the lifetimes of this series quantitatively.

#### 5. $^1D_2$ and $^3D_2$

Here, we present a five-channel MQDT model for the  $n^{1,3}D_2$  Rydberg states of  $^{174}\text{Yb}$ . We adapt this model from Ref. [49], but we refit the MQDT model parameters of the  $^1S_0$ ,  $^{1,3}D_2$ ,  $^{1,3}P_1$  Rydberg series in a si-



Table I. Rydberg-Ritz expansion coefficients of the  $n^3D_1$  and  $n^3D_3$  Rydberg states of Yb, inferred from laser spectroscopy of D  $F = 3/2$  and  $F = 5/2$  Rydberg states of  $^{171}\text{Yb}$ .

	$n^3D_1$	$n^3D_3$
$\mu_0$	2.752 580 93	2.728 953 15
$\mu_2$	0.3826	-0.2065
$\mu_4$	-483.1	220.5

multaneous, 42-parameter fit to the previously measured [46, 49, 50, 53–56, 58] and newly measured data presented in Tabs. XII to XIX. The resulting MQDT models are presented in Tabs. II to IV.

In addition, to account for singlet-triplet mixing, the model includes a rotation around the  $^1D_2$  and  $^3D_2$  channels in the  $U_{i\alpha}$  matrix. To determine the magnitude of the singlet-triplet mixing, we use the  $g$ -factors of the  $n^{1,3}D_2$  Rydberg series and its perturbers measured by Zerne and co-workers [59] to obtain a value for the singlet-triplet mixing angle between the  $^1D_2$  and  $^3D_2$  channels. To that extent, we vary the energy-dependent mixing angle  $\theta_{12}$  (Eq. A7), and calculate the  $g$ -factor in using Eq. (22) of Ref. [44]. In addition, we treat the  $g$ -factors of the perturbing states with only partially known electronic configuration as parameters of our model. To obtain the best agreement between experiment and theory, we introduce an energy dependent mixing angle, as defined in Eq. (A7). The results of the fit are presented in Fig. 15 and the MQDT model is summarized in Tab. III. From our MQDT model, we estimate a triplet character in the  $^1D_2$  series between 14.0% and 15.5% for  $30 \leq n \leq 100$ . This is in agreement with an estimated triplet admixture into the  $36^1D_2$  state of 19(6)% presented in Ref. [58].

## 6. $^3D_1$ and $^3D_3$

The  $^3D_1$  and  $^3D_3$  Rydberg states of  $^{174}\text{Yb}$  are not directly laser accessible by two-photon laser spectroscopy through the  $6s6p^1P_1$  intermediate state. A few  $^3D_1$  and  $^3D_3$  Rydberg states have been observed in Ref. [61] and Ref. [113]. For the purposes of this work, we infer the quantum defects of the  $^3D_1$  and  $^3D_3$  from laser accessible D  $F = 3/2$  and D  $F = 5/2$  Rydberg states in  $^{171}\text{Yb}$ , as discussed in App. E3.

The quantum defects of the two series are well described by a Rydberg-Ritz model

$$\mu(n) = \mu_0 + \frac{\mu_2}{(n - \mu_0)^2} + \frac{\mu_4}{(n - \mu_0)^4} \quad (\text{D1})$$

for the states studied in this work with  $\nu > 30$ . The obtained expansion coefficients for the two series are presented in Tab. I.

The inferred quantum defects for the  $n^3D_3$  Rydberg series, are consistent with the assignment of measure-

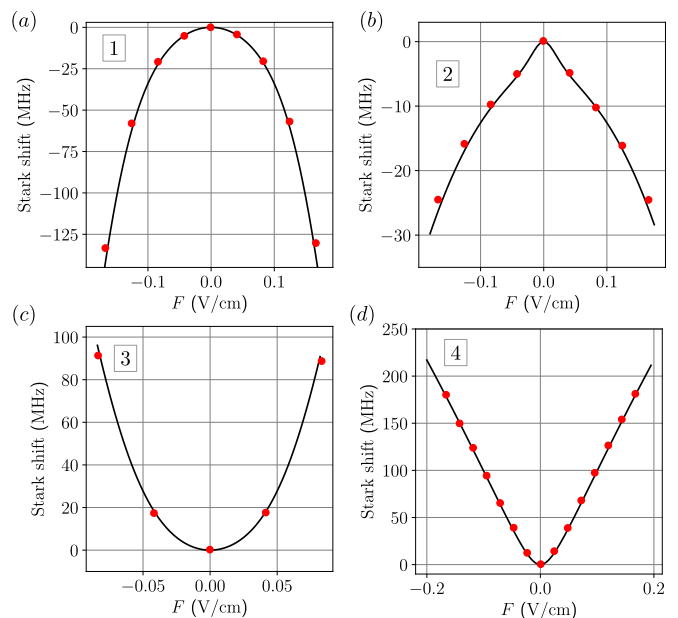


Figure 16. Experimental Stark shifts (red dots) of  $^{171}\text{Yb}$   $|\nu_{F_c=1}, L=0, F=1/2\rangle$  Rydberg states with (a)  $\nu_{F_c=1} \approx 65.68$ , (b)  $\nu_{F_c=1} \approx 66.68$ , (c)  $\nu_{F_c=1} \approx 67.68$ , (d)  $\nu_{F_c=1} \approx 64.09$  compared with theoretical Stark shifts (solid black line). The extracted experimental Stark shifts at low electric field are presented in subpanels Fig 5 (d) and (e) as indicated by labels 1 to 4.

ments in  $^{174}\text{Yb}$  presented in Ref. [61] to within the stated measurement uncertainties of 10 MHz. The inferred quantum defects for the  $n^3D_1$  Rydberg series are consistent with the assignment of measurements in  $^{174}\text{Yb}$  presented in Refs. [61, 113], but the Rydberg state energies deviate up to 40 MHz from the values presented in Ref. [61], which could be due to the limited number of D  $F = 3/2$  states with dominant  $^3D_1$  character observed in this work.

## Appendix E: Additional spectroscopic data and models for $^{171}\text{Yb}$

In this appendix, we give additional details about the spectroscopic measurements and MQDT model development for  $^{171}\text{Yb}$ .

### 1. S $F = 1/2$ and $F = 3/2$ states

There is only a single  $F = 3/2$  series with  $L = 0$ , which converges to the  $F_c = 1$  threshold and has  $^3S_1$  character. We have measured the energy spacing between several S  $F = 3/2$  Rydberg states and S  $F = 1/2$  or D  $F = 5/2$  Rydberg states using microwave spectroscopy in an atomic beam. The experimental transition frequencies are presented in Tab. XXV. Due to the small number of measured transitions to S  $F = 3/2$  Rydberg states, we model

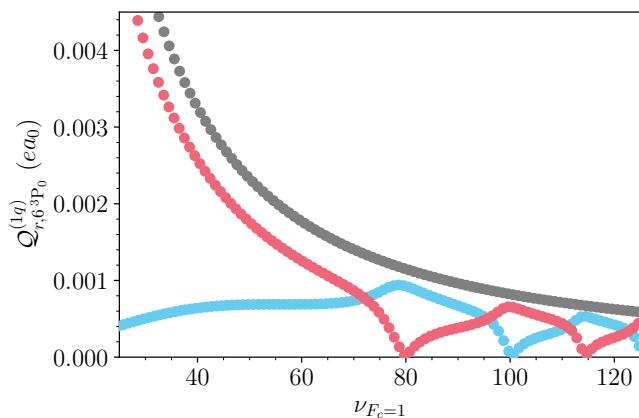


Figure 17. Transition dipole matrix elements  $Q_{r,6^3P_0}$  between the  $6s6p^3P_0(m_F = +1/2)$  metastable and Rydberg state  $r$ , where  $r = |\nu, L = 0, F = 3/2, m_F = +3/2\rangle$  (gray) and  $r = |\nu, L = 0, F = 1/2, m_F = -1/2\rangle$  (red and blue, color code as in Fig. 3).

this series using the Rydberg-Ritz model introduced for  $^{174}\text{Yb}$  [29] with parameters optimized in the fit to the  $S F = 1/2$  Rydberg states (presented in Tab. VII). The experimental and theoretical energies of the  $S F = 3/2$  Rydberg series agree to within the uncertainty of the initial state energy used in the microwave spectroscopy.

In Fig. 5, we presented measurements of Stark shifts of  $S F = 1/2$  Rydberg states. Most Rydberg states exhibit a quadratic Stark shift at small electric fields, common for non-degenerate Rydberg states, and we extract a static polarizability by a quadratic fit to the observed Stark shift. However, for cases in which the Rydberg state of interest is very nearly degenerate with other Rydberg states (shaded gray in Fig. 5), the Stark shift is not quadratic even at very small electric fields. In Fig. 16, we present a field-dependent shift measurement together with a non-perturbative calculation, finding excellent agreement.

Fig. 17 illustrates calculated transition dipole matrix elements from  $6s6p^3P_0$  metastable state into  $S (F = \{1/2, 3/2\})$  Rydberg states of  $^{171}\text{Yb}$ , which are computed using the single active electron approximation. The matrix elements to  $S (F = 1/2)$  Rydberg states are generally smaller than the matrix elements to  $S (F = 3/2)$  Rydberg states. However, at low effective principal quantum numbers, the transition dipole matrix element to one of the two  $S (F = 1/2)$  Rydberg series is still comparable to the  $S (F = 3/2)$  case, due to a dominant triplet character. At larger effective principal quantum numbers, particularly close to near degeneracies between the two  $S (F = 1/2)$  channels, the matrix elements varies strongly with the effective principal quantum number, indicating strong hyperfine-induced singlet-triplet mixing.

## 2. $P F = 1/2, F = 3/2,$ and $F = 5/2$ states

Here, we introduce MQDT models for  $P F = 1/2, F = 3/2,$  and  $F = 5/2$  Rydberg states of  $^{171}\text{Yb}$ . There are seven  $L = 1$  series in  $^{171}\text{Yb}$ . In  $LS$  coupling, they can be described as  $^3P_0(F = 1/2), ^1P_1(F = \{1/2, 3/2\}), ^3P_1(F = \{1/2, 3/2\})$  and  $^3P_2(F = \{3/2, 5/2\})$ . As in the case of the  $|\nu, L = 0, F = 1/2\rangle$ , we use the  $^{174}\text{Yb}$  MQDT models of  $^{1,3}P_1$  and  $^3P_0$  (for  $F = 1/2$ ) and  $^{1,3}P_1$  and  $^3P_2$  (for  $F = 3/2$ ) as a basis for the  $^{171}\text{Yb}$  MQDT model and introduce the hyperfine coupling in the ion-core using a frame transformation (see App. A 1).

We optimize the MQDT model parameters for both the  $F = 1/2$  and  $F = 3/2$  series using a weighted, least-squared fitting procedure to a dataset containing Rydberg state energies obtained in this work from microwave spectroscopy (Tab. XXVI and Tab. XXVIII) and from previous laser spectroscopy reported Ref. [89] (Tab. XXVII and Tab. XXIX). In our fitting procedure, we treat the MQDT model parameters originating from  $^{174}\text{Yb}$  that occur in both the  $P F = 1/2$  and  $F = 3/2$   $^{171}\text{Yb}$  as a single parameter. The resulting MQDT parameters for  $F = 1/2$  and  $F = 3/2$  are presented in Tab. VIII and Tab. IX, respectively.

The state energies reported in Tab. XXVII and Tab. XXIX are obtained from isotope shift and hyperfine splitting measurements of the  $n^1P_1$  and  $n^3P_{0,1,2}$  Rydberg states using three-photon laser spectroscopy, as presented in previous work [89]. The absolute uncertainty of the Rydberg state energies presented in Ref. [89] is stated to be 4 GHz, but we find that the stated (relative) hyperfine splittings are more precise. To minimize absolute errors on the measured energies of the  $^{171}\text{Yb}$   $P F = 1/2$  and  $F = 3/2$  Rydberg states, we introduce the following treatment.

For Rydberg states with principal quantum number  $n > 20$ , we infer absolute energies of  $^{171}\text{Yb}$   $P F = 1/2$  and  $F = 3/2$  Rydberg states from the measured hyperfine splittings by (1) referencing to theoretical energies of  $^{174}\text{Yb}$   $n^{1,3}P_1$  Rydberg states, as obtained from the MQDT model presented in Tab. IV and (2) by accounting for a constant energy offset added, to minimize deviations between the inferred energies from laser spectroscopy and microwave intervals to the  $|\nu, L = 0, F = 1/2\rangle$  Rydberg states.

For Rydberg states with principal quantum number  $n \leq 20$ , we (1) reference the hyperfine splitting measurements to the observed absolute energies of  $^{176}\text{Yb}$ , as presented in Ref. [89] and (2) add a constant energy offset to all Rydberg states to minimize the deviations between this treatment and the treatment for  $n > 20$  at large principal quantum numbers.

The resulting inferred absolute energies of  $|\nu, L = 1, F = 1/2\rangle$  and  $|\nu, L = 1, F = 3/2\rangle$  Rydberg states are presented in Tabs. XXVII and XXIX.

The  $F = 5/2$  series with  $L = 1$  converges to the  $F_c = 1$  threshold. We have not directly measured any  $^{171}\text{Yb}$   $L = 1, F = 5/2$  states and therefore, we model this series

using the MQDT model for the  $^3P_2$  series presented for  $^{174}\text{Yb}$  in the previous section, with optimized parameters obtained from the fit to the  $|\nu, L = 1, F = 3/2\rangle$  Rydberg states presented in Tab. IX.

### 3. D $F = 1/2$ , $F = 3/2$ , $F = 5/2$ , and $F = 7/2$

There are eight  $L = 2$  series in  $^{171}\text{Yb}$ . In  $LS$  coupling, they can be described as  $^3D_1(F = \{1/2, 3/2\})$ ,  $^1D_2(F = \{3/2, 5/2\})$ ,  $^3D_2(F = \{3/2, 5/2\})$  and  $^3D_3(F = \{5/2, 7/2\})$ . In  $^{174}\text{Yb}$ , spin-orbit coupling mixes the two  $J = 2$  series as discussed in Section II; in  $^{171}\text{Yb}$ , hyperfine coupling additionally mixes the three  $F = 3/2$  series and the three  $F = 5/2$  series.

As in the case of the  $|\nu, L = 0, F = 1/2\rangle$  Rydberg states, we measure the energies of  $|\nu, L = 2, F = 3/2\rangle$  and  $|\nu, L = 2, F = 5/2\rangle$  Rydberg states by laser spectroscopy by a two-photon transition via the  $6s6p^1P_1(F = 3/2)$  intermediate state. Transition frequencies to all measured  $|\nu, L = 2, F = 3/2\rangle$  and  $|\nu, L = 2, F = 5/2\rangle$  states are summarized in Tabs. XXX and XXXI and plotted on a Lu-Fano-type plot in Fig. 18a.

We use a least-square procedure to obtain MQDT parameters for the  $F = 3/2$  and  $F = 5/2$  series. As in the case of the P Rydberg states, we treat the MQDT parameters that originate from the  $^{174}\text{Yb}$  models and occur in both the  $F = 3/2$  and  $F = 5/2$  MQDT models as a single parameter. The developed MQDT models summarized in Tabs. X and XI describe both the Rydberg state energies and the measured  $g$ -factors well over nearly the entire energy range. Significant deviations for both  $F = 3/2$  and  $F = 5/2$  occur towards low effective principal quantum numbers. These deviations could arise from unaccounted perturbers in the MQDT or from channel interactions with additional  $(F = 3/2)^e$  Rydberg series. In the case of  $F = 5/2$ , we additionally observe slight deviations between experiment and theory, that could be caused by uncompensated stray electric fields.

There is only a single D Rydberg series with  $F = 1/2$  ( $F = 7/2$ ), converging to the  $F_c = 1$  threshold with  $^3D_1$  ( $^3D_3$ ) character. Because we use the  $6s6p^1P_1(F = 3/2)$  (dominantly singlet character) state as an intermediate state, the  $|\nu, L = 2, F = 1/2\rangle$  (dominantly triplet character) and the  $|\nu, L = 2, F = 7/2\rangle$  Rydberg states are inaccessible by direct laser spectroscopy. However, the fitted  $F = 3/2$  and  $F = 5/2$  series MQDT models include a Rydberg-Ritz model for the  $^3D_1$  and  $^3D_3$  series (Tab. X and Tab. XI). Therefore, we use this model to predict the positions of the  $F = 1/2$  and  $F = 7/2$  series.

### Appendix F: Polarizability trends in $^{174}\text{Yb}$ and $^{171}\text{Yb}$ S Rydberg states

In Fig. 19 and Fig. 20 we present predicted polarizabilities for  $L = 0$  states of both  $^{174}\text{Yb}$  and  $^{171}\text{Yb}$ . We note several interesting features. First, the  $^{174}\text{Yb}$   $^3S_1$

polarizability is positive at low- $n$  and negative at high- $n$ , as the strongly perturbed  $^3P_0$  and  $^3P_1$  series cross the  $^3S_1$  series in energy. Second, the  $^{171}\text{Yb}$  polarizabilities have a much more complex behavior, with multiple sign changes resulting from a number of resonances.

### Appendix G: Rydberg-Rydberg-interaction trends

The van der Waals coefficients  $C_6$  for the  $L = 0$  Rydberg states of  $^{174}\text{Yb}$  and  $^{171}\text{Yb}$  Rydberg states are presented in Fig. 21. In  $^{174}\text{Yb}$ , the  $C_6$  coefficients of  $6sns^1S_0$  Rydberg series are unusually small, consistent with the single-channel calculations of Ref. [93] (we additionally note a Förster resonance around  $\nu \approx 50$ , which arises from the inclusion of singlet-triplet mixing in the  $^1,^3P_1$  Rydberg series). In contrast, the  $C_6$  coefficients of  $6sns^3S_1$  Rydberg states of  $^{174}\text{Yb}$  are larger, consistent with previous estimates [29] and observations [102], but calculated here for the first time. The  $C_6$  coefficients of this series are the same magnitude as for the  $ns_{1/2}$  Rydberg states of rubidium, but with opposite sign (*i.e.*, attractive).

As in the case for  $^1S_0$  Rydberg states of  $^{174}\text{Yb}$ , the singlet connected  $|\nu, L = 0, F = 1/2\rangle$  Rydberg states of  $^{171}\text{Yb}$  (blue dots in Fig. 21) have small  $C_6$  coefficients in the range  $40 \leq \nu \leq 70$ . The triplet connected  $|\nu, L = 0, F = 1/2, m_F\rangle$  states have  $C_6$  coefficients that are approximately half the magnitude of Rb, with the same sign (*i.e.*, repulsive).

As pointed out in Section IV,  $|\nu, L = 0, F = 3/2\rangle$   $|\nu, L = 0, F = 3/2\rangle$  Rydberg pair states of  $^{171}\text{Yb}$  have small Förster defects over a large range of effective principal quantum number  $\nu$  (Fig. 22). It is surprising that the Förster defect is so small over such a large range of  $\nu$ , which results from a combination of series perturbers and hyperfine coupling. To calculate a meaningful asymptotic  $C_6$  coefficient, we calculate the pair potentials under a 30 G magnetic field to lift the degeneracy somewhat (Fig. 21c). The extracted  $C_6$  coefficients are not meaningful at short separations, which are dominated by resonant dipole-dipole interaction, as shown in Fig. 7.



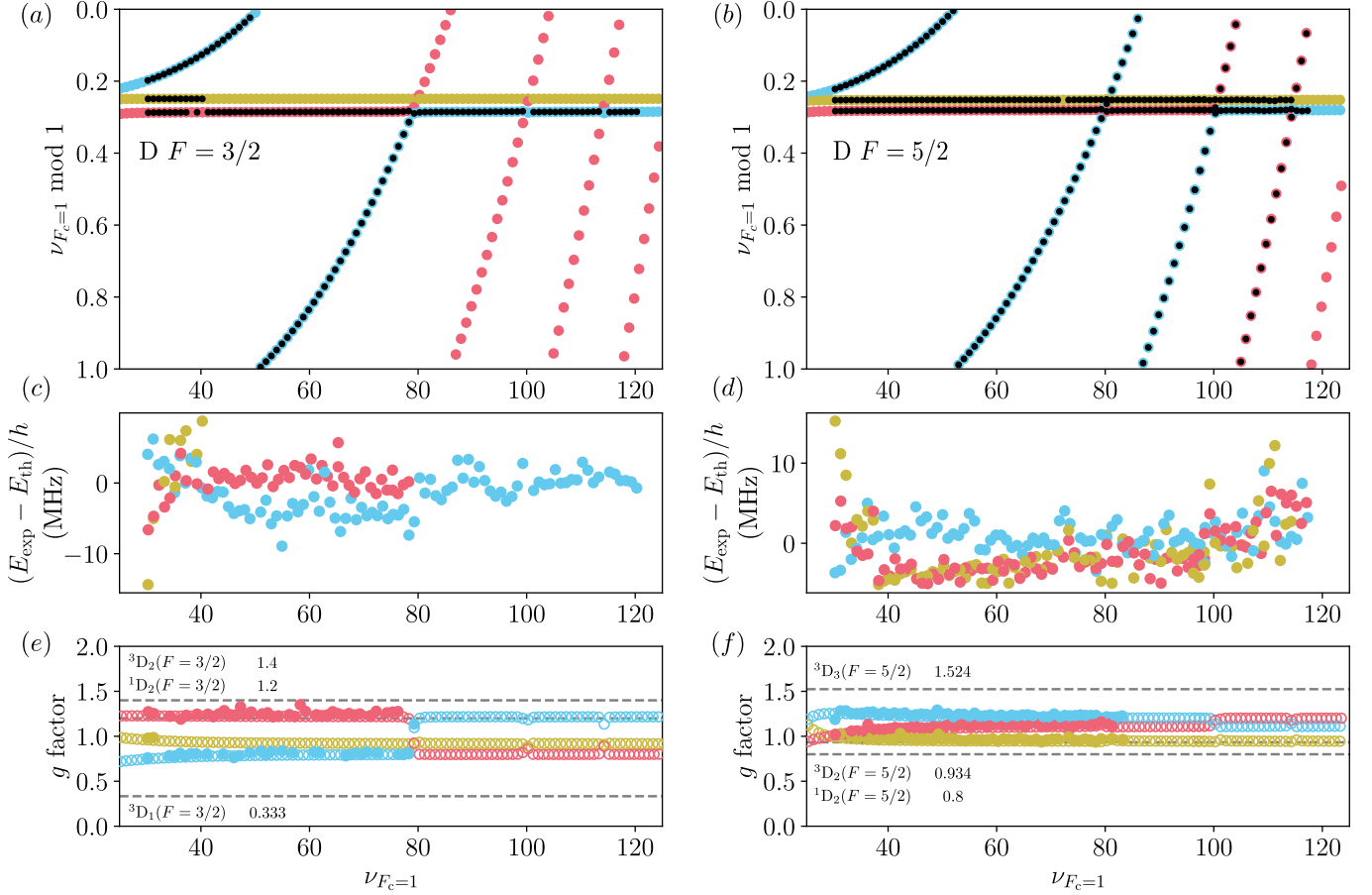


Figure 18. Lu-Fano-type plot of the  $^{171}\text{Yb}$  (a)  $|\nu, L = 2, F = 3/2\rangle$  and (b)  $|\nu, L = 2, F = 5/2\rangle$  Rydberg states. The experimentally observed Rydberg states are indicated by black dots and compared to theoretically obtained energies from the MQDT model (colored dots) presented in Tab. X and Tab. XI. (c) and (d) Deviations between the experimentally observed and theoretically calculated state energies. (e) and (f) Experimentally observed (full circles) and theoretically calculated  $g$ -factors of the  $|\nu, L = 2, F = 3/2\rangle$  and  $|\nu, L = 2, F = 5/2\rangle$  Rydberg states, respectively. Color coding as in (a) and (b). The gray dashed lines indicate the values of Landé  $g$  factors in pure  $LS$  coupling.

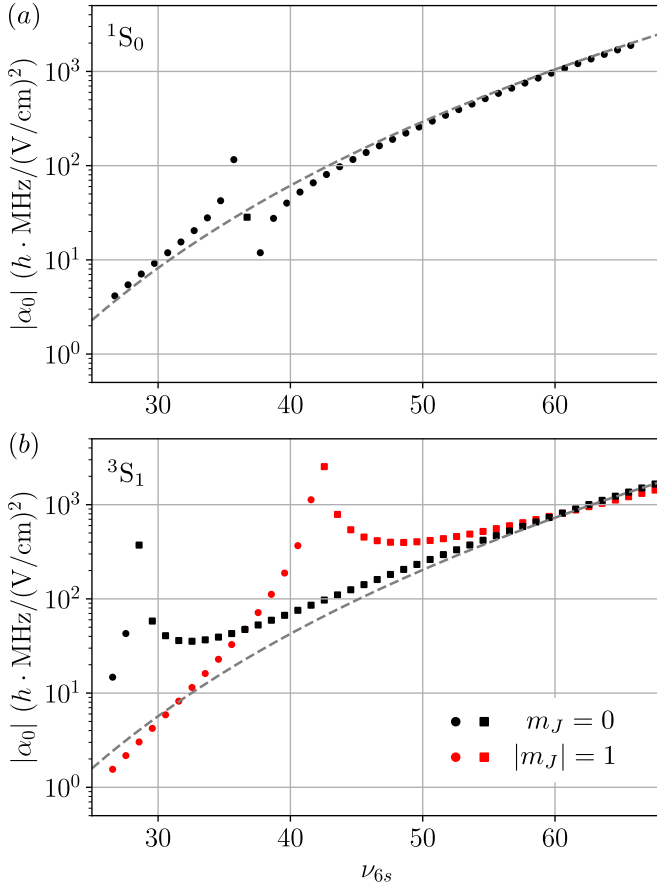


Figure 19. Predicted absolute static dipole polarizabilities of Rydberg series of  $^{174}\text{Yb}$  for (a)  $6sns\ ^1S_0$  and (b)  $6sns\ ^3S_1$ . Circles indicate positive values of  $\alpha_0$ , whereas squares indicate negative values of  $\alpha_0$ . The gray, dashed lines in (a) and (b) serve as a guide to the eye, indicating a  $\nu_{6s}^7$  scaling.

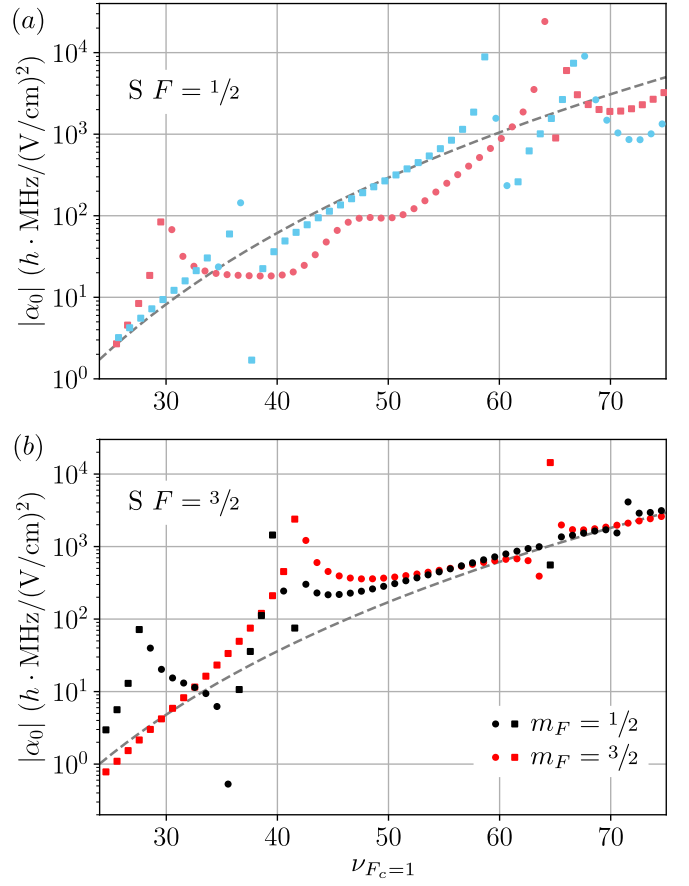


Figure 20. Predicted absolute static dipole polarizabilities of Rydberg series of  $^{171}\text{Yb}$  with (a)  $SF = 1/2$  (color code as in Fig. 3) and (b)  $SF = 3/2$ . Circles indicate positive values of  $\alpha_0$ , whereas squares indicate negative values of  $\alpha_0$ . The gray, dashed lines in (a) and (b) serve as a guide to the eye, indicating a  $\nu_{F_c=1}^7$  scaling.

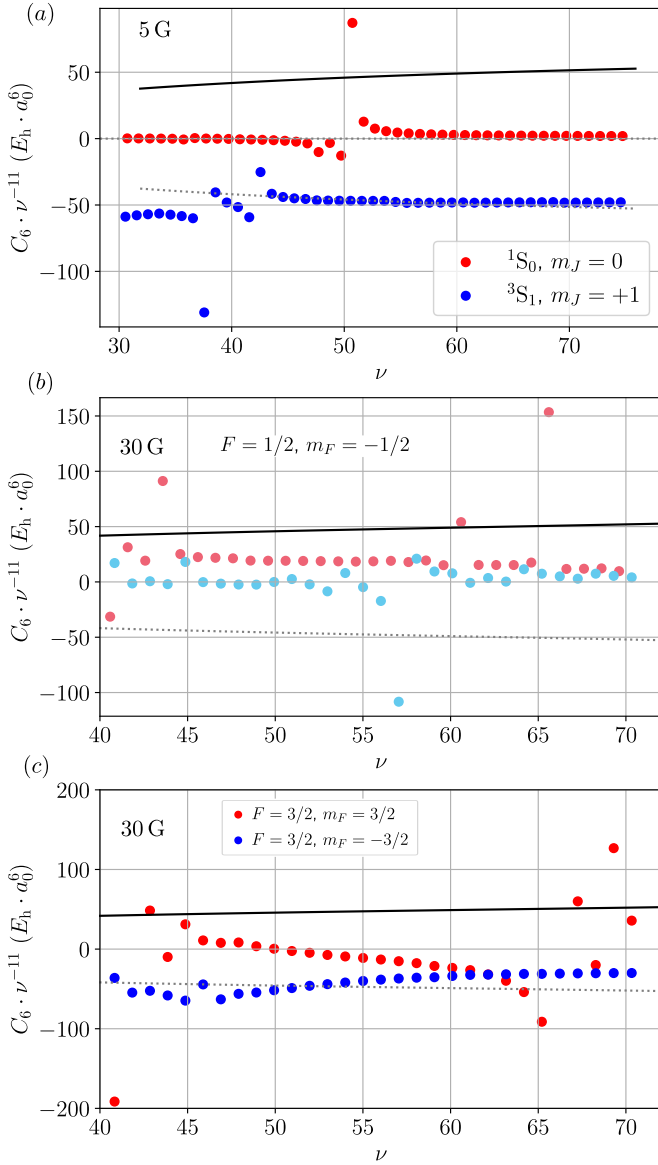


Figure 21. Predicted scaled  $C_6$  coefficients of (a)  $^{174}\text{Yb}$   $^1S_0$  (red dots) and  $^3S_1$  (blue dots) Rydberg states at a magnetic field of 5 G ( $\theta = \pi/2$ ), (b) and (c)  $^{171}\text{Yb}$   $|\nu, L = 0, F = 1/2\rangle$  and  $|\nu, L = 0, F = 3/2\rangle$  Rydberg states at a magnetic field of 30 G ( $\theta = \pi/2$ ). For comparison, the scaled  $C_6$  coefficients of  $n^2S_{1/2}$  Rydberg states of Rb are given by solid ( $C_6$ ) and dotted ( $-C_6$ ) black lines. The color code in (b) corresponds to the color code in Fig. 3.

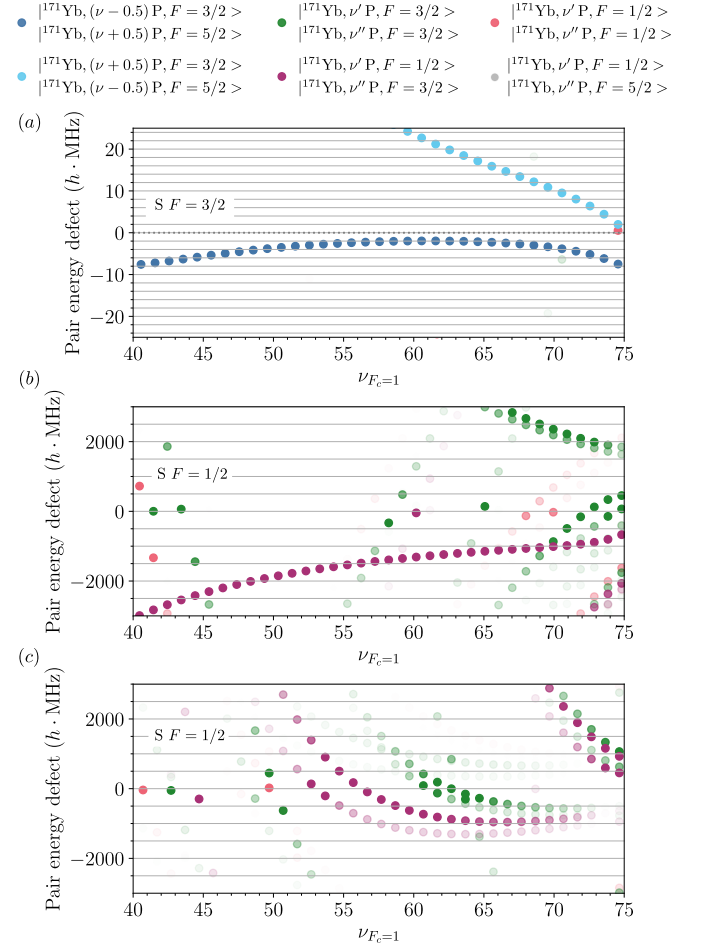


Figure 22.  $^{171}\text{Yb}$  pair energy defects between  $|\nu_{F_c=1}, L = 0, F\rangle |\nu_{F_c=1}, L = 0, F\rangle$  and the nearest dipole coupled  $|\nu_{F_c=1}, L = 1, F\rangle |\nu_{F_c=1}, L = 1, F'\rangle$  states for (a)  $F = 3/2$ , and (b) and (c)  $F = 1/2$ . The color of the markers indicates the combination of hyperfine states of the  $|\nu, L = 1, F\rangle |\nu', L = 1, F'\rangle$  pair state according to the legend. The opacity encodes  $\left(\frac{d_1 d_2}{\Delta E}\right)^2 \left(\frac{1}{\nu_{F_c=1}}\right)^8$ , where  $d_i$  are the dipole matrix elements between the involved Rydberg states and  $\Delta E$  corresponds to the pair defect.

- [1] H. Bernien, S. Schwartz, A. Keesling, H. Levine, A. Omran, H. Pichler, S. Choi, A. S. Zibrov, M. Endres, M. Greiner, V. Vuletić, and M. D. Lukin, Probing many-body dynamics on a 51-atom quantum simulator, *Nature* **551**, 579 (2017).
- [2] P. Scholl, M. Schuler, H. J. Williams, A. A. Eberharter, D. Barredo, K.-N. Schymik, V. Lienhard, L.-P. Henry, T. C. Lang, T. Lahaye, A. M. Läuchli, and A. Browaeys, Quantum simulation of 2D antiferromagnets with hundreds of Rydberg atoms, *Nature* **595**, 233 (2021).
- [3] D. Bluvstein, H. Levine, G. Semeghini, T. T. Wang, S. Ebadi, M. Kalinowski, A. Keesling, N. Maskara, H. Pichler, M. Greiner, V. Vuletić, and M. D. Lukin, A quantum processor based on coherent transport of entangled atom arrays, *Nature* **604**, 451 (2022).
- [4] W. J. Eckner, N. Darkwah Oppong, A. Cao, A. W. Young, W. R. Milner, J. M. Robinson, J. Ye, and A. M. Kaufman, Realizing spin squeezing with Rydberg interactions in an optical clock, *Nature* **621**, 734 (2023).
- [5] P. Goy, J. M. Raimond, G. Vitrant, and S. Haroche, Millimeter-wave spectroscopy in cesium Rydberg states. Quantum defects, fine- and hyperfine-structure measurements, *Phys. Rev. A* **26**, 2733 (1982).
- [6] K.-H. Weber and C. J. Sansonetti, Accurate energies of  $nS$ ,  $nP$ ,  $nD$ ,  $nF$ , and  $nG$  levels of neutral cesium, *Phys. Rev. A* **35**, 4650 (1987).
- [7] W. Li, I. Mourachko, M. W. Noel, and T. F. Gallagher, Millimeter-wave spectroscopy of cold Rb Rydberg atoms in a magneto-optical trap: Quantum defects of the  $ns$ ,  $np$ , and  $nd$  series, *Phys. Rev. A* **67**, 052502 (2003).
- [8] M. Mack, F. Karlewski, H. Hattermann, S. Höckh, F. Jessen, D. Cano, and J. Fortágh, Measurement of absolute transition frequencies of  $^{87}\text{Rb}$  to  $nS$  and  $nD$  Rydberg states by means of electromagnetically induced transparency, *Phys. Rev. A* **83**, 052515 (2011).
- [9] J. Han, Y. Jamil, D. V. L. Norum, P. J. Tanner, and T. F. Gallagher, Rb  $nf$  quantum defects from millimeter-wave spectroscopy of cold  $^{85}\text{Rb}$  Rydberg atoms, *Phys. Rev. A* **74**, 054502 (2006).
- [10] J. Deiglmayr, H. Herburger, H. Saßmannshausen, P. Jansen, H. Schmutz, and F. Merkt, Precision measurement of the ionization energy of Cs I, *Phys. Rev. A* **93**, 013424 (2016).
- [11] M. Peper, F. Helmrich, J. Butscher, J. A. Agner, H. Schmutz, F. Merkt, and J. Deiglmayr, Precision measurement of the ionization energy and quantum defects of  $^{39}\text{K}$  I, *Phys. Rev. A* **100**, 012501 (2019).
- [12] M. L. Zimmerman, M. G. Littman, M. M. Kash, and D. Kleppner, Stark structure of the Rydberg states of alkali-metal atoms, *Phys. Rev. A* **20**, 2251 (1979).
- [13] C. E. Theodosiou, Lifetimes of alkali-metal—atom Rydberg states, *Phys. Rev. A* **30**, 2881 (1984).
- [14] J. Deiglmayr, Long-range interactions between Rydberg atoms, *Phys. Scr.* **91**, 104007 (2016).
- [15] L. Béguin, A. Vernier, R. Chicireanu, T. Lahaye, and A. Browaeys, Direct Measurement of the van der Waals Interaction between Two Rydberg Atoms, *Phys. Rev. Lett.* **110**, 263201 (2013).
- [16] S. Ravets, H. Labuhn, D. Barredo, T. Lahaye, and A. Browaeys, Measurement of the angular dependence of the dipole-dipole interaction between two individual Rydberg atoms at a Förster resonance, *Phys. Rev. A* **92**, 020701 (2015).
- [17] S. Anand, C. E. Bradley, R. White, V. Ramesh, K. Singh, and H. Bernien, A dual-species Rydberg array (2024), arXiv:2401.10325 [quant-ph].
- [18] W. P. Spencer, A. G. Vaidyanathan, D. Kleppner, and T. W. Ducas, Measurements of lifetimes of sodium Rydberg states in a cooled environment, *Phys. Rev. A* **24**, 2513 (1981).
- [19] W. P. Spencer, A. G. Vaidyanathan, D. Kleppner, and T. W. Ducas, Temperature dependence of blackbody-radiation-induced transfer among highly excited states of sodium, *Phys. Rev. A* **25**, 380 (1982).
- [20] H. Bergström, C. Levinson, and H. Lundberg, Natural radiative lifetimes in the  $5snd\ ^1D_2$  series of Sr I, *Z. Phys. D* **2**, 127 (1986).
- [21] C. Boisseau, I. Simbotin, and R. Côté, Macrodimers: Ultralong Range Rydberg Molecules, *Phys. Rev. Lett.* **88**, 133004 (2002).
- [22] K. R. Overstreet, A. Schwettmann, J. Tallant, D. Booth, and J. P. Shaffer, Observation of electric-field-induced Cs Rydberg atom macrodimers, *Nat. Phys.* **5**, 581 (2009).
- [23] H. Saßmannshausen and J. Deiglmayr, Observation of Rydberg-Atom Macrodimers: Micrometer-Sized Diatomic Molecules, *Phys. Rev. Lett.* **117**, 083401 (2016).
- [24] S. Hollerith, J. Zeiher, J. Rui, A. Rubio-Abadal, V. Walther, T. Pohl, D. M. Stamper-Kurn, I. Bloch, and C. Gross, Quantum gas microscopy of Rydberg macrodimers, *Science* **364**, 664 (2019).
- [25] A. Cooper, J. P. Covey, I. S. Madjarov, S. G. Porsev, M. S. Safronova, and M. Endres, Alkaline-Earth Atoms in Optical Tweezers, *Phys. Rev. X* **8**, 041055 (2018).
- [26] M. A. Norcia, A. W. Young, and A. M. Kaufman, Microscopic Control and Detection of Ultracold Strontium in Optical-Tweezer Arrays, *Phys. Rev. X* **8**, 041054 (2018).
- [27] R. C. Teixeira, A. Larrouy, A. Muni, L. Lachaud, J.-M. Raimond, S. Gleyzes, and M. Brune, Preparation of Long-Lived, Non-Autoionizing Circular Rydberg States of Strontium, *Phys. Rev. Lett.* **125**, 263001 (2020).
- [28] C. Hölzl, A. Götzelmann, E. Pultinevicius, M. Wirth, and F. Meinert, Long-Lived Circular Rydberg Qubits of Alkaline-Earth Atoms in Optical Tweezers (2024), arXiv:2401.10625 [physics.atom-ph].
- [29] J. T. Wilson, S. Saskin, Y. Meng, S. Ma, R. Dilip, A. P. Burgers, and J. D. Thompson, Trapping Alkaline Earth Rydberg Atoms Optical Tweezer Arrays, *Phys. Rev. Lett.* **128**, 033201 (2022).
- [30] A. Jenkins, J. W. Lis, A. Senoo, W. F. McGrew, and A. M. Kaufman, Ytterbium Nuclear-Spin Qubits in an Optical Tweezer Array, *Phys. Rev. X* **12**, 021027 (2022).
- [31] S. Ma, A. P. Burgers, G. Liu, J. Wilson, B. Zhang, and J. D. Thompson, Universal Gate Operations on Nuclear Spin Qubits in an Optical Tweezer Array of  $^{171}\text{Yb}$  Atoms, *Phys. Rev. X* **12**, 021028 (2022).
- [32] W. Huie, L. Li, N. Chen, X. Hu, Z. Jia, W. K. C. Sun, and J. P. Covey, Repetitive Readout and Real-Time Control of Nuclear Spin Qubits in  $^{171}\text{Yb}$  Atoms, *PRX Quantum* **4**, 030337 (2023).
- [33] D. K. Mark, J. Choi, A. L. Shaw, M. Endres, and S. Choi, Benchmarking Quantum Simulators Using Er-

- godic Quantum Dynamics, Phys. Rev. Lett. **131**, 110601 (2023).
- [34] P. Scholl, A. L. Shaw, R. B.-S. Tsai, R. Finkelstein, J. Choi, and M. Endres, Erasure conversion in a high-fidelity Rydberg quantum simulator, Nature **622**, 273 (2023).
- [35] R. Finkelstein, R. B.-S. Tsai, X. Sun, P. Scholl, S. Direkci, T. Gefen, J. Choi, A. L. Shaw, and M. Endres, Universal quantum operations and ancilla-based readout for tweezer clocks (2024), arXiv:2402.16220 [quant-ph].
- [36] A. Cao, W. J. Eckner, T. Lukin Yelin, A. W. Young, S. Jandura, L. Yan, K. Kim, G. Pupillo, J. Ye, N. Darkwah Oppong, and A. M. Kaufman, Multi-qubit gates and 'Schrodinger cat' states in an optical clock (2024), arXiv:2402.16289 [quant-ph].
- [37] J. W. Lis, A. Senoo, W. F. McGrew, F. Rönchen, A. Jenkins, and A. M. Kaufman, Midcircuit Operations Using the *omg* Architecture in Neutral Atom Arrays, Phys. Rev. X **13**, 041035 (2023).
- [38] M. A. Norcia, W. B. Cairncross, K. Barnes, P. Battaglini, A. Brown, M. O. Brown, K. Cassella, C.-A. Chen, R. Coxe, D. Crow, J. Epstein, C. Griger, A. M. W. Jones, H. Kim, J. M. Kindem, J. King, S. S. Kondov, K. Kotru, J. Lauigan, M. Li, M. Lu, E. Megidish, J. Marjanovic, M. McDonald, T. Mitiga, J. A. Muniz, S. Narayanaswami, C. Nishiguchi, R. Notermans, T. Paule, K. A. Pawlak, L. S. Peng, A. Ryou, A. Smull, D. Stack, M. Stone, A. Sucich, M. Urbanek, R. J. M. van de Veerdonk, Z. Vendeiro, T. Wilkason, T.-Y. Wu, X. Xie, X. Zhang, and B. J. Bloom, Midcircuit Qubit Measurement and Rearrangement in a  $^{171}\text{Yb}$  Atomic Array, Phys. Rev. X **13**, 041034 (2023).
- [39] Y. Wu, S. Kolkowitz, S. Puri, and J. D. Thompson, Erasure conversion for fault-tolerant quantum computing in alkaline earth Rydberg atom arrays, Nat. Commun. **13**, 4657 (2022).
- [40] S. Ma, G. Liu, P. Peng, B. Zhang, S. Jandura, J. Claes, A. P. Burgers, G. Pupillo, S. Puri, and J. D. Thompson, High-fidelity gates and mid-circuit erasure conversion in an atomic qubit, Nature **622**, 279 (2023).
- [41] M. J. Seaton, Quantum defect theory I. General formulation, Proc. Phys. Soc. (London) **88**, 801 (1966).
- [42] U. Fano, Quantum Defect Theory of  $l$  Uncoupling in  $\text{H}_2$  as an Example of Channel-Interaction Treatment, Phys. Rev. A **2**, 353 (1970).
- [43] C. L. Vaillant, M. P. A. Jones, and R. M. Potvliege, Multichannel quantum defect theory of strontium bound Rydberg states, J. Phys. B: At., Mol. Opt. Phys. **47**, 155001 (2014).
- [44] F. Robicheaux, D. W. Booth, and M. Saffman, Theory of long-range interactions for Rydberg states attached to hyperfine-split cores, Phys. Rev. A **97**, 022508 (2018).
- [45] E. Robertson, N. Šibalić, R. Potvliege, and M. Jones, ARC 3.0: An expanded Python toolbox for atomic physics calculations, Comput. Phys. Commun. **261**, 107814 (2021).
- [46] M. Aymar, A. Débarre, and O. Robaux, Highly excited levels of neutral ytterbium. II. Multichannel quantum defect analysis of odd- and even-parity spectra, J. Phys. B: At. Mol. Phys. **13**, 1089 (1980).
- [47] M. Aymar, Multichannel-quantum-defect theory wave functions of Ba tested or improved by laser measurements, J. Opt. Soc. Am. B **1**, 239 (1984).
- [48] R. Ali, M. Yaseen, A. Nadeem, S. A. Bhatti, and M. A. Baig, Two-colour three-photon excitation of the  $6snf\ ^{1,3}\text{F}_3$  and  $6snp\ ^1\text{P}_1, ^3\text{P}_{1,2}$  Rydberg levels of Yb I, J. Phys. B: At., Mol. Opt. Phys. **32**, 953 (1999).
- [49] H. Lehec, A. Zuliani, W. Maineult, E. Luc-Koenig, P. Pillet, P. Cheinet, F. Niyaz, and T. F. Gallagher, Laser and microwave spectroscopy of even-parity Rydberg states of neutral ytterbium and multichannel-quantum-defect-theory analysis, Phys. Rev. A **98**, 062506 (2018).
- [50] H. Lehec, *Spectroscopie Rydberg et excitation du coeur isolé d'atomes d'ytterbium ultra-froids*, Ph.D. thesis, Université Paris Saclay (COMUE) (2017).
- [51] R. Ding, J. D. Whalen, S. K. Kanungo, T. C. Killian, F. B. Dunning, S. Yoshida, and J. Burgdörfer, Spectroscopy of  $^{87}\text{Sr}$  triplet Rydberg states, Phys. Rev. A **98**, 042505 (2018).
- [52] F. Robicheaux, Calculations of long range interactions for  $^{87}\text{Sr}$  Rydberg states, J. Phys. B: At., Mol. Opt. Phys. **52**, 244001 (2019).
- [53] P. Camus and F. S. Tomkins, Spectre d'absorption de Yb I, J. Physique **30**, 545 (1969).
- [54] W. F. Meggers and J. L. Tech, The First Spectrum of Ytterbium (Yb I), J. Res. NBS **83**, 13 (1977).
- [55] P. Camus, A. Débarre, and C. Morillon, Highly excited levels of neutral ytterbium. I. Two-photon and two-step spectroscopy of even spectra, J. Phys. B: At. Mol. Phys. **13**, 1073 (1980).
- [56] M. Aymar, R. J. Champeau, C. Delsart, and O. Robaux, Three-step laser spectroscopy and multichannel quantum defect analysis of odd-parity Rydberg states of neutral ytterbium, J. Phys. B: At. Mol. Phys. **17**, 3645 (1984).
- [57] J. Neukammer, H. Rinneberg, and U. Majewski, Diamagnetic shift and singlet-triplet mixing of  $6snp$  Yb Rydberg states with large radial extent, Phys. Rev. A **30**, 1142 (1984).
- [58] H. Maeda, Y. Matsuo, M. Takami, and A. Suzuki, Optical-microwave double-resonance spectroscopy of highly excited Rydberg states of ytterbium, Phys. Rev. A **45**, 1732 (1992).
- [59] R. Zerneck, L. Caiyan, J. Zhankui, and J. Larsson, Landé  $g_J$  factor measurements in the  $6snd\ ^{1,3}\text{D}_2$  sequences of Yb I, Z. Phys. D **37**, 259 (1996).
- [60] F. Niyaz, J. Nunkaew, and T. F. Gallagher, Microwave spectroscopy of the Yb  $6s(n+3)d \rightarrow 6sng, 6snh,$  and  $6sni$  transitions, Phys. Rev. A **99**, 042507 (2019).
- [61] D. Okuno, Y. Nakamura, T. Kusano, Y. Takasu, N. Takei, H. Konishi, and Y. Takahashi, High-resolution Spectroscopy and Single-photon Rydberg Excitation of Reconfigurable Ytterbium Atom Tweezer Arrays Utilizing a Metastable State, J. Phys. Soc. Japan **91**, 084301 (2022).
- [62] K. T. Lu, Spectroscopy and Collision Theory. The Xe Absorption Spectrum, Phys. Rev. A **4**, 579 (1971).
- [63] K. Barnes, P. Battaglini, B. J. Bloom, K. Cassella, R. Coxe, N. Crisosto, J. P. King, S. S. Kondov, K. Kotru, S. C. Larsen, J. Lauigan, B. J. Lester, M. McDonald, E. Megidish, S. Narayanaswami, C. Nishiguchi, R. Notermans, L. S. Peng, A. Ryou, T.-Y. Wu, and M. Yarwood, Assembly and coherent control of a register of nuclear spin qubits, Nat. Commun. **13**, 2779 (2022).

- [64] J. Hostetter, J. D. Pritchard, J. E. Lawler, and M. Saffman, Measurement of holmium Rydberg series through magneto-optical trap depletion spectroscopy, *Phys. Rev. A* **91**, 012507 (2015).
- [65] A. Trautmann, M. J. Mark, P. Ilzhöfer, H. Edri, A. E. Arrach, J. G. Maloberti, C. H. Greene, F. Robicheaux, and F. Ferlaino, Spectroscopy of Rydberg states in erbium using electromagnetically induced transparency, *Phys. Rev. Res.* **3**, 033165 (2021).
- [66] M. J. Seaton, Quantum defect theory, *Rep. Prog. Phys.* **46**, 167 (1983).
- [67] W. E. Cooke and C. L. Cromer, Multichannel quantum-defect theory and an equivalent N-level system, *Phys. Rev. A* **32**, 2725 (1985).
- [68] C.-M. Lee and K. T. Lu, Spectroscopy and Collision Theory. II. the Ar Absorption Spectrum, *Phys. Rev. A* **8**, 1241 (1973).
- [69] M. Aymar, O. Robaux, and C. Thomas, Theoretical investigations on the bound odd-parity spectrum of neutral krypton, *J. Phys. B: At. Mol. Phys.* **14**, 4255 (1981).
- [70] H. J. Wörner, U. Hollenstein, and F. Merkt, Multichannel quantum defect theory and high-resolution spectroscopy of the hyperfine structure of high Rydberg states of  $^{83}\text{Kr}$ , *Phys. Rev. A* **68**, 032510 (2003).
- [71] M. Schäfer, M. Raunhardt, and F. Merkt, Millimeter-wave spectroscopy and multichannel quantum-defect-theory analysis of high Rydberg states of xenon: The hyperfine structure of  $^{129}\text{Xe}^+$  and  $^{131}\text{Xe}^+$ , *Phys. Rev. A* **81**, 032514 (2010).
- [72] R. Beigang, K. Lücke, D. Schmidt, A. Timmermann, and P. West, One-photon laser spectroscopy of Rydberg series from metastable levels in calcium and strontium, *Phys. Scr.* **26**, 183 (1982).
- [73] J. Neukammer and H. Rinneberg, Hyperfine structure of perturbed  $6sns\ ^3S_1$  Rydberg states of barium, *J. Phys. B: At. Mol. Phys.* **15**, L425 (1982).
- [74] H. Rinneberg and J. Neukammer, Hyperfine structure and three-channel quantum-defect theory of  $6snd\ ^1D_2$  Rydberg states of Ba, *Phys. Rev. A* **27**, 1779 (1983).
- [75] M. Aymar, Rydberg series of alkaline-earth atoms Ca through Ba. the interplay of laser spectroscopy and multichannel quantum defect analysis, *Phys. Rep.* **110**, 163 (1984).
- [76] S. Bhattacharyya, M. A. N. Razvi, S. Cohen, and S. G. Nakhate, Odd-parity  $J = 11/2$  autoionizing Rydberg series of europium below the  $5d\ ^9D_4$  threshold: Spectroscopy and multichannel quantum-defect-theory analysis, *Phys. Rev. A* **76**, 012502 (2007).
- [77] A. Osterwalder, A. Wüest, F. Merkt, and C. Jungen, High-resolution millimeter wave spectroscopy and multichannel quantum defect theory of the hyperfine structure in high Rydberg states of molecular hydrogen  $\text{H}_2$ , *J. Chem. Phys.* **121**, 11810 (2004).
- [78] D. Sprecher, C. Jungen, and F. Merkt, Determination of the binding energies of the  $np$  Rydberg states of  $\text{H}_2$ , HD, and  $\text{D}_2$  from high-resolution spectroscopic data by multichannel quantum-defect theory, *J. Chem. Phys.* **140**, 104303 (2014).
- [79] T. F. Gallagher, *Rydberg Atoms*, Cambridge Monographs on Atomic, Molecular and Chemical Physics (Cambridge University Press, 1994).
- [80] R. Beigang, W. Makat, A. Timmermann, and P. J. West, Hyperfine-Induced  $n$  Mixing in High Rydberg States of  $^{87}\text{Sr}$ , *Phys. Rev. Lett.* **51**, 771 (1983).
- [81] J.-Q. Sun and K. T. Lu, Hyperfine structure of extremely high Rydberg  $msns\ ^1S_0$  and  $msns\ ^3S_1$  series in odd alkaline-earth isotopes, *J. Phys. B: At., Mol. Opt. Phys.* **21**, 1957 (1988).
- [82] M. Saffman, Quantum computing with atomic qubits and Rydberg interactions: progress and challenges, *J. Phys. B: At., Mol. Opt. Phys.* **49**, 202001 (2016).
- [83] R. Blatt, H. Schnatz, and G. Werth, Precise Determination of the  $^{171}\text{Yb}^+$  Ground State Hyperfine Separation, *Z. Phys. A - Atoms and Nuclei* **312**, 143 (1983).
- [84] P. Liao, R. Freeman, R. Panock, and L. Humphrey, Hyperfine-induced singlet-triplet mixing in  $^3\text{He}$ , *Opt. Commun.* **34**, 195 (1980).
- [85] J.-Q. Sun, Multichannel quantum defect theory of the hyperfine structure of high Rydberg states, *Phys. Rev. A* **40**, 7355 (1989).
- [86] J.-Q. Sun, K. T. Lu, and R. Beigang, Hyperfine structure of extremely high Rydberg  $msnd\ ^1D_2$ ,  $^3D_1$ ,  $^3D_2$  and  $^3D_3$  series in odd alkaline-earth isotopes, *J. Phys. B: At., Mol. Opt. Phys.* **22**, 2887 (1989).
- [87] L. Barbier and R.-J. Champeau, Very high resolution study of high Rydberg levels of the configurations  $4f^{14}6snd$  of Yb I, *J. Physique* **41**, 947 (1980).
- [88] U. Majewski, J. Neukammer, and H. Rinneberg, High-Resolution Three-Photon Spectroscopy of  $6s15p\ ^{1,3}P_1$  Rydberg States of Yb, *Phys. Rev. Lett.* **51**, 1340 (1983).
- [89] U. Majewski, *"Hochauflösende Laserspektroskopie von Ytterbium-Rydbergzuständen"*, Diploma thesis, Freie Universität Berlin (1985).
- [90] S. Weber, C. Tresp, H. Menke, A. Urvoy, O. Firstenberg, H. P. Büchler, and S. Hofferberth, Calculation of Rydberg interaction potentials, *J. Phys. B: At., Mol. Opt. Phys.* **50**, 133001 (2017).
- [91] N. Šibalić, J. Pritchard, C. Adams, and K. Weatherill, ARC: An open-source library for calculating properties of alkali Rydberg atoms, *Comput. Phys. Commun.* **220**, 319 (2017).
- [92] B. Vermersch, Anisotropy and state mixing in the interactions between Rydberg states, *Eur. Phys. J.: Spec. Top.* **225**, 2977 (2016).
- [93] C. L. Vaillant, M. P. A. Jones, and R. M. Potvliege, Long-range Rydberg–Rydberg interactions in calcium, strontium and ytterbium, *J. Phys. B: At., Mol. Opt. Phys.* **45**, 135004 (2012).
- [94] I. I. Beterov and M. Saffman, Rydberg blockade, Förster resonances, and quantum state measurements with different atomic species, *Phys. Rev. A* **92**, 042710 (2015).
- [95] J. T. Young, P. Bienias, R. Belyansky, A. M. Kaufman, and A. V. Gorshkov, Asymmetric Blockade and Multi-qubit Gates via Dipole-Dipole Interactions, *Phys. Rev. Lett.* **127**, 120501 (2021).
- [96] A. Derevianko, P. Kómár, T. Topcu, R. M. Kroeze, and M. D. Lukin, Effects of molecular resonances on Rydberg blockade, *Phys. Rev. A* **92**, 063419 (2015).
- [97] H. Levine, A. Keesling, G. Semeghini, A. Omran, T. T. Wang, S. Ebadi, H. Bernien, M. Greiner, V. Vuletić, H. Pichler, and M. D. Lukin, Parallel Implementation of High-Fidelity Multiqubit Gates with Neutral Atoms, *Phys. Rev. Lett.* **123**, 170503 (2019).
- [98] S. Jandura and G. Pupillo, Time-Optimal Two- and Three-Qubit Gates for Rydberg Atoms, *Quantum* **6**, 712 (2022).
- [99] S. J. Evered, D. Bluvstein, M. Kalinowski, S. Ebadi, T. Manovitz, H. Zhou, S. H. Li, A. A. Geim,

- T. T. Wang, N. Maskara, H. Levine, G. Semeghini, G. Greiner, G. Vuletić, and M. D. Lukin, High-fidelity parallel entangling gates on a neutral atom quantum computer, *Nature* **622**, 268 (2023).
- [100] G. Lochead, D. Boddy, D. P. Sadler, C. S. Adams, and M. P. A. Jones, Number-resolved imaging of excited-state atoms using a scanning autoionization microscope, *Phys. Rev. A* **87**, 053409 (2013).
- [101] I. S. Madjarov, J. P. Covey, A. L. Shaw, J. Choi, A. Kale, A. Cooper, H. Pichler, V. Schkolnik, J. R. Williams, and M. Endres, High-fidelity entanglement and detection of alkaline-earth Rydberg atoms, *Nat. Phys* **16**, 857 (2020).
- [102] A. P. Burgers, S. Ma, S. Saskin, J. Wilson, M. A. Alarcón, C. H. Greene, and J. D. Thompson, Controlling Rydberg Excitations Using Ion-Core Transitions in Alkaline-Earth Atom-Tweezer Arrays, *PRX Quantum* **3**, 020326 (2022).
- [103] K.-L. Pham, T. F. Gallagher, P. Pillet, S. Lepoutre, and P. Cheinet, Coherent Light Shift on Alkaline-Earth Rydberg Atoms from Isolated Core Excitation without Autoionization, *PRX Quantum* **3**, 020327 (2022).
- [104] A. D. Ludlow, M. M. Boyd, J. Ye, E. Peik, and P. O. Schmidt, Optical atomic clocks, *Rev. Mod. Phys.* **87**, 637 (2015).
- [105] V. D. Ovsiannikov, A. Derevianko, and K. Gibble, Rydberg Spectroscopy in an Optical Lattice: Blackbody Thermometry for Atomic Clocks, *Phys. Rev. Lett.* **107**, 093003 (2011).
- [106] M. Aymar, C. H. Greene, and E. Luc-Koenig, Multi-channel Rydberg spectroscopy of complex atoms, *Rev. Mod. Phys.* **68**, 1015 (1996).
- [107] C. H. Greene and M. Aymar, Spin-orbit effects in the heavy alkaline-earth atoms, *Phys. Rev. A* **44**, 1773 (1991).
- [108] A. R. Edmonds, *Angular momentum in quantum mechanics*, 4th ed. (Princeton University Press, Princeton, 1996).
- [109] O. Robaux and M. Aymar, A program for analysing the Rydberg series of highly excited discrete spectra by M.Q.D.T., *Comput. Phys. Commun.* **25**, 223 (1982).
- [110] F. A. Jenkins and E. Segrè, The Quadratic Zeeman Effect, *Phys. Rev.* **55**, 52 (1939).
- [111] M. Kleinert, M. E. Gold Dahl, and S. Bergeson, Measurement of the Yb I  $^1S_0 - ^1P_1$  transition frequency at 399 nm using an optical frequency comb, *Phys. Rev. A* **94**, 052511 (2016).
- [112] I. I. Beterov, I. I. Ryabtsev, D. B. Tretyakov, and V. M. Entin, Quasiclassical calculations of blackbody-radiation-induced depopulation rates and effective lifetimes of Rydberg  $ns$ ,  $np$ , and  $nd$  alkali-metal atoms with  $n \leq 80$ , *Phys. Rev. A* **79**, 052504 (2009).
- [113] J. T. Wilson, *New tools for quantum science in Yb Rydberg atom arrays*, Ph.D. thesis, Princeton University (2022).
- [114] W. C. Martin, R. Zalubas, and L. Hagan, Atomic Energy Levels: The Rare Earth Elements, *Nat. Stand. Ref. Data Ser., NSRDS-NBS* **60**, 10.6028/NBS.NSRDS.60 (1978).
- [115] W. Bi-ru, Z. You-feng, X. Yun-fei, P. Li-gang, L. Ji, and Z. Jian-wei, The  $6snp \ ^3P_{0,2}$  Rydberg series of neutral ytterbium, *J. Phys. B: At., Mol. Opt. Phys.* **24**, 49 (1991).
- [116] J.-F. Wyart and P. Camus, Extended Analysis of the Emission Spectrum of Neutral Ytterbium (Yb I), *Phys. Scr.* **20**, 43 (1979).

## Appendix H: MQDT model parameters

### 1. $^{174}\text{Yb}$

Table II. Six-channel MQDT model parameters for the  $6sns\ ^1S_0$  series of  $^{174}\text{Yb}$  obtained from fit to spectroscopic data presented in Tabs. XII to XIX. The electronic configuration of the perturbing Rydberg channels  $4f^{13}5d6snp$  is abbreviated as  $5d$ . The rotations  $\mathcal{R}(\theta_{ij})$  are applied in the order  $\mathcal{R}(\theta_{12})\mathcal{R}(\theta_{13})\mathcal{R}(\theta_{14})\mathcal{R}(\theta_{34})\mathcal{R}(\theta_{35})\mathcal{R}(\theta_{16})$ .

$i, \bar{\alpha}, \alpha$	1	2	3	4	5	6
$ i\rangle$	$(6s_{1/2})(ns_{1/2})$	$5d\ \mathbf{a}$	$(6p_{3/2})(np_{3/2})$	$5d\ \mathbf{b}$	$(6p_{1/2})(np_{1/2})$	$5d\ \mathbf{c}$
$I_i\ (\text{cm}^{-1})$	50 443.070393	83 967.7	80 835.39	83 967.7	77 504.98	83 967.7
$ \bar{\alpha}\rangle$	$6sns\ ^1S_0$	$5d\ \mathbf{a}$	$6pnd\ ^1S_0$	$5d\ \mathbf{b}$	$6pnd\ ^3P_0$	$5d\ \mathbf{c}$
$\mu_\alpha^{(0)}$	0.355097325	0.204537279	0.116394359	0.295432196	0.25765161	0.155807042
$\mu_\alpha^{(2)}$	0.278368431	0.0	0.0	0.0	0.0	0.0
$V_{\bar{\alpha}\alpha}$	$\theta_{12} = 0.12654859$	$\theta_{13} = 0.30010744$	$\theta_{14} = 0.05703381$	$\theta_{34} = 0.11439805$	$\theta_{35} = 0.09864375$	$\theta_{16} = 0.14248210$
$U_{i\bar{\alpha}}$	1	0	0	0	0	0
	0	1	0	0	0	0
	0	0	$-\sqrt{2/3}$	0	$\sqrt{1/3}$	0
	0	0	0	1	0	0
	0	0	$\sqrt{1/3}$	0	$\sqrt{2/3}$	0
	0	0	0	0	0	1

Table III. Five-channel MQDT model parameters for the  $6snd\ ^{1,3}D_2$  series of  $^{174}\text{Yb}$  obtained from a global fit to spectroscopic data presented in Tabs. XII to XIX. The electronic configuration of the perturbing Rydberg channels  $4f^{13}5d6snp$  is abbreviated as  $5d$ . The rotations  $\mathcal{R}(\theta_{ij})$  are applied in the order  $\mathcal{R}(\theta_{12}(\epsilon))\mathcal{R}(\theta_{13})\mathcal{R}(\theta_{14})\mathcal{R}(\theta_{24})\mathcal{R}(\theta_{15})\mathcal{R}(\theta_{25})$ . The channel- $g$ -factors  $g^*$  are obtained in  $LS$  coupling for channels 1 and 2, and by a fit to experimentally observed  $g$  factors [59] for the remaining channels.

$i, \bar{\alpha}, \alpha$	1	2	3	4	5
$ i\rangle$	$(6s_{1/2})(nd_{5/2})$	$(6s_{1/2})(nd_{3/2})$	$5d\ \mathbf{a}$	$5d\ \mathbf{b}$	$(6p_{1/2})(np_{1/2})$
$I_i\ (\text{cm}^{-1})$	50 443.070393	50 443.070393	83 967.7	83 967.7	79 725.35
$ \bar{\alpha}\rangle$	$6snd\ ^1D_2$	$6snd\ ^3D_2$	$5d\ \mathbf{a}$	$5d\ \mathbf{b}$	$6pnd\ ^1D_2$
$\mu_\alpha^{(0)}$	0.729500971	0.75229161	0.196120406	0.233821165	0.152890218
$\mu_\alpha^{(2)}$	-0.0284447537	0.0967044398	0.0	0.0	0.0
$V_{\bar{\alpha}\alpha}$	$\theta_{12}^{(0)} = 0.21157531$ $\theta_{12}^{(2)} = -15.3844$	$\theta_{13} = 0.00522534111$ $\theta_{25} = 0.0721775002$	$\theta_{14} = 0.0398754262$	$\theta_{24} = -0.00720265975$	$\theta_{15} = 0.104784389$
$g^*$	1	1.1670	1.1846	0.9390	1.2376
$U_{i\bar{\alpha}}$	$\sqrt{3/5}$	$\sqrt{2/5}$	0	0	0
	$-\sqrt{2/5}$	$\sqrt{3/5}$	0	0	0
	0	0	1	0	0
	0	0	0	1	0
	0	0	0	0	1



Table IV. Six-channel MQDT model parameters for the  $6snp^{1,3}P_1$  series of  $^{174}\text{Yb}$  obtained from fit to spectroscopic data presented in Tabs. XII to XIX. The electronic configuration of the perturbing Rydberg channels  $4f^{13}5d6snd$  is abbreviated as  $5d$ . The rotations  $\mathcal{R}(\theta_{ij})$  are applied in the order  $\mathcal{R}(\theta_{12}(\epsilon))\mathcal{R}(\theta_{13})\mathcal{R}(\theta_{14})\mathcal{R}(\theta_{15})\mathcal{R}(\theta_{16})\mathcal{R}(\theta_{23})\mathcal{R}(\theta_{24})\mathcal{R}(\theta_{25})\mathcal{R}(\theta_{26})$ .

$i, \bar{\alpha}, \alpha$	1	2	3	4	5	6
$ i\rangle$	$(6s_{1/2})(np_{3/2})$	$(6s_{1/2})(np_{1/2})$	$5d \mathbf{a}$	$5d \mathbf{b}$	$5d \mathbf{c}$	$5d \mathbf{d}$
$I_i$ ( $\text{cm}^{-1}$ )	50 443.070393	50 443.070393	83 967.7	83 967.7	83 967.7	83 967.7
$ \bar{\alpha}\rangle$	$6snp^1P_1$	$6snp^3P_1$	$5d \mathbf{a}$	$5d \mathbf{b}$	$5d \mathbf{c}$	$5d \mathbf{d}$
$\mu_\alpha^{(0)}$	0.92271098	0.98208719	0.22851720	0.20607759	0.19352751	0.18153094
$\mu_\alpha^{(2)}$	2.6036257	-5.4562725	0.0	0.0	0.0	0.0
$V_{\bar{\alpha}\alpha}$	$\theta_{12}^{(0)} = -0.08410871$ $\theta_{16} = -0.10451698$	$\theta_{12}^{(2)} = 120.37555$ $\theta_{23} = 0.02477048$	$\theta_{12}^{(4)} = -9314.23$ $\theta_{24} = 0.05765807$	$\theta_{13} = -0.07318156$ $\theta_{25} = 0.08606276$	$\theta_{14} = -0.06651977$ $\theta_{26} = 0.04994363$	$\theta_{15} = -0.02210989$
$U_{i\bar{\alpha}}$	$\sqrt{2/3}$ $-\sqrt{1/3}$ 0 0 0 0	$\sqrt{1/3}$ $\sqrt{2/3}$ 0 0 0 0	0 0 1 0 0 0	0 0 0 1 0 0	0 0 0 0 1 0	0 0 0 0 0 1

Table V. Four-channel MQDT model parameters for the  $6snp^3P_2$  series of  $^{174}\text{Yb}$  obtained from fit to spectroscopic data presented in Tabs. XX and XXI. The electronic configuration of the perturbing Rydberg channels  $4f^{13}5d6snd$  is abbreviated as  $5d$ . The rotations  $\mathcal{R}(\theta_{ij})$  are applied in the order  $\mathcal{R}(\theta_{12})\mathcal{R}(\theta_{13})\mathcal{R}(\theta_{14})$

$i, \bar{\alpha}, \alpha$	1	2	3	4
$ i\rangle$	$(6s_{1/2})(np_{3/2})$	$5d \mathbf{a}$	$5d \mathbf{b}$	$5d \mathbf{c}$
$I_i$ ( $\text{cm}^{-1}$ )	50 443.070393	83 967.7	83 967.7	83 967.7
$ \bar{\alpha}\rangle$	$6snp^3P_2$	$5d \mathbf{a}$	$5d \mathbf{b}$	$5d \mathbf{c}$
$\mu_\alpha^{(0)}$	0.925121305	0.230133261	0.209638118	0.186228192
$\mu_\alpha^{(2)}$	-2.73247165	0.0	0.0	0.0
$\mu_\alpha^{(4)}$	74.664989	0.0	0.0	0.0
$V_{\bar{\alpha}\alpha}$	$\theta_{12} = 0.0706666127$	$\theta_{13} = 0.0232711158$	$\theta_{14} = -0.0292153659$	
$U_{i\bar{\alpha}}$	1 0 0 0	0 1 0 0	0 0 1 0	0 0 0 1

Table VI. Two-channel MQDT model parameters for the  $6snp^3P_0$  series of  $^{174}\text{Yb}$  obtained from fit to spectroscopic data presented in Tabs. XXII and XXIII. For lack of information, we use a presumed ionization limit of perturbing channel  $Q$  as  $83\,967.7 \text{ cm}^{-1}$ .

$i, \bar{\alpha}, \alpha$	1	2
$ i\rangle$	$(6s_{1/2})(np_{1/2})$	$4f^{13}5d6snd$
$I_i$ ( $\text{cm}^{-1}$ )	50 443.070393	83 967.7
$ \bar{\alpha}\rangle$	$6snp^3P_0$	$Q$
$\mu_\alpha^{(0)}$	0.95356884	0.19845903
$\mu_\alpha^{(2)}$	-0.28602498	0.0
$V_{\bar{\alpha}\alpha}$	$\theta_{12} = 0.16328854$	
$U_{i\bar{\alpha}}$	1 0	0 1

**2.  $^{171}\text{Yb}$**

Table VII. Seven-channel MQDT model parameters for the  $|\nu, L = 0, F = 1/2\rangle$  series of  $^{171}\text{Yb}$  obtained from fit to spectroscopic data presented in Tab. XXIV. The electronic configuration of the perturbing Rydberg channels  $4f^3 5d6snp$  is abbreviated as  $5d$ . The rotations  $\mathcal{R}(\theta_{ij})$  are applied in the order  $\mathcal{R}(\theta_{12})\mathcal{R}(\theta_{13})\mathcal{R}(\theta_{14})\mathcal{R}(\theta_{34})\mathcal{R}(\theta_{35})\mathcal{R}(\theta_{16})$ .

$i, \bar{\alpha}, \alpha$	1 ( $F_c = 0$ )	2	3	4	5	6	7 ( $F_c = 1$ )
$ i_F\rangle$	$(6s_{1/2})(ns_{1/2})$	$5d \mathbf{a}$	$(6p_{3/2})(np_{3/2})$	$5d \mathbf{b}$	$(6p_{1/2})(np_{1/2})$	$5d \mathbf{c}$	$(6s_{1/2})(ns_{1/2})$
$I_i$ ( $\text{cm}^{-1}$ )	50442.795744	83967.7	80835.39	83967.7	77504.98	83967.7	50443.217463
$ \bar{\alpha}\rangle$	$6sns^1S_0$	$5d \mathbf{a}$	$6pnd^1S_0$	$5d \mathbf{b}$	$6pnd^3P_0$	$5d \mathbf{c}$	$6sns^3S_1$
$\mu_{\alpha}^{(0)}$	0.357519763	0.203907536	0.116803536	0.286731074	0.248113946	0.148678953	$\mu_{3S_1}^{3S_1}$
$\mu_{\alpha}^{(2)}$	0.298712849	0.0	0.0	0.0	0.0	0.0	
$\mu_{3S_1}^{3S_1}$	$\mu_{3S_1}^{(0)} = 0.438426851$	$\mu_{3S_1}^{(2)} = 3.91762642$	$\mu_{3S_1}^{(4)} = -10612.6828$	$\mu_{3S_1}^{(6)} = 8017432.38$	$\mu_{3S_1}^{(8)} = -2582622910.0$		
$V_{\bar{\alpha}\alpha}$	$\theta_{12} = 0.131810463$	$\theta_{13} = 0.297612147$	$\theta_{14} = 0.055508821$	$\theta_{34} = 0.101030515$	$\theta_{35} = 0.102911159$	$\theta_{16} = 0.137723736$	
$U_{i\bar{\alpha}}$	$1/2$	0	0	0	0	0	$\sqrt{3}/2$
	0	1	0	0	0	0	0
	0	0	$-\sqrt{2}/3$	0	$\sqrt{1/3}$	0	0
	0	0	0	1	0	0	0
	0	0	$\sqrt{1/3}$	0	$\sqrt{2/3}$	0	0
	0	0	0	0	0	1	0
	$\sqrt{3}/2$	0	0	0	0	0	$-1/2$





Table X. Six-channel MQDT model parameters for the  $|\nu, L = 2, F = 3/2\rangle$  series of  $^{171}\text{Yb}$  obtained from fit to spectroscopic data presented in Tab. XXX and XXXI. The electronic configuration of the perturbing Rydberg channels  $4f^{13}5d6snp$  is abbreviated as  $5d$ . The rotations  $\mathcal{R}(\theta_{ij})$  are applied in the order  $\mathcal{R}(\theta_{12})\mathcal{R}(\theta_{13})\mathcal{R}(\theta_{14})\mathcal{R}(\theta_{24})\mathcal{R}(\theta_{15})\mathcal{R}(\theta_{25})$ .

$i, \bar{\alpha}, \alpha$	1 ( $F_c = 1$ )	2 ( $F_c = 1$ )	3	4	5	6 ( $F_c = 0$ )
$ i\rangle$	$(6s_{1/2})(nd_{5/2})$	$(6s_{1/2})(nd_{3/2})$	$5d \mathbf{a}$	$5d \mathbf{b}$	$(6p_{1/2})(np_{1/2})$	$(6s_{1/2})(nd_{3/2})$
$I_i$ ( $\text{cm}^{-1}$ )	50 443.217463	50 443.217463	83 967.7	83 967.7	79 725.35	50 442.795744
$ \bar{\alpha}\rangle$	$6snd^1 D_2$	$6snd^3 D_2$	$5d \mathbf{a}$	$5d \mathbf{b}$	$6pnd^1 D_2$	$6snd^3 D_1$
$\mu_{\alpha}^{(0)}$	0.730537124	0.751591782	0.196120394	0.233742396	0.152905343	$\mu_{3D_1}^{3T}$
$\mu_{\alpha}^{(2)}$	-0.000186828866	-0.00114049637	0.0	0.0	0.0	
$\mu_{3D_1}^{3T}$	$\mu_{3D_1}^{(0)} = 0.75258093$	$\mu_{3D_1}^{(2)} = 0.382628525$	$\mu_{3D_1}^{(4)} = -483.120633$			
$V_{\alpha\alpha}$	$\theta_{12} = 0.205496654$	$\theta_{13} = 0.00522401624$	$\theta_{14} = 0.0409502343$	$\theta_{24} = -0.00378075773$	$\theta_{15} = 0.108563952$	$\theta_{25} = 0.0665700438$
$U_{i\bar{\alpha}}$	$-\sqrt{3/5}$	$-\sqrt{2/5}$	0	0	0	0
	$\sqrt{3/5}/2$	$-3/(2\sqrt{10})$	0	0	0	$\sqrt{5/2}/2$
	0	0	1	0	0	0
	0	0	0	1	0	0
	0	0	0	0	1	0
	-1/2	$\sqrt{3/2}/2$	0	0	0	$\sqrt{3/2}/2$

Table XI. Six-channel MQDT model parameters for the  $|\nu, L = 2, F = 5/2\rangle$  series of  $^{171}\text{Yb}$  obtained from fit to spectroscopic data presented in Tab. XXX and XXXI. The electronic configuration of the perturbing Rydberg channels  $4f^{13}5d6snp$  is abbreviated as  $5d$ . The rotations  $\mathcal{R}(\theta_{ij})$  are applied in the order  $\mathcal{R}(\theta_{12})\mathcal{R}(\theta_{13})\mathcal{R}(\theta_{14})\mathcal{R}(\theta_{24})\mathcal{R}(\theta_{15})\mathcal{R}(\theta_{25})$ .

$i, \bar{\alpha}, \alpha$	1 ( $F_c = 1$ )	2 ( $F_c = 1$ )	3	4	5	6 ( $F_c = 0$ )
$ i\rangle$	$(6s_{1/2})(nd_{5/2})$	$(6s_{1/2})(nd_{3/2})$	$5d \mathbf{a}$	$5d \mathbf{b}$	$(6p_{1/2})(np_{1/2})$	$(6s_{1/2})(nd_{5/2})$
$I_i$ ( $\text{cm}^{-1}$ )	50 443.217463	50 443.217463	83 967.7	83 967.7	79 725.35	50 442.795744
$ \bar{\alpha}\rangle$	$6snd^1D_2$	$6snd^3D_2$	$5d \mathbf{a}$	$5d \mathbf{b}$	$6pnd^1D_2$	$6snd^3D_3$
$\mu_{\alpha}^{(0)}$	0.730537124	0.751591782	0.196120394	0.233742396	0.152905343	$\mu_{3D_3}^{\text{tr}}$
$\mu_{\alpha}^{(2)}$	-0.000186828866	-0.00114049637	0.0	0.0	0.0	
$\mu_{3D_3}^{\text{tr}}$	$\mu_{3D_3}^{(0)} = 0.72895315$	$\mu_{3D_3}^{(2)} = -0.20653489$	$\mu_{3D_3}^{(4)} = 220.484722$			
$V_{\alpha\alpha}$	$\theta_{12} = 0.205496654$	$\theta_{13} = 0.00522401624$	$\theta_{14} = 0.0409502343$	$\theta_{24} = -0.00378075773$	$\theta_{15} = 0.108563952$	$\theta_{25} = 0.0665700438$
$U_{i\bar{\alpha}}$	$\sqrt{7/5/2}$	$\sqrt{7/30}$	0	0	0	$-\sqrt{5/3/2}$
	$-\sqrt{2/5}$	$\sqrt{3/5}$	0	0	0	0
	0	0	1	0	0	0
	0	0	0	1	0	0
	0	0	0	0	1	0
	1/2	$\sqrt{1/6}$	0	0	0	$\sqrt{7/3/2}$

## Appendix I: Table of spectroscopic results

1.  $^{174}\text{Yb } ^1S_0$ 

Table XII: Laser spectroscopic data of the  $6sns^1S_0$  Rydberg series included in the determination of the MQDT models. The state energies and the respective uncertainties are taken from Refs. [54, 55] as compiled in [46], and from Ref. [49]. As in Ref. [49], the observed wavenumbers from Ref. [46] are reduced by  $0.1 \text{ cm}^{-1}$ .

State label	$\tilde{\nu}_{\text{exp.}}$ ( $\text{cm}^{-1}$ )	$\tilde{\nu}_{\text{th.}}$ ( $\text{cm}^{-1}$ )	$E_{\text{exp.}} - E_{\text{th.}}$ ( $h \cdot \text{MHz}$ )	Ref.
$6s7s^1S_0$	34 350.55(10)	34 349.227 809	39 638	[46]
$6s8s^1S_0$	41 939.78(10)	41 939.687 015	2788	[46]
$6p^2^3P_0$	42 436.84(10)	42 436.901 198	-1835	[46]
$4f^{13}5d6s6p B$	46 081.44(10)	46 081.618 520	-5352	[46]
$6s10s^1S_0$	46 893.14(10)	46 893.135 082	147	[46]
$6s11s^1S_0$	47 808.39(10)	47 808.418 289	-848	[46]
$6p^2^1S_0$	48 344.28(10)	48 344.184 498	2863	[46]
$6s12s^1S_0$	48 723.39(10)	48 723.404 543	-436	[46]
$6s13s^1S_0$	49 046.33(10)	49 046.326 912	93	[46]
$6s14s^1S_0$	49 302.44(10)	49 302.594 518	-4632	[46]
$6s15s^1S_0$	49 499.14(10)	49 498.896 317	7305	[46]
$6s16s^1S_0$	49 649.95(10)	49 649.937 316	380	[46]
$6s17s^1S_0$	49 767.75(10)	49 767.683 212	2002	[46]
$6s18s^1S_0$	49 859.41(10)	49 859.328 215	2452	[46]
$4f^{13}5d6s6p A$	49 897.22(10)	49 897.247 483	-824	[46]
$6s19s^1S_0$	49 940.64(10)	49 940.693 054	-1591	[46]
$6s20s^1S_0$	50 001.25(10)	50 001.050 710	5975	[46]
$6s21s^1S_0$	50 051.82(10)	50 051.872 944	-1587	[46]
$6s22s^1S_0$	50 094.61(10)	50 094.534 502	2263	[46]
$6s23s^1S_0$	50 130.625 48(10)	50 130.625 177	9.20	[49]
$6s24s^1S_0$	50 161.409 31(10)	50 161.409 005	9.27	[49]
$6s25s^1S_0$	50 187.870 22(10)	50 187.869 988	6.96	[49]
$6s26s^1S_0$	50 210.777 67(10)	50 210.777 495	5.15	[49]
$6s27s^1S_0$	50 230.738 54(10)	50 230.738 437	3.19	[49]
$6s28s^1S_0$	50 248.236 25(10)	50 248.236 135	3.38	[49]
$6s29s^1S_0$	50 263.659 05(10)	50 263.659 083	-0.96	[49]
$6s30s^1S_0$	50 277.322 24(10)	50 277.322 301	-1.91	[49]
$6s31s^1S_0$	50 289.483 45(10)	50 289.483 338	3.36	[49]
$6s32s^1S_0$	50 300.354 17(10)	50 300.354 369	-5.96	[49]
$6s33s^1S_0$	50 310.111 32(10)	50 310.111 439	-3.58	[49]
$6s34s^1S_0$	50 318.901 54(10)	50 318.901 593	-1.72	[49]
$6s35s^1S_0$	50 326.848 50(10)	50 326.848 409	2.69	[49]
$6s36s^1S_0$	50 334.056 42(10)	50 334.056 356	1.90	[49]
$6s37s^1S_0$	50 340.614 22(10)	50 340.614 223	0.00	[49]
$6s38s^1S_0$	50 346.597 83(10)	50 346.597 860	-0.94	[49]
$6s39s^1S_0$	50 352.072 42(10)	50 352.072 378	1.15	[49]
$6s40s^1S_0$	50 357.093 89(10)	50 357.093 914	-0.73	[49]
$6s41s^1S_0$	50 361.711 02(10)	50 361.711 085	-2.03	[49]
$6s42s^1S_0$	50 365.966 16(10)	50 365.966 154	0.21	[49]
$6s43s^1S_0$	50 369.896 15(10)	50 369.896 009	4.15	[49]
$6s44s^1S_0$	50 373.533 00(10)	50 373.532 957	1.17	[49]
$6s45s^1S_0$	50 376.905 46(10)	50 376.905 393	2.06	[49]
$6s46s^1S_0$	50 380.038 43(10)	50 380.038 354	2.28	[49]
$6s47s^1S_0$	50 382.953 98(10)	50 382.953 983	-0.08	[49]
$6s48s^1S_0$	50 385.671 79(10)	50 385.671 922	-3.84	[49]
$6s49s^1S_0$	50 388.209 68(10)	50 388.209 646	1.12	[49]
$6s50s^1S_0$	50 390.582 79(10)	50 390.582 738	1.59	[49]
$6s51s^1S_0$	50 392.805 06(10)	50 392.805 135	-2.20	[49]
$6s52s^1S_0$	50 394.889 10(10)	50 394.889 330	-6.78	[49]
$6s53s^1S_0$	50 396.846 52(10)	50 396.846 547	-0.68	[49]



Table XII (*continued*)

State label	$\tilde{\nu}_{\text{exp.}}$ ( $\text{cm}^{-1}$ )	$\tilde{\nu}_{\text{th.}}$ ( $\text{cm}^{-1}$ )	$E_{\text{exp.}} - E_{\text{th.}}$ ( $h \cdot \text{MHz}$ )	Ref.
$6s54s^1S_0$	50 398.686 86(10)	50 398.686 893	-0.88	[49]
$6s55s^1S_0$	50 400.419 33(10)	50 400.419 491	-4.87	[49]
$6s56s^1S_0$	50 402.052 46(10)	50 402.052 590	-3.93	[49]
$6s57s^1S_0$	50 403.593 72(10)	50 403.593 664	1.82	[49]
$6s58s^1S_0$	50 405.049 40(10)	50 405.049 499	-3.01	[49]
$6s59s^1S_0$	50 406.426 28(10)	50 406.426 267	0.53	[49]
$6s60s^1S_0$	50 407.729 59(10)	50 407.729 591	-0.12	[49]
$6s61s^1S_0$	50 408.964 44(10)	50 408.964 603	-4.85	[49]
$6s62s^1S_0$	50 410.135 85(10)	50 410.135 994	-4.29	[49]
$6s63s^1S_0$	50 411.248 02(10)	50 411.248 060	-1.18	[49]
$6s64s^1S_0$	50 412.304 82(10)	50 412.304 741	2.34	[49]
$6s65s^1S_0$	50 413.309 65(10)	50 413.309 653	-0.19	[49]
$6s66s^1S_0$	50 414.266 24(10)	50 414.266 124	3.52	[49]
$6s67s^1S_0$	50 415.177 21(10)	50 415.177 218	-0.37	[49]
$6s68s^1S_0$	50 416.045 81(10)	50 416.045 760	1.40	[49]
$6s69s^1S_0$	50 416.874 38(10)	50 416.874 360	0.61	[49]
$6s70s^1S_0$	50 417.665 46(10)	50 417.665 428	0.96	[49]
$6s71s^1S_0$	50 418.421 25(10)	50 418.421 198	1.55	[49]
$6s72s^1S_0$	50 419.143 75(10)	50 419.143 740	0.30	[49]
$6s73s^1S_0$	50 419.835 03(10)	50 419.834 972	1.67	[49]
$6s74s^1S_0$	50 420.496 62(10)	50 420.496 678	-1.78	[49]
$6s75s^1S_0$	50 421.130 46(10)	50 421.130 516	-1.75	[49]
$6s76s^1S_0$	50 421.737 94(10)	50 421.738 029	-2.55	[49]
$6s77s^1S_0$	50 422.320 81(10)	50 422.320 655	4.78	[49]
$6s78s^1S_0$	50 422.879 73(10)	50 422.879 734	0.00	[49]
$6s79s^1S_0$	50 423.416 44(10)	50 423.416 519	-2.40	[49]
$6s80s^1S_0$	50 423.932 20(10)	50 423.932 179	0.50	[49]

Table XIII: Spectroscopic data of  $n^1S_0 \leftrightarrow n'^1S_0$  Rydberg-Rydberg transitions obtained by microwave spectroscopy, as presented in Ref. [58] and Ref. [49].

$f$	$i$	$\Delta E_{f \leftarrow i}^{\text{exp.}}$ ( $h \cdot \text{MHz}$ )	$\Delta E_{f \leftarrow i}^{\text{theo.}}$ ( $h \cdot \text{MHz}$ )	$E_{\text{exp.}} - E_{\text{th.}}$ ( $h \cdot \text{MHz}$ )	Ref.
$6s35s^1S_0$	$6s34s^1S_0$	238 239.32(12)	238 239.57	-0.25	[49]
$6s36s^1S_0$	$6s35s^1S_0$	216 088.70(14)	216 088.80	-0.10	[49]
$6s37s^1S_0$	$6s36s^1S_0$	196 599.98(12)	196 599.91	0.07	[49]
$6s38s^1S_0$	$6s37s^1S_0$	179 384.72(12)	179 384.94	-0.22	[49]
$6s39s^1S_0$	$6s38s^1S_0$	164 121.48(12)	164 121.90	-0.42	[49]
$6s40s^1S_0$	$6s39s^1S_0$	150 540.64(10)	150 541.89	-1.25	[49]
$6s41s^1S_0$	$6s40s^1S_0$	138 420.36(80)	138 419.28	1.08	[58]
$6s42s^1S_0$	$6s41s^1S_0$	127 563.40(80)	127 563.77	-0.37	[58]
$6s43s^1S_0$	$6s42s^1S_0$	117 814.16(12)	117 814.08	0.08	[49]
$6s44s^1S_0$	$6s43s^1S_0$	109 032.84(80)	109 032.97	-0.13	[58]
$6s45s^1S_0$	$6s44s^1S_0$	101 103.00(80)	101 103.09	-0.09	[58]
$6s46s^1S_0$	$6s45s^1S_0$	93 924.12(80)	93 923.80	0.32	[58]
$6s47s^1S_0$	$6s46s^1S_0$	87 408.62(80)	87 408.35	0.27	[58]
$6s48s^1S_0$	$6s47s^1S_0$	81 481.92(80)	81 481.78	0.14	[58]
$6s49s^1S_0$	$6s48s^1S_0$	76 079.14(80)	76 079.04	0.10	[58]
$6s50s^1S_0$	$6s49s^1S_0$	71 143.62(80)	71 143.52	0.10	[58]
$6s51s^1S_0$	$6s50s^1S_0$	66 625.94(80)	66 625.79	0.15	[58]
$6s52s^1S_0$	$6s51s^1S_0$	62 482.74(80)	62 482.59	0.15	[58]
$6s53s^1S_0$	$6s52s^1S_0$	58 675.66(80)	58 675.88	-0.22	[58]

Table XIV: Spectroscopic data of  $n^1S_0 \leftrightarrow n'^1S_0$  Rydberg-Rydberg transitions obtained by microwave spectroscopy, as presented in Ref. [58] and Ref. [49].

$f$	$i$	$\Delta E_{f \leftarrow i}^{\text{exp.}} (h \cdot \text{MHz})$	$\Delta E_{f \leftarrow i}^{\text{theo.}} (h \cdot \text{MHz})$	$E_{\text{exp.}} - E_{\text{th.}} (h \cdot \text{MHz})$	Ref.
$6s29s^1S_0$	$6s28d^1D_2$	-235 548.18(22)	-235 549.07	0.89	[49]
$6s30s^1S_0$	$6s29d^1D_2$	-209 275.16(22)	-209 275.15	-0.01	[49]
$6s31s^1S_0$	$6s30d^1D_2$	-186 918.48(12)	-186 918.43	-0.05	[49]
$6s32s^1S_0$	$6s31d^1D_2$	-167 680.52(16)	-167 679.89	-0.63	[49]
$6s33s^1S_0$	$6s32d^1D_2$	-151 009.20(14)	-151 008.75	-0.45	[49]
$6s34s^1S_0$	$6s33d^1D_2$	-136 482.22(10)	-136 481.90	-0.32	[49]
$6s35s^1S_0$	$6s34d^1D_2$	-123 762.40(16)	-123 761.92	-0.48	[49]
$6s36s^1S_0$	$6s35d^1D_2$	-112 576.06(18)	-112 574.97	-1.09	[49]
$6s37s^1S_0$	$6s36d^1D_2$	-102 697.06(14)	-102 696.27	-0.79	[49]
$6s38s^1S_0$	$6s37d^1D_2$	-93 940.32(10)	-93 939.81	-0.51	[49]
$6s39s^1S_0$	$6s38d^1D_2$	-86 151.10(16)	-86 150.54	-0.56	[49]
$6s40s^1S_0$	$6s39d^1D_2$	-79 199.54(18)	-79 198.53	-1.01	[49]
$6s41s^1S_0$	$6s40d^1D_2$	-72 974.18(80)	-72 974.26	0.08	[58]
$6s42s^1S_0$	$6s41d^1D_2$	-67 385.66(80)	-67 385.00	-0.66	[58]
$6s43s^1S_0$	$6s42d^1D_2$	-62 351.88(12)	-62 351.81	-0.07	[49]
$6s44s^1S_0$	$6s43d^1D_2$	-57 807.28(10)	-57 807.27	-0.01	[49]
$6s45s^1S_0$	$6s44d^1D_2$	-53 693.84(80)	-53 693.53	-0.31	[58]
$6s46s^1S_0$	$6s45d^1D_2$	-49 961.68(80)	-49 960.75	-0.93	[58]
$6s47s^1S_0$	$6s46d^1D_2$	-46 566.70(80)	-46 565.88	-0.82	[58]
$6s48s^1S_0$	$6s47d^1D_2$	-43 472.26(80)	-43 471.53	-0.73	[58]
$6s49s^1S_0$	$6s48d^1D_2$	-40 645.06(80)	-40 645.20	0.14	[58]

2.  $^{174}\text{Yb } 1,3D_2$ 

Table XV: Laser spectroscopic data of the  $6snd^{1,3}D_2$  Rydberg series included in the determination of the MQDT models. The state energies and the respective uncertainties are taken from Refs. [54, 55] as compiled in [46], and from Ref. [49].

State label	$\tilde{\nu}_{\text{exp.}}$ ( $\text{cm}^{-1}$ )	$\tilde{\nu}_{\text{th.}}$ ( $\text{cm}^{-1}$ )	$E_{\text{exp.}} - E_{\text{th.}}$ ( $h \cdot \text{MHz}$ )	Ref.
$6s8d^1D_2$	46 405.62(10)	46 403.272 104	70 388	[46]
$6s8d^3D_2$	46 467.69(10)	46 468.043 298	-10 592	[46]
$6p^2^1D_2$	47 420.97(10)	47 421.132 756	-4879	[46]
$6s9d^3D_2$	47 634.40(10)	47 634.131 975	8035	[46]
$6s9d^1D_2$	47 821.74(10)	47 822.162 808	-12 675	[46]
$6s10d^3D_2$	48 357.63(10)	48 353.002 109	138 741	[46]
$6s10d^1D_2$	48 403.49(10)	48 394.683 988	263 998	[46]
$4f^{13}5d6s6p B$	48 762.52(10)	48 760.869 520	49 480	[46]
$6s11d^3D_2$	48 838.14(10)	48 835.934 045	66 133	[46]
$6s11d^1D_2$	48 883.12(10)	48 875.940 853	215 225	[46]
$6s12d^3D_2$	49 161.12(10)	49 161.781 360	-19 827	[46]
$6s12d^1D_2$	49 176.00(10)	49 177.241 316	-37 214	[46]
$6s13d^3D_2$	49 399.10(10)	49 399.198 912	-2965	[46]
$6s13d^1D_2$	49 408.58(10)	49 409.028 480	-13 445	[46]
$6s14d^3D_2$	49 576.36(10)	49 576.392 356	-970	[46]
$6s14d^1D_2$	49 583.28(10)	49 583.267 177	384	[46]
$6s15d^3D_2$	49 712.11(10)	49 712.052 181	1733	[46]
$6s15d^1D_2$	49 717.15(10)	49 717.113 078	1107	[46]
$6s16d^3D_2$	49 818.19(10)	49 818.196 204	-186	[46]
$6s16d^1D_2$	49 822.08(10)	49 822.053 662	790	[46]
$6s17d^3D_2$	49 902.78(10)	49 902.799 738	-592	[46]
$6s17d^1D_2$	49 905.79(10)	49 905.817 418	-822	[46]
$6s18d^3D_2$	49 971.34(10)	49 971.318 220	653	[46]
$6s18d^1D_2$	49 973.69(10)	49 973.727 776	-1132	[46]
$6s19d^3D_2$	50 027.66(10)	50 027.584 183	2273	[46]
$6s19d^1D_2$	50 029.61(10)	50 029.540 314	2089	[46]
$6s20d^3D_2$	50 074.44(10)	50 074.353 479	2594	[46]
$6s20d^1D_2$	50 076.05(10)	50 075.963 231	2601	[46]
$6s21d^3D_2$	50 113.67(10)	50 113.648 731	638	[46]
$6s21d^1D_2$	50 115.18(10)	50 114.988 113	5753	[46]
$6s22d^3D_2$	50 147.03(10)	50 146.981 443	1456	[46]
$6s22d^1D_2$	50 148.59(10)	50 148.105 296	14 531	[46]
$6s23d^3D_2$	50 175.499 46(10)	50 175.499 483	-0.62	[49]
$6s23d^1D_2$	50 176.447 18(10)	50 176.447 102	2.46	[49]
$6s24d^3D_2$	50 200.087 07(10)	50 200.087 073	-0.04	[49]
$6s24d^1D_2$	50 200.884 09(10)	50 200.883 990	3.00	[49]
$6s25d^3D_2$	50 221.433 57(10)	50 221.433 594	-0.64	[49]
$6s25d^1D_2$	50 222.082 36(10)	50 222.082 084	8.12	[49]
$6s26d^3D_2$	50 240.035 78(10)	50 240.036 096	-9.62	[49]
$6s26d^1D_2$	50 240.290 62(10)	50 240.290 082	16.08	[49]
$4f^{13}5d6s6p A$	50 244.240 35(10)	50 244.240 186	4.92	[49]
$6s27d^3D_2$	50 256.489 82(10)	50 256.489 876	-1.52	[49]
$6s27d^1D_2$	50 257.162 36(10)	50 257.162 250	3.21	[49]
$6s28d^3D_2$	50 270.973 04(10)	50 270.972 964	2.41	[49]
$6s28d^1D_2$	50 271.516 35(10)	50 271.516 154	5.95	[49]
$6s29d^3D_2$	50 283.833 88(10)	50 283.833 996	-3.62	[49]
$6s29d^1D_2$	50 284.302 93(10)	50 284.302 968	-1.06	[49]
$6s30d^3D_2$	50 295.305 74(10)	50 295.305 673	2.13	[49]
$6s30d^1D_2$	50 295.718 23(10)	50 295.718 265	-1.06	[49]
$6s31d^3D_2$	50 305.580 85(10)	50 305.581 001	-4.42	[49]
$6s31d^1D_2$	50 305.947 57(10)	50 305.947 568	0.15	[49]
$6s32d^3D_2$	50 314.820 78(10)	50 314.820 687	2.72	[49]

Table XV (continued)

State label	$\tilde{\nu}_{\text{exp.}}$ ( $\text{cm}^{-1}$ )	$\tilde{\nu}_{\text{th.}}$ ( $\text{cm}^{-1}$ )	$E_{\text{exp.}} - E_{\text{th.}}$ ( $h \cdot \text{MHz}$ )	Ref.
$6s32d^1D_2$	50 315.148 60(10)	50 315.148 549	1.68	[49]
$6s33d^3D_2$	50 323.159 28(10)	50 323.159 355	-2.26	[49]
$6s33d^1D_2$	50 323.454 15(10)	50 323.454 139	0.37	[49]
$6s34d^3D_2$	50 330.710 37(10)	50 330.710 452	-2.42	[49]
$6s34d^1D_2$	50 330.976 69(10)	50 330.976 663	0.79	[49]
$6s35d^3D_2$	50 337.570 18(10)	50 337.570 117	1.99	[49]
$6s35d^1D_2$	50 337.811 62(10)	50 337.811 453	4.92	[49]
$6s36d^3D_2$	50 343.820 31(10)	50 343.820 258	1.46	[49]
$6s36d^1D_2$	50 344.039 79(10)	50 344.039 802	-0.29	[49]
$6s37d^3D_2$	50 349.530 86(10)	50 349.531 006	-4.44	[49]
$6s37d^1D_2$	50 349.731 40(10)	50 349.731 355	1.26	[49]
$6s38d^3D_2$	50 354.762 54(10)	50 354.762 686	-4.26	[49]
$6s38d^1D_2$	50 354.946 00(10)	50 354.946 050	-1.39	[49]
$6s39d^3D_2$	50 359.567 54(10)	50 359.567 422	3.40	[49]
$6s39d^1D_2$	50 359.735 65(10)	50 359.735 693	-1.27	[49]
$6s40d^3D_2$	50 363.990 46(10)	50 363.990 436	0.76	[49]
$6s40d^1D_2$	50 364.145 30(10)	50 364.145 244	1.70	[49]
$6s41d^3D_2$	50 368.071 08(10)	50 368.071 117	-1.00	[49]
$6s41d^1D_2$	50 368.213 92(10)	50 368.213 876	1.21	[49]
$6s42d^3D_2$	50 371.843 89(10)	50 371.843 904	-0.30	[49]
$6s42d^1D_2$	50 371.975 78(10)	50 371.975 841	-1.69	[49]
$6s43d^3D_2$	50 375.338 98(10)	50 375.339 009	-0.91	[49]
$6s43d^1D_2$	50 375.461 13(10)	50 375.461 200	-2.10	[49]
$6s44d^3D_2$	50 378.583 09(10)	50 378.583 029	1.83	[49]
$6s44d^1D_2$	50 378.696 44(10)	50 378.696 417	0.55	[49]
$6s45d^3D_2$	50 381.599 38(10)	50 381.599 450	-2.23	[49]
$6s45d^1D_2$	50 381.704 92(10)	50 381.704 865	1.52	[49]
$6s46d^3D_2$	50 384.409 12(10)	50 384.409 077	1.30	[49]
$6s46d^1D_2$	50 384.507 12(10)	50 384.507 253	-3.96	[49]
$6s47d^3D_2$	50 387.030 40(10)	50 387.030 387	0.38	[49]
$6s47d^1D_2$	50 387.121 93(10)	50 387.121 976	-1.38	[49]
$6s48d^3D_2$	50 389.479 83(10)	50 389.479 843	-0.45	[49]
$6s48d^1D_2$	50 389.565 35(10)	50 389.565 424	-2.08	[49]
$6s49d^3D_2$	50 391.772 08(10)	50 391.772 145	-1.91	[49]
$6s49d^1D_2$	50 391.852 20(10)	50 391.852 233	-0.91	[49]
$6s50d^3D_2$	50 393.920 37(10)	50 393.920 454	-2.61	[49]
$6s50d^1D_2$	50 393.995 48(10)	50 393.995 512	-0.82	[49]
$6s51d^3D_2$	50 395.936 56(10)	50 395.936 583	-0.63	[49]
$6s51d^1D_2$	50 396.006 94(10)	50 396.007 025	-2.44	[49]
$6s52d^3D_2$	50 397.831 14(10)	50 397.831 157	-0.55	[49]
$6s52d^1D_2$	50 397.897 32(10)	50 397.897 355	-1.12	[49]
$6s53d^3D_2$	50 399.613 77(10)	50 399.613 755	0.50	[49]
$6s53d^1D_2$	50 399.676 02(10)	50 399.676 045	-0.89	[49]
$6s54d^3D_2$	50 401.292 93(10)	50 401.293 031	-2.90	[49]
$6s54d^1D_2$	50 401.351 71(10)	50 401.351 714	-0.18	[49]
$6s55d^3D_2$	50 402.876 70(10)	50 402.876 817	-3.62	[49]
$6s55d^1D_2$	50 402.932 00(10)	50 402.932 168	-5.00	[49]
$6s56d^3D_2$	50 404.372 20(10)	50 404.372 219	-0.65	[49]
$6s56d^1D_2$	50 404.424 37(10)	50 404.424 486	-3.56	[49]
$6s57d^3D_2$	50 405.785 64(10)	50 405.785 692	-1.51	[49]
$6s57d^1D_2$	50 405.835 01(10)	50 405.835 101	-2.75	[49]
$6s58d^3D_2$	50 407.123 10(10)	50 407.123 115	-0.45	[49]
$6s58d^1D_2$	50 407.169 80(10)	50 407.169 870	-2.13	[49]
$6s59d^3D_2$	50 408.389 84(10)	50 408.389 847	-0.11	[49]
$6s59d^1D_2$	50 408.434 01(10)	50 408.434 135	-3.85	[49]
$6s60d^3D_2$	50 409.590 67(10)	50 409.590 782	-3.25	[49]
$6s60d^1D_2$	50 409.632 64(10)	50 409.632 776	-4.15	[49]

Table XV (*continued*)

State label	$\tilde{\nu}_{\text{exp.}}$ ( $\text{cm}^{-1}$ )	$\tilde{\nu}_{\text{th.}}$ ( $\text{cm}^{-1}$ )	$E_{\text{exp.}} - E_{\text{th.}}$ ( $h \cdot \text{MHz}$ )	Ref.
$6s61d^3D_2$	50 410.730 33(10)	50 410.730 401	-2.17	[49]
$6s61d^1D_2$	50 410.770 16(10)	50 410.770 255	-2.95	[49]
$6s62d^3D_2$	50 411.812 74(10)	50 411.812 808	-1.89	[49]
$6s62d^1D_2$	50 411.850 64(10)	50 411.850 666	-0.83	[49]
$6s63d^3D_2$	50 412.841 59(10)	50 412.841 769	-5.35	[49]
$6s63d^1D_2$	50 412.877 75(10)	50 412.877 762	-0.41	[49]
$6s64d^3D_2$	50 413.820 73(10)	50 413.820 745	-0.33	[49]
$6s64d^1D_2$	50 413.854 96(10)	50 413.854 994	-1.08	[49]
$6s65d^3D_2$	50 414.752 98(10)	50 414.752 923	1.68	[49]
$6s65d^1D_2$	50 414.785 47(10)	50 414.785 539	-2.12	[49]
$6s66d^3D_2$	50 415.641 26(10)	50 415.641 238	0.65	[49]
$6s66d^1D_2$	50 415.672 42(10)	50 415.672 324	2.74	[49]
$6s67d^3D_2$	50 416.488 38(10)	50 416.488 400	-0.64	[49]
$6s67d^1D_2$	50 416.518 07(10)	50 416.518 050	0.52	[49]
$6s68d^3D_2$	50 417.296 94(10)	50 417.296 913	0.78	[49]
$6s68d^1D_2$	50 417.325 29(10)	50 417.325 213	2.37	[49]
$6s69d^3D_2$	50 418.069 21(10)	50 418.069 091	3.44	[49]
$6s69d^1D_2$	50 418.096 09(10)	50 418.096 123	-0.93	[49]
$6s70d^3D_2$	50 418.807 12(10)	50 418.807 080	1.10	[49]
$6s70d^1D_2$	50 418.833 00(10)	50 418.832 919	2.46	[49]
$6s71d^3D_2$	50 419.512 87(10)	50 419.512 869	0.08	[49]
$6s71d^1D_2$	50 419.537 69(10)	50 419.537 584	3.15	[49]
$6s72d^3D_2$	50 420.188 34(10)	50 420.188 305	1.02	[49]
$6s72d^1D_2$	50 420.212 02(10)	50 420.211 959	1.88	[49]
$6s73d^3D_2$	50 420.835 12(10)	50 420.835 102	0.53	[49]
$6s73d^1D_2$	50 420.857 74(10)	50 420.857 757	-0.63	[49]
$6s74d^3D_2$	50 421.455 12(10)	50 421.454 858	7.69	[49]
$6s74d^1D_2$	50 421.476 50(10)	50 421.476 569	-2.15	[49]
$6s75d^3D_2$	50 422.049 16(10)	50 422.049 060	3.01	[49]
$6s75d^1D_2$	50 422.069 91(10)	50 422.069 877	0.89	[49]
$6s76d^3D_2$	50 422.619 15(10)	50 422.619 092	1.86	[49]
$6s76d^1D_2$	50 422.639 24(10)	50 422.639 066	5.08	[49]
$6s77d^3D_2$	50 423.166 27(10)	50 423.166 249	0.52	[49]
$6s77d^1D_2$	50 423.185 41(10)	50 423.185 423	-0.33	[49]
$6s78d^3D_2$	50 423.691 83(10)	50 423.691 737	2.74	[49]
$6s78d^1D_2$	50 423.710 18(10)	50 423.710 155	0.63	[49]
$6s79d^3D_2$	50 424.196 85(10)	50 424.196 688	4.75	[49]
$6s79d^1D_2$	50 424.214 46(10)	50 424.214 387	2.12	[49]
$6s80d^3D_2$	50 424.682 12(10)	50 424.682 155	-1.21	[49]
$6s80d^1D_2$	50 424.699 26(10)	50 424.699 174	2.56	[49]

Table XVI: Spectroscopic data of  $n^1D_2 \leftrightarrow n'^1D_2$  Rydberg-Rydberg transitions obtained by microwave spectroscopy, as presented in Ref. [58] and Ref. [49].

$f$	$i$	$\Delta E_{f \leftarrow i}^{\text{exp.}}$ ( $h \cdot \text{MHz}$ )	$\Delta E_{f \leftarrow i}^{\text{theo.}}$ ( $h \cdot \text{MHz}$ )	$E_{\text{exp.}} - E_{\text{th.}}$ ( $h \cdot \text{MHz}$ )	Ref.
$6s33d^1D_2$	$6s32d^1D_2$	248 996.64(28)	248 995.32	1.32	[49]
$6s34d^1D_2$	$6s33d^1D_2$	225 519.66(12)	225 519.59	0.07	[49]
$6s35d^1D_2$	$6s34d^1D_2$	204 902.10(12)	204 901.85	0.25	[49]
$6s36d^1D_2$	$6s35d^1D_2$	186 721.48(12)	186 721.21	0.27	[49]
$6s37d^1D_2$	$6s36d^1D_2$	170 628.56(14)	170 628.47	0.09	[49]
$6s38d^1D_2$	$6s37d^1D_2$	156 333.20(14)	156 332.64	0.56	[49]
$6s39d^1D_2$	$6s38d^1D_2$	143 589.46(8)	143 589.88	-0.42	[49]
$6s40d^1D_2$	$6s39d^1D_2$	132 194.90(80)	132 195.01	-0.11	[58]
$6s41d^1D_2$	$6s40d^1D_2$	121 974.42(80)	121 974.51	-0.09	[58]

Table XVI (*continued*)

$f$	$i$	$\Delta E_{f \leftarrow i}^{\text{exp.}} (h \cdot \text{MHz})$	$\Delta E_{f \leftarrow i}^{\text{theo.}} (h \cdot \text{MHz})$	$E_{\text{exp.}} - E_{\text{th.}} (h \cdot \text{MHz})$	Ref.
$6s42d^1D_2$	$6s41d^1D_2$	112 780.92(80)	112 780.89	0.03	[58]
$6s43d^1D_2$	$6s42d^1D_2$	104 488.90(80)	104 488.42	0.48	[58]
$6s44d^1D_2$	$6s43d^1D_2$	96 989.66(80)	96 989.35	0.31	[58]
$6s45d^1D_2$	$6s44d^1D_2$	90 191.26(80)	90 191.02	0.24	[58]
$6s46d^1D_2$	$6s45d^1D_2$	84 013.80(80)	84 013.47	0.33	[58]
$6s47d^1D_2$	$6s46d^1D_2$	78 387.84(80)	78 387.43	0.41	[58]
$6s48d^1D_2$	$6s47d^1D_2$	73 253.24(80)	73 252.71	0.53	[58]
$6s49d^1D_2$	$6s48d^1D_2$	68 557.18(80)	68 556.83	0.35	[58]
$6s50d^1D_2$	$6s49d^1D_2$	64 254.32(80)	64 253.89	0.43	[58]
$6s51d^1D_2$	$6s50d^1D_2$	60 303.62(80)	60 303.64	-0.02	[58]
$6s52d^1D_2$	$6s51d^1D_2$	56 670.98(80)	56 670.67	0.31	[58]
$6s53d^1D_2$	$6s52d^1D_2$	53 324.24(80)	53 323.76	0.48	[58]
$6s54d^1D_2$	$6s53d^1D_2$	50 235.96(80)	50 235.30	0.66	[58]
$6s55d^1D_2$	$6s54d^1D_2$	47 381.44(80)	47 380.81	0.63	[58]
$6s56d^1D_2$	$6s55d^1D_2$	44 739.32(80)	44 738.56	0.76	[58]

3.  $^{174}\text{Yb } 1,3P_1$ Table XVII: Spectroscopic data of  $n^{1,3}P_1 \leftrightarrow n'S_0$  Rydberg-Rydberg transitions obtained by microwave spectroscopy in an atomic beam setup as described in App. B and from Ref. [50].

$f$	$i$	$\nu_{f \leftarrow i}$ (MHz)	$\tilde{\nu}_{\text{exp.}}$ ( $\text{cm}^{-1}$ )	$\tilde{\nu}_{\text{th.}}$ ( $\text{cm}^{-1}$ )	$E_{\text{exp.}} - E_{\text{th.}}$ ( $h \cdot \text{MHz}$ )	Ref.
$6s30p^1P_1$	$6s30s^1S_0$	125 083.25(10)	50 281.494 629	50 281.494 630	-0.02	This work
$6s31p^1P_1$	$6s31s^1S_0$	111 552.79(10)	50 293.204 338	50 293.204 334	0.14	This work
$6s32p^1P_1$	$6s32s^1S_0$	99 908.78(10)	50 303.686 967	50 303.686 965	0.07	This work
$6s33p^1P_1$	$6s33s^1S_0$	89 832.20(10)	50 313.107 919	50 313.107 921	-0.05	This work
$6s37p^1P_1$	$6s38s^1S_0$	-118 631.36(10)	50 342.640 744	50 342.640 748	-0.12	This work
$6s38p^1P_1$	$6s39s^1S_0$	-108 614.16(10)	50 348.449 399	50 348.449 403	-0.11	This work
$6s39p^1P_1$	$6s40s^1S_0$	-99 693.21(10)	50 353.768 507	50 353.768 511	-0.13	This work
$6s42p^3P_1$	$6s41s^1S_0$	122 420.24(10)	50 365.794 584	50 365.794 585	-0.01	This work
$6s43p^3P_1$	$6s42s^1S_0$	110 051.61(10)	50 369.637 081	50 369.637 080	0.03	This work
$6s44p^3P_1$	$6s43s^1S_0$	99 037.2(5)	50 373.199 534	50 373.199 536	-0.05	[50]
$6s44p^3P_1$	$6s43s^1S_0$	99 037.32(10)	50 373.199 538	50 373.199 536	0.06	This work
$6s45p^3P_1$	$6s44s^1S_0$	89 241.46(10)	50 376.509 732	50 376.509 732	-0.02	This work
$6s46p^3P_1$	$6s45s^1S_0$	80 542.0(5)	50 379.591 985	50 379.591 983	0.07	[50]
$6s47p^3P_1$	$6s46s^1S_0$	72 826.1(5)	50 382.467 571	50 382.467 572	-0.03	[50]
$6s48p^3P_1$	$6s47s^1S_0$	65 989.5(5)	50 385.155 155	50 385.155 158	-0.08	[50]
$6s48p^1P_1$	$6s47s^1S_0$	106 947.8(5)	50 386.521 377	50 386.521 371	0.18	[50]
$6s49p^3P_1$	$6s48s^1S_0$	59 934.5(5)	50 387.671 122	50 387.671 139	-0.51	[50]
$6s49p^1P_1$	$6s48s^1S_0$	99 874.4(5)	50 389.003 373	50 389.003 366	0.22	[50]
$6s50p^3P_1$	$6s49s^1S_0$	54 572.3(5)	50 390.029 982	50 390.029 985	-0.12	[50]
$6s50p^1P_1$	$6s49s^1S_0$	93 411.1(5)	50 391.325 504	50 391.325 500	0.14	[50]
$6s51p^3P_1$	$6s50s^1S_0$	49 819.2(5)	50 392.244 528	50 392.244 533	-0.17	[50]
$6s51p^1P_1$	$6s50s^1S_0$	87 493.7(5)	50 393.501 214	50 393.501 209	0.15	[50]
$6s52p^3P_1$	$6s51s^1S_0$	45 601.0(5)	50 394.326 221	50 394.326 230	-0.28	[50]
$6s52p^1P_1$	$6s51s^1S_0$	82 065.6(5)	50 395.542 549	50 395.542 548	0.05	[50]
$6s53p^1P_1$	$6s52s^1S_0$	77 077.5(5)	50 397.460 359	50 397.460 355	0.11	[50]
$6s54p^3P_1$	$6s52s^1S_0$	97 186.4(5)	50 398.131 119	50 398.131 122	-0.08	[50]
$6s54p^1P_1$	$6s53s^1S_0$	72 485.4(5)	50 399.264 399	50 399.264 400	-0.02	[50]
$6s55p^3P_1$	$6s53s^1S_0$	90 699.2(5)	50 399.871 946	50 399.871 948	-0.06	[50]
$6s55p^1P_1$	$6s54s^1S_0$	68 251.0(5)	50 400.963 502	50 400.963 504	-0.06	[50]
$6s56p^3P_1$	$6s54s^1S_0$	84 797.5(5)	50 401.515 433	50 401.515 435	-0.06	[50]
$6s57p^3P_1$	$6s55s^1S_0$	79 415.9(5)	50 403.068 521	50 403.068 524	-0.11	[50]
$6s58p^3P_1$	$6s56s^1S_0$	74 497.4(5)	50 404.537 556	50 404.537 558	-0.08	[50]
$6s59p^3P_1$	$6s57s^1S_0$	69 992.0(5)	50 405.928 346	50 405.928 348	-0.06	[50]
$6s59p^1P_1$	$6s57s^1S_0$	97 906.5(5)	50 406.859 474	50 406.859 474	-0.03	[50]
$6s60p^3P_1$	$6s58s^1S_0$	65 856.0(5)	50 407.246 219	50 407.246 223	-0.10	[50]
$6s60p^1P_1$	$6s58s^1S_0$	92 647.5(5)	50 408.139 887	50 408.139 888	-0.02	[50]
$6s61p^3P_1$	$6s58s^1S_0$	103 325.9(5)	50 408.496 080	50 408.496 078	0.06	[50]
$6s61p^1P_1$	$6s59s^1S_0$	87 758.5(5)	50 409.353 576	50 409.353 577	-0.04	[50]
$6s62p^3P_1$	$6s59s^1S_0$	97 617.1(5)	50 409.682 423	50 409.682 420	0.10	[50]
$6s62p^1P_1$	$6s60s^1S_0$	83 207.5(5)	50 410.505 095	50 410.505 098	-0.11	[50]
$6s63p^3P_1$	$6s60s^1S_0$	92 330.3(5)	50 410.809 398	50 410.809 396	0.08	[50]
$6s63p^1P_1$	$6s61s^1S_0$	78 965.8(5)	50 411.598 618	50 411.598 625	-0.20	[50]
$6s64p^3P_1$	$6s61s^1S_0$	87 426.4(5)	50 411.880 834	50 411.880 831	0.09	[50]
$6s64p^1P_1$	$6s62s^1S_0$	75 007.7(5)	50 412.637 982	50 412.637 988	-0.18	[50]
$6s65p^3P_1$	$6s62s^1S_0$	82 870.6(5)	50 412.900 260	50 412.900 254	0.17	[50]
$6s65p^1P_1$	$6s63s^1S_0$	71 309.8(5)	50 413.626 699	50 413.626 704	-0.15	[50]

Table XVIII: Spectroscopic data of  $n^{1,3}P_1 \leftrightarrow n'^{1,3}D_2$  Rydberg-Rydberg transitions obtained by microwave spectroscopy in an atomic beam setup as described in App. B and from Ref. [50].

$f$	$i$	$\nu_{f \leftarrow i}$ (MHz)	$\tilde{\nu}_{\text{exp.}}$ ( $\text{cm}^{-1}$ )	$\tilde{\nu}_{\text{th.}}$ ( $\text{cm}^{-1}$ )	$E_{\text{exp.}} - E_{\text{th.}}$ ( $h \cdot \text{MHz}$ )	Ref.
$6s31p^1P_1$	$6s30d^3D_2$	-114 223.63(10)	50 291.495 583	50 291.495 586	-0.09	This work
$6s32p^1P_1$	$6s31d^3D_2$	-106 695.56(10)	50 302.022 020	50 302.022 017	0.08	This work
$6s34p^1P_1$	$6s33d^3D_2$	-94 535.43(10)	50 320.005 993	50 320.005 989	0.11	This work
$6s35p^1P_1$	$6s34d^3D_2$	-89 631.26(10)	50 327.720 675	50 327.720 672	0.09	This work
$6s36p^1P_1$	$6s35d^3D_2$	-85 360.87(10)	50 334.722 784	50 334.722 784	0.01	This work
$6s37p^1P_1$	$6s36d^3D_2$	-81 628.49(10)	50 341.097 425	50 341.097 427	-0.06	This work
$6s38p^1P_1$	$6s37d^3D_2$	-78 347.73(10)	50 346.917 607	50 346.917 609	-0.06	This work
$6s39p^1P_1$	$6s38d^3D_2$	-75 439.74(10)	50 352.246 287	50 352.246 291	-0.12	This work
$6s40p^1P_1$	$6s39d^3D_2$	-72 831.25(10)	50 357.138 033	50 357.138 035	-0.09	This work
$6s41p^1P_1$	$6s40d^3D_2$	-70 454.79(10)	50 361.640 317	50 361.640 319	-0.07	This work
$6s42p^1P_1$	$6s40d^1D_2$	94 245.3(5)	50 367.288 929	50 367.288 925	0.13	[50]
$6s43p^1P_1$	$6s41d^1D_2$	87 090.9(5)	50 371.118 916	50 371.118 910	0.15	[50]
$6s44p^1P_1$	$6s42d^1D_2$	80 642.9(5)	50 374.665 799	50 374.665 793	0.19	[50]
$6s45p^1P_1$	$6s43d^1D_2$	74 816.2(5)	50 377.956 800	50 377.956 793	0.22	[50]
$6s45p^1P_1$	$6s42d^3D_2$	139 878.25(10)	50 376.509 740	50 376.509 732	0.23	This work
$6s46p^1P_1$	$6s44d^1D_2$	69 537.7(5)	50 381.015 945	50 381.015 938	0.20	[50]
$6s47p^1P_1$	$6s45d^1D_2$	64 744.7(5)	50 383.864 516	50 383.864 501	0.44	[50]
$6s52p^1P_1$	$6s49d^3D_2$	76 569.51(10)	50 394.326 229	50 394.326 230	-0.05	This work
$6s56p^1P_1$	$6s53d^1D_2$	86 628.3(5)	50 402.565 654	50 402.565 649	0.14	[50]
$6s57p^1P_1$	$6s54d^1D_2$	81 734.3(5)	50 404.078 077	50 404.078 075	0.07	[50]
$6s58p^1P_1$	$6s55d^1D_2$	77 202.2(5)	50 405.507 356	50 405.507 355	0.03	[50]

Table XIX: Laser spectroscopic data of the  $6snp^{1,3}P_1$  Rydberg series included in the determination of the MQDT models. The state energies and the respective uncertainties are taken from Refs. [53, 56].

State label	$\tilde{\nu}_{\text{exp.}}$ ( $\text{cm}^{-1}$ )	$\tilde{\nu}_{\text{th.}}$ ( $\text{cm}^{-1}$ )	$E_{\text{exp.}} - E_{\text{th.}}$ ( $h \cdot \text{MHz}$ )	Ref.
$6s12p^1P_1$	48 719.18(10)	48 719.416 230	-6954	[53]
$6s12p^3P_1$	48 761.81(10)	48 763.202 662	-41 756	[53]
$4f^{13}5d^26s A$	49 005.89(10)	49 006.059 508	-5082	[53]
$6s13p^3P_1$	49 110.07(10)	49 107.770 988	68 918	[53]
$6s13p^1P_1$	49 127.40(10)	49 127.675 624	-8263	[53]
$6s14p^1P_1$	49 352.44(10)	49 352.942 891	-15 206	[53]
$6s14p^3P_1$	49 360.60(10)	49 359.516 364	32 481	[53]
$6s15p^1P_1$	49 536.42(10)	49 537.093 278	-20 296	[53]
$6s15p^3P_1$	49 546.55(10)	49 545.470 131	32 369	[53]
$6s16p^1P_1$	49 677.79(10)	49 678.008 399	-6425	[53]
$6s16p^3P_1$	49 688.55(10)	49 687.624 822	27 731	[53]
$6s17p^1P_1$	49 786.40(10)	49 786.407 461	-347	[53]
$6s17p^3P_1$	49 799.20(10)	49 798.493 431	21 177	[53]
$6s18p^1P_1$	49 867.12(10)	49 866.780 676	10 025	[53]
$6s18p^3P_1$	49 886.92(10)	49 886.553 028	10 997	[53]
$4f^{13}5d^26s B$	49 920.00(10)	49 919.800 148	5991	[56]
$6s19p^3P_1$	49 957.87(10)	49 957.619 220	7513	[56]
$6s19p^1P_1$	49 969.14(10)	49 969.330 880	-5853	[56]
$6s20p^3P_1$	50 015.96(10)	50 015.798 337	4842	[56]
$6s20p^1P_1$	50 021.28(10)	50 021.406 997	-3856	[56]
$6s21p^3P_1$	50 064.12(10)	50 064.064 042	1672	[56]
$6s21p^1P_1$	50 067.83(10)	50 067.818 312	368	[56]
$6s22p^3P_1$	50 104.64(10)	50 104.582 172	1728	[56]
$6s22p^1P_1$	50 107.66(10)	50 107.598 166	1998	[56]
$6s23p^3P_1$	50 138.99(10)	50 138.939 066	1522	[56]
$6s23p^1P_1$	50 141.54(10)	50 141.577 594	-979	[56]
$6s24p^3P_1$	50 168.38(10)	50 168.323 080	1701	[56]



Table XIX (*continued*)

State label	$\tilde{\nu}_{\text{exp.}}$ ( $\text{cm}^{-1}$ )	$\tilde{\nu}_{\text{th.}}$ ( $\text{cm}^{-1}$ )	$E_{\text{exp.}} - E_{\text{th.}}$ ( $h \cdot \text{MHz}$ )	Ref.
$6s24p^1P_1$	50 170.82(10)	50 170.724 685	2713	[56]
$6s25p^3P_1$	50 193.66(10)	50 193.645 993	415	[56]
$6s25p^1P_1$	50 195.86(10)	50 195.876 945	-533	[56]
$6s26p^3P_1$	50 215.64(10)	50 215.619 621	606	[56]
$6s26p^1P_1$	50 217.65(10)	50 217.717 500	-1896	[56]
$6s27p^3P_1$	50 234.85(10)	50 234.806 844	1289	[56]
$6s27p^1P_1$	50 236.83(10)	50 236.796 508	1029	[56]
$6s28p^3P_1$	50 251.74(10)	50 251.657 502	2468	[56]
$6s28p^1P_1$	50 253.58(10)	50 253.557 333	652	[56]
$6s29p^3P_1$	50 266.66(10)	50 266.534 501	3758	[56]
$6s29p^1P_1$	50 268.44(10)	50 268.359 101	2407	[56]

4.  $^{174}\text{Yb } ^3P_2$ Table XX: Spectroscopic data of the  $n^3P_2$  Rydberg series obtained by microwave spectroscopy in an atomic beam setup as described in App. B and from Ref. [50].

$f$	$i$	$\nu_{f \leftarrow i}$ (MHz)	$\tilde{\nu}_{\text{exp.}}$ ( $\text{cm}^{-1}$ )	$\tilde{\nu}_{\text{th.}}$ ( $\text{cm}^{-1}$ )	$E_{\text{exp.}} - E_{\text{th.}}$ ( $h \cdot \text{MHz}$ )	Ref.
$6s31p^3P_2$	$6s30d^3D_2$	-54 957.40(10)	50 293.472 491	50 293.472 497	-0.16	This work
$6s36p^3P_2$	$6s34d^3D_2$	172 078.74(10)	50 336.450 381	50 336.450 366	0.46	This work
$6s37p^3P_2$	$6s35d^3D_2$	156 685.04(10)	50 342.796 567	50 342.796 557	0.30	This work
$6s38p^3P_2$	$6s36d^3D_2$	143 074.41(10)	50 348.592 707	50 348.592 706	0.03	This work
$6s39p^3P_2$	$6s37d^3D_2$	130 996.14(10)	50 353.900 567	50 353.900 572	-0.15	This work
$6s40p^3P_2$	$6s38d^3D_2$	120 240.54(10)	50 358.773 479	50 358.773 486	-0.21	This work
$6s43p^3P_2$	$6s41d^3D_2$	94 279.05(10)	50 371.215 928	50 371.215 944	-0.49	This work
$6s43p^3P_2$	$6s41d^3D_2$	94 279.0(5)	50 371.215 926	50 371.215 944	-0.53	[50]
$6s44p^3P_2$	$6s42d^3D_2$	87 302.7(5)	50 374.756 008	50 374.756 022	-0.39	[50]
$6s45p^3P_2$	$6s43d^3D_2$	80 998.1(5)	50 378.040 815	50 378.040 830	-0.44	[50]
$6s46p^3P_2$	$6s44d^3D_2$	75 286.6(5)	50 381.094 320	50 381.094 330	-0.30	[50]
$6s47p^3P_2$	$6s45d^3D_2$	70 099.8(5)	50 383.937 728	50 383.937 737	-0.26	[50]
$6s48p^3P_2$	$6s46d^3D_2$	65 378.8(5)	50 386.589 879	50 386.589 888	-0.29	[50]
$6s49p^3P_2$	$6s47d^3D_2$	61 072.4(5)	50 389.067 543	50 389.067 557	-0.42	[50]
$6s50p^3P_2$	$6s48d^3D_2$	57 136.5(5)	50 391.385 711	50 391.385 718	-0.21	[50]
$6s51p^3P_2$	$6s49d^3D_2$	53 531.7(5)	50 393.557 770	50 393.557 773	-0.10	[50]
$6s52p^3P_2$	$6s50d^3D_2$	50 224.0(5)	50 395.595 746	50 395.595 745	0.03	[50]
$6s53p^3P_2$	$6s51d^3D_2$	47 183.3(5)	50 397.510 448	50 397.510 446	0.07	[50]
$6s54p^3P_2$	$6s51d^3D_2$	101 181.5(5)	50 399.311 634	50 399.311 620	0.43	[50]
$6s55p^3P_2$	$6s52d^3D_2$	95 241.7(5)	50 401.008 078	50 401.008 067	0.36	[50]
$6s56p^3P_2$	$6s53d^3D_2$	89 758.1(5)	50 402.607 763	50 402.607 749	0.42	[50]
$6s57p^3P_2$	$6s54d^3D_2$	84 687.7(5)	50 404.117 908	50 404.117 889	0.58	[50]
$6s58p^3P_2$	$6s55d^3D_2$	79 992.0(5)	50 405.545 063	50 405.545 045	0.52	[50]
$6s59p^3P_2$	$6s56d^3D_2$	75 637.4(5)	50 406.895 211	50 406.895 188	0.67	[50]
$6s60p^3P_2$	$6s57d^3D_2$	71 593.1(5)	50 408.173 781	50 408.173 761	0.61	[50]
$6s61p^3P_2$	$6s58d^3D_2$	67 832.0(5)	50 409.385 747	50 409.385 732	0.45	[50]
$6s62p^3P_2$	$6s58d^3D_2$	102 306.0(5)	50 410.535 676	50 410.535 650	0.79	[50]
$6s63p^3P_2$	$6s59d^3D_2$	97 068.5(5)	50 411.627 703	50 411.627 677	0.78	[50]
$6s64p^3P_2$	$6s60d^3D_2$	92 182.6(5)	50 412.665 663	50 412.665 637	0.79	[50]
$6s65p^3P_2$	$6s61d^3D_2$	87 619.3(5)	50 413.653 067	50 413.653 039	0.84	[50]
$6s66p^3P_2$	$6s62d^3D_2$	83 352.3(5)	50 414.593 141	50 414.593 114	0.82	[50]
$6s67p^3P_2$	$6s63d^3D_2$	79 358.0(5)	50 415.488 867	50 415.488 839	0.81	[50]
$6s68p^3P_2$	$6s64d^3D_2$	75 615.0(5)	50 416.342 990	50 416.342 961	0.86	[50]
$6s69p^3P_2$	$6s65d^3D_2$	72 103.7(5)	50 417.158 043	50 417.158 016	0.81	[50]
$6s70p^3P_2$	$6s66d^3D_2$	68 806.7(5)	50 417.936 383	50 417.936 351	0.94	[50]
$6s71p^3P_2$	$6s67d^3D_2$	65 707.5(5)	50 418.680 167	50 418.680 139	0.83	[50]
$6s72p^3P_2$	$6s68d^3D_2$	62 791.9(5)	50 419.391 425	50 419.391 394	0.92	[50]
$6s73p^3P_2$	$6s69d^3D_2$	60 046.2(5)	50 420.072 017	50 420.071 987	0.90	[50]
$6s74p^3P_2$	$6s70d^3D_2$	57 458.5(5)	50 420.723 690	50 420.723 654	1.06	[50]
$6s75p^3P_2$	$6s71d^3D_2$	55 017.0(5)	50 421.348 039	50 421.348 012	0.80	[50]
$6s76p^3P_2$	$6s72d^3D_2$	52 712.0(5)	50 421.946 588	50 421.946 566	0.66	[50]

Table XXI: Laser spectroscopic data of the  $6snp\ ^3P_2$  Rydberg series included in the determination of the MQDT model. The state energies and the respective uncertainties are taken from Ref. [56].

State label	$\tilde{\nu}_{\text{exp.}}$ ( $\text{cm}^{-1}$ )	$\tilde{\nu}_{\text{th.}}$ ( $\text{cm}^{-1}$ )	$E_{\text{exp.}} - E_{\text{th.}}$ ( $h \cdot \text{MHz}$ )	Ref.
$6s9p\ ^3P_2$	46 184.15	46 159.155 515	749 316	[114]
$6s10p\ ^3P_2$	47 471.10	47 476.475 100	-161 141	[114]
$6s11p\ ^3P_2$	48 233.7(5)	48 251.376 961	-529 942	[115]
$6s12p\ ^3P_2$	48 745.6(5)	48 741.398 200	125 967	[48]
$4f^{13}6s5d^2\ ^3P_2$	48 965.15	48 961.554 736	112 280	[116]
$6s13p\ ^3P_2$	49 136.4(5)	49 138.766 072	-70 933	[48]
$6s14p\ ^3P_2$	49 370.5(5)	49 372.087 230	-47 584	[48]
$6s15p\ ^3P_2$	49 553.0(5)	49 553.219 876	-6592	[48]
$6s16p\ ^3P_2$	49 692.7(5)	49 690.324 708	71 209	[48]
$4f^{13}6s5d^2\ ^1D_2$	49 751.89	49 737.646 161	427 319	[116]
$6s17p\ ^3P_2$	49 805.6(5)	49 805.731 817	-3952	[48]
$6s18p\ ^3P_2$	49 891.51(10)	49 891.644 895	-4044	[56]
$6s19p\ ^3P_2$	49 961.83(10)	49 961.875 954	-1378	[56]
$6s20p\ ^3P_2$	50 019.65(10)	50 019.606 364	1308	[56]
$6s21p\ ^3P_2$	50 067.61(10)	50 067.578 929	931	[56]
$6s22p\ ^3P_2$	50 107.90(10)	50 107.858 387	1248	[56]
$6s23p\ ^3P_2$	50 142.00(10)	50 141.999 179	25	[56]
$6s24p\ ^3P_2$	50 171.19(10)	50 171.184 915	152	[56]
$6s25p\ ^3P_2$	50 196.37(10)	50 196.328 275	1251	[56]
$6s26p\ ^3P_2$	50 218.17(10)	50 218.141 668	849	[56]
$6s27p\ ^3P_2$	50 237.20(10)	50 237.187 508	374	[56]
$6s28p\ ^3P_2$	50 253.96(10)	50 253.914 481	1365	[56]
$6s29p\ ^3P_2$	50 268.74(10)	50 268.683 999	1679	[56]
$6s30p\ ^3P_2$	50 281.83(10)	50 281.789 781	1206	[56]

5.  $^{174}\text{Yb } ^3P_0$ Table XXII: Spectroscopic data of the  $n^3P_0$  Rydberg series obtained by microwave spectroscopy in an atomic beam setup as described in App. B and from Ref. [50].

$f$	$i$	$\Delta E_{f \leftarrow i}^{\text{exp.}} (h \cdot \text{MHz})$	$\tilde{\nu}_{\text{exp.}} (\text{cm}^{-1})$	$\tilde{\nu}_{\text{th.}} (\text{cm}^{-1})$	$E_{\text{exp.}} - E_{\text{th.}} (h \cdot \text{MHz})$	Ref.
$6s31p^3P_0$	$6s29d^3D_2$	-218 431.0(10)	50 288.019 600	50 288.019 553	1.39	This work
$6s32p^3P_0$	$6s30d^3D_2$	-202 698.6(10)	50 298.819 704	50 298.819 627	2.31	This work
$6s33p^3P_0$	$6s32d^3D_2$	-174 533.8(10)	50 317.337 535	50 317.337 448	2.61	This work
$6s34p^3P_0$	$6s33d^3D_2$	-161 992.9(10)	50 325.306 952	50 325.306 979	-0.84	This work
$6s35p^3P_0$	$6s34d^3D_2$	-150 399.2(10)	50 332.553 339	50 332.553 237	3.06	This work
$6s49p^3P_0$	$6s48d^3D_2$	83 958.5(10)	50 389.830 942	50 389.830 905	1.10	This work

Table XXIII: Laser spectroscopic data of the  $6snp^3P_0$  Rydberg series included in the determination of the MQDT model. The state energies and the respective uncertainties are taken from Ref. [56].

State label	$\tilde{\nu}_{\text{exp.}} (\text{cm}^{-1})$	$\tilde{\nu}_{\text{th.}} (\text{cm}^{-1})$	$E_{\text{exp.}} - E_{\text{th.}} (h \cdot \text{MHz})$	Ref.
$6s19p^3P_0$	49 950.00(10)	49 949.938 219	1852	[56]
$6s20p^3P_0$	50 008.89(10)	50 008.811 227	2362	[56]
$6s21p^3P_0$	50 057.80(10)	50 057.648 909	4530	[56]
$6s22p^3P_0$	50 098.66(10)	50 098.616 902	1292	[56]
$6s23p^3P_0$	50 133.38(10)	50 133.329 520	1513	[56]
$6s24p^3P_0$	50 163.01(10)	50 163.009 857	4	[56]
$6s25p^3P_0$	50 188.69(10)	50 188.597 776	2765	[56]
$6s26p^3P_0$	50 210.87(10)	50 210.824 289	1370	[56]
$6s27p^3P_0$	50 230.30(10)	50 230.263 905	1082	[56]
$6s28p^3P_0$	50 247.59(10)	50 247.372 307	6526	[56]
$6s29p^3P_0$	50 262.63(10)	50 262.514 049	3476	[56]
$6s30p^3P_0$	50 276.24(10)	50 275.983 295	7696	[56]

6.  $^{171}\text{Yb S } F = 1/2$ Table XXIV: Laser spectroscopic data of the  $|\nu, L = 0, F = 1/2\rangle$  Rydberg series obtained from laser spectroscopy in an atomic beam setup as described in App. B.

$\nu_{F_c=1}$	$\tilde{\nu}_{\text{exp.}} \text{ (cm}^{-1}\text{)}$	$\tilde{\nu}_{\text{th.}} \text{ (cm}^{-1}\text{)}$	$E_{\text{exp.}} - E_{\text{th.}} \text{ (h} \cdot \text{MHz)}$
26.722 072 4	50 289.539 00(10)	50 289.539 148	-4.31
27.532 673 7	50 298.454 85(10)	50 298.454 960	-3.24
27.720 640 6	50 300.411 47(10)	50 300.411 503	-0.92
28.528 458 0	50 308.384 57(10)	50 308.384 445	3.70
28.719 255 7	50 310.170 00(10)	50 310.170 033	-0.98
29.524 054 2	50 317.324 69(10)	50 317.324 673	0.50
29.717 908 2	50 318.961 81(10)	50 318.961 749	1.92
30.519 412 0	50 325.402 48(10)	50 325.402 483	-0.13
30.716 591 2	50 326.910 28(10)	50 326.910 209	2.17
31.514 494 8	50 332.725 04(10)	50 332.725 133	-2.75
31.715 299 7	50 334.119 94(10)	50 334.119 864	2.14
32.509 273 8	50 339.383 70(10)	50 339.383 773	-2.06
32.714 030 4	50 340.679 43(10)	50 340.679 492	-1.96
33.503 725 4	50 345.456 21(10)	50 345.456 242	-1.01
33.712 781 1	50 346.664 91(10)	50 346.664 934	-0.57
34.497 829 0	50 351.009 28(10)	50 351.009 319	-1.17
34.711 550 2	50 352.141 20(10)	50 352.141 286	-2.70
35.491 566 2	50 356.100 60(10)	50 356.100 551	1.34
35.710 337 2	50 357.164 62(10)	50 357.164 684	-1.77
36.484 919 9	50 360.779 73(10)	50 360.779 737	-0.14
36.709 141 5	50 361.783 67(10)	50 361.783 731	-1.92
37.477 873 9	50 365.090 20(10)	50 365.090 148	1.48
37.707 963 3	50 366.040 69(10)	50 366.040 686	0.17
38.470 412 8	50 369.069 63(10)	50 369.069 523	3.22
38.706 802 7	50 369.972 30(10)	50 369.972 430	-3.93
39.462 522 0	50 372.750 98(10)	50 372.750 899	2.47
39.705 659 8	50 373.611 19(10)	50 373.611 261	-2.16
40.454 187 1	50 376.163 30(10)	50 376.163 291	0.23
40.704 535 0	50 376.985 57(10)	50 376.985 570	0.10
41.445 394 6	50 379.332 38(10)	50 379.332 272	3.36
41.703 428 3	50 380.120 43(10)	50 380.120 387	1.37
42.436 131 0	50 382.280 51(10)	50 382.280 447	1.89
42.702 339 7	50 383.037 80(10)	50 383.037 848	-1.43
43.426 383 7	50 385.027 95(10)	50 385.027 858	2.87
43.701 269 2	50 385.757 62(10)	50 385.757 594	0.76
44.416 140 2	50 387.592 29(10)	50 387.592 326	-1.12
44.700 216 3	50 388.297 13(10)	50 388.297 090	1.27
45.405 388 5	50 389.989 73(10)	50 389.989 735	-0.05
45.699 180 6	50 390.672 04(10)	50 390.671 919	3.48
46.394 117 2	50 392.234 27(10)	50 392.234 288	-0.45
46.698 161 3	50 392.895 97(10)	50 392.896 013	-1.18
47.382 315 0	50 394.338 76(10)	50 394.338 707	1.67
47.697 157 4	50 394.981 85(10)	50 394.981 861	-0.32
48.369 971 1	50 396.314 42(10)	50 396.314 419	-0.09
48.696 167 8	50 396.940 68(10)	50 396.940 685	-0.28
49.357 075 1	50 398.171 66(10)	50 398.171 710	-1.60
49.695 190 8	50 398.782 48(10)	50 398.782 589	-3.29
50.343 617 0	50 399.919 75(10)	50 399.919 862	-3.25
50.694 224 9	50 400.516 61(10)	50 400.516 695	-2.46
51.329 587 0	50 401.567 26(10)	50 401.567 261	-0.13
51.693 267 9	50 402.151 23(10)	50 402.151 248	-0.53
52.692 317 5	50 403.693 68(10)	50 403.693 722	-1.35
53.691 371 2	50 405.150 97(10)	50 405.150 902	1.89
57.232 905 3	50 409.716 13(10)	50 409.716 214	-2.40
58.214 635 5	50 410.836 48(10)	50 410.836 615	-4.10

Table XXIV (*continued*)

$\nu_{F_c=1}$	$\tilde{\nu}_{\text{exp.}} \text{ (cm}^{-1}\text{)}$	$\tilde{\nu}_{\text{th.}} \text{ (cm}^{-1}\text{)}$	$E_{\text{exp.}} - E_{\text{th.}}$ ( $h \cdot \text{MHz}$ )
58.686 577 2	50 411.355 26(10)	50 411.355 318	-1.61
59.195 732 5	50 411.900 92(10)	50 411.901 068	-4.57
59.685 573 4	50 412.412 94(10)	50 412.412 988	-1.35
60.176 191 8	50 412.913 07(10)	50 412.913 240	-5.14
60.684 539 9	50 413.418 74(10)	50 413.418 825	-2.49
61.156 009 8	50 413.876 37(10)	50 413.876 507	-4.06
61.683 468 0	50 414.376 06(10)	50 414.376 154	-2.80
62.135 184 7	50 414.793 79(10)	50 414.793 977	-5.52
62.682 346 9	50 415.288 01(10)	50 415.288 036	-0.84
63.113 716 5	50 415.668 30(10)	50 415.668 516	-6.33
63.681 163 4	50 416.157 22(10)	50 416.157 293	-2.29
64.091 608 0	50 416.502 64(10)	50 416.502 771	-4.08
64.679 901 1	50 416.986 54(10)	50 416.986 526	0.41
65.068 865 1	50 417.299 09(10)	50 417.299 192	-2.98
65.678 538 9	50 417.778 03(10)	50 417.778 142	-3.33
66.045 498 3	50 418.059 89(10)	50 418.060 047	-4.73
66.677 049 5	50 418.534 22(10)	50 418.534 362	-4.24
67.021 524 8	50 418.787 35(10)	50 418.787 441	-2.87
67.675 396 4	50 419.257 30(10)	50 419.257 241	1.69
67.996 970 2	50 419.483 46(10)	50 419.483 333	3.84
68.673 530 9	50 419.948 65(10)	50 419.948 679	-1.01
68.971 873 5	50 420.149 51(10)	50 420.149 546	-0.93
69.671 385 0	50 420.610 50(10)	50 420.610 432	2.16
69.946 291 9	50 420.787 74(10)	50 420.787 786	-1.28
70.668 862 8	50 421.244 15(10)	50 421.244 117	1.06
70.920 311 3	50 421.399 65(10)	50 421.399 654	-0.13
71.665 825 2	50 421.851 10(10)	50 421.851 219	-3.51
71.894 060 6	50 421.986 72(10)	50 421.986 663	1.59
72.662 066 6	50 422.432 96(10)	50 422.433 092	-3.92
72.867 735 2	50 422.550 30(10)	50 422.550 254	1.35
73.657 277 9	50 422.990 90(10)	50 422.990 949	-1.57
73.841 634 0	50 423.091 79(10)	50 423.091 820	-0.80
74.650 995 6	50 423.525 84(10)	50 423.525 857	-0.39
74.816 210 4	50 423.612 77(10)	50 423.612 730	1.12
75.642 548 8	50 424.038 67(10)	50 424.038 725	-1.80
75.792 125 2	50 424.114 33(10)	50 424.114 350	-0.55
76.631 062 4	50 424.530 34(10)	50 424.530 333	0.19
76.770 243 3	50 424.598 07(10)	50 424.598 029	1.30
77.615 632 4	50 425.001 37(10)	50 425.001 426	-1.74
77.751 458 8	50 425.065 04(10)	50 425.065 015	0.81
78.595 708 9	50 425.452 78(10)	50 425.452 897	-3.49
78.736 311 3	50 425.516 38(10)	50 425.516 286	2.75
79.724 690 7	50 425.952 51(10)	50 425.952 463	1.38
80.715 971 8	50 426.373 93(10)	50 426.373 926	0.04
81.512 172 4	50 426.701 20(10)	50 426.701 371	-5.01
81.709 393 3	50 426.781 11(10)	50 426.781 004	3.15
82.478 656 0	50 427.086 06(10)	50 427.086 174	-3.52
82.704 310 0	50 427.174 17(10)	50 427.174 081	2.70
83.443 205 7	50 427.456 82(10)	50 427.456 954	-4.02
83.700 251 6	50 427.553 68(10)	50 427.553 608	2.08
84.406 134 7	50 427.814 45(10)	50 427.814 504	-1.70
84.696 894 3	50 427.920 22(10)	50 427.920 078	4.38
85.367 654 0	50 428.159 50(10)	50 428.159 526	-0.90
85.694 015 0	50 428.274 04(10)	50 428.274 003	1.08
86.327 908 4	50 428.492 54(10)	50 428.492 653	-3.28
86.691 456 4	50 428.615 83(10)	50 428.615 894	-1.85
87.287 001 4	50 428.814 50(10)	50 428.814 463	1.21
87.689 101 3	50 428.946 27(10)	50 428.946 250	0.61
88.245 011 2	50 429.125 51(10)	50 429.125 491	0.62

Table XXIV (*continued*)

$\nu_{F_c=1}$	$\tilde{\nu}_{\text{exp.}} \text{ (cm}^{-1}\text{)}$	$\tilde{\nu}_{\text{th.}} \text{ (cm}^{-1}\text{)}$	$E_{\text{exp.}} - E_{\text{th.}}$ ( $h \cdot \text{MHz}$ )
88.686 855 4	50 429.265 48(10)	50 429.265 556	-2.12
89.202 003 3	50 429.426 33(10)	50 429.426 237	2.86
89.684 634 7	50 429.574 30(10)	50 429.574 271	0.82
90.158 039 1	50 429.717 11(10)	50 429.717 171	-1.92
90.682 353 3	50 429.872 68(10)	50 429.872 834	-4.58
91.113 185 8	50 429.998 69(10)	50 429.998 737	-1.36
91.679 911 4	50 430.161 68(10)	50 430.161 658	0.61
92.067 527 4	50 430.271 35(10)	50 430.271 360	-0.27
92.677 176 2	50 430.441 20(10)	50 430.441 124	2.23
93.021 182 8	50 430.535 48(10)	50 430.535 447	0.99
93.673 950 4	50 430.711 57(10)	50 430.711 581	-0.37
93.974 336 4	50 430.791 46(10)	50 430.791 403	1.73
94.669 911 9	50 430.973 36(10)	50 430.973 330	0.88
94.927 298 5	50 431.039 65(10)	50 431.039 638	0.43
95.664 490 5	50 431.226 62(10)	50 431.226 600	0.54
95.880 627 8	50 431.280 49(10)	50 431.280 600	-3.43
96.656 611 3	50 431.471 53(10)	50 431.471 495	1.17
96.835 388 2	50 431.514 90(10)	50 431.514 826	2.15
97.644 233 1	50 431.707 95(10)	50 431.707 903	1.44
97.793 610 3	50 431.743 09(10)	50 431.743 037	1.44
98.624 046 8	50 431.935 51(10)	50 431.935 459	1.49
98.758 592 1	50 431.966 23(10)	50 431.966 178	1.44
99.733 293 0	50 432.185 08(10)	50 432.185 023	1.73
100.717 156 5	50 432.399 53(10)	50 432.399 514	0.38
101.707 046 1	50 432.609 14(10)	50 432.609 066	2.25
102.700 291 2	50 432.813 37(10)	50 432.813 269	3.02
103.695 357 4	50 433.011 96(10)	50 433.011 989	-0.78
104.337 310 1	50 433.137 10(10)	50 433.137 185	-2.66
104.691 419 8	50 433.205 37(10)	50 433.205 261	3.27
105.277 816 2	50 433.316 52(10)	50 433.316 487	1.11
105.688 004 5	50 433.393 24(10)	50 433.393 192	1.36
106.216 927 0	50 433.490 80(10)	50 433.490 791	0.20
106.684 795 5	50 433.576 10(10)	50 433.575 917	5.38
107.154 853 1	50 433.660 34(10)	50 433.660 321	0.51
107.681 527 8	50 433.753 58(10)	50 433.753 582	-0.16
108.091 797 1	50 433.825 37(10)	50 433.825 287	2.56
108.677 903 5	50 433.926 30(10)	50 433.926 319	-0.61
109.028 016 8	50 433.985 91(10)	50 433.985 896	0.54
109.673 478 8	50 434.094 32(10)	50 434.094 237	2.54
109.963 927 9	50 434.142 36(10)	50 434.142 368	-0.20
110.667 430 8	50 434.257 45(10)	50 434.257 381	2.01
110.900 332 1	50 434.294 94(10)	50 434.294 976	-1.15
111.657 970 6	50 434.415 69(10)	50 434.415 650	1.23
111.839 000 4	50 434.444 20(10)	50 434.444 121	2.38
112.640 970 0	50 434.568 69(10)	50 434.568 604	2.68
112.784 045 2	50 434.590 68(10)	50 434.590 534	4.35
113.742 734 5	50 434.735 45(10)	50 434.735 347	2.96
114.718 444 8	50 434.879 13(10)	50 434.879 019	3.38
115.705 371 9	50 435.020 73(10)	50 435.020 661	1.97
116.697 553 3	50 435.159 51(10)	50 435.159 450	1.88
117.355 112 0	50 435.249 50(10)	50 435.249 498	0.01
117.692 094 7	50 435.295 12(10)	50 435.295 061	1.75
118.280 186 1	50 435.373 73(10)	50 435.373 646	2.43
118.687 687 6	50 435.427 47(10)	50 435.427 416	1.56
119.203 551 7	50 435.494 70(10)	50 435.494 694	0.10
119.683 618 9	50 435.556 53(10)	50 435.556 524	0.28
120.125 636 5	50 435.612 85(10)	50 435.612 800	1.59

7.  $^{171}\text{Yb S } F = 3/2$ 

Table XXV: Spectroscopic data of the  $|\nu, L = 0, F = 3/2\rangle$  Rydberg series obtained from microwave spectroscopy in an atomic beam setup as described in App. B between  $f = |\nu, L = 0, F = 3/2\rangle$  and  $i = |\nu', L = 0, F = 1/2\rangle$  (a) or  $i = |\nu', L = 2, F = 5/2\rangle$  (b) states.

$\nu_{F_c=1}^f$	$\nu_{F_c=1}^i$	$\nu_{f \leftarrow i}$ (MHz)	$\tilde{\nu}_{\text{exp.}}$ ( $\text{cm}^{-1}$ )	$\tilde{\nu}_{\text{th.}}$ ( $\text{cm}^{-1}$ )	$E_{\text{exp.}} - E_{\text{th.}}$ ( $h \cdot \text{MHz}$ )
42.561 535 7	41.703 428 3 <sup>a</sup>	75 510.49(10)	50 382.533 715	50 382.533 582	4.01
43.561 481 7	42.281 582 8 <sup>b</sup>	106 550.02(10)	50 385.282 853	50 385.282 798	1.66
44.561 433 9	43.281 525 6 <sup>b</sup>	99 434.19(10)	50 387.849 037	50 387.849 039	-0.06



8.  $^{171}\text{Yb P } F = 1/2$ Table XXVI: Spectroscopic data of the  $|\nu, L = 1, F = 1/2\rangle$  Rydberg series obtained from microwave spectroscopy in an atomic beam setup as described in App. B between  $i = |\nu, L = 0, F = 1/2\rangle$  and  $f = |\nu', L = 1, F = 1/2\rangle$ .

$\nu_{F_c=1}^f$	$\nu_{F_c=1}^i$	$\nu_{f \leftarrow i}$ (MHz)	$\tilde{\nu}_{\text{exp.}}$ ( $\text{cm}^{-1}$ )	$\tilde{\nu}_{\text{th.}}$ ( $\text{cm}^{-1}$ )	$E_{\text{exp.}} - E_{\text{th.}}$ ( $h \cdot \text{MHz}$ )
28.056 078 6	27.720 640 6	101 759.03(10)	50 303.805 819	50 303.805 862	-1.27
29.529 571 6	29.717 908 2	-47 673.09(10)	50 317.371 545	50 317.371 713	-5.03
29.827 855 1	29.717 908 2	27 406.71(10)	50 319.875 938	50 319.876 086	-4.42
30.511 335 0	30.716 591 2	-47 064.40(10)	50 325.340 310	50 325.340 098	6.34
31.052 537 2	30.716 591 2	75 043.07(10)	50 329.413 376	50 329.413 168	6.26
32.051 390 6	31.715 299 7	68 236.65(10)	50 336.395 994	50 336.395 864	3.90
33.050 225 4	32.714 030 4	62 222.71(10)	50 342.755 018	50 342.754 965	1.58
33.735 909 0	34.711 550 2	-160 206.00(10)	50 346.797 389	50 346.797 273	3.49
34.049 024 0	33.712 781 1	56 886.78(10)	50 348.562 472	50 348.562 480	-0.25
34.709 339 5	35.710 337 2	-150 943.26(10)	50 352.129 759	50 352.129 684	2.24
35.047 769 8	34.711 550 2	52 133.44(10)	50 353.880 271	50 353.880 326	-1.65
35.438 633 2	35.710 337 2	-39 707.34(10)	50 355.840 190	50 355.840 111	2.34
35.438 633 2	34.711 550 2	110 889.87(10)	50 355.840 174	50 355.840 111	1.89
35.681 564 6	34.711 550 2	146 435.93(10)	50 357.025 863	50 357.025 847	0.48
37.045 032 5	36.709 141 5	44 067.61(10)	50 363.253 668	50 363.253 772	-3.12
37.623 559 6	36.709 141 5	117 229.07(10)	50 365.694 072	50 365.694 025	1.39
38.043 510 8	37.707 963 3	40 630.85(10)	50 367.395 986	50 367.396 097	-3.32
38.594 165 0	37.707 963 3	105 037.84(10)	50 369.544 372	50 369.544 272	2.99
39.041 856 8	38.706 802 7	37 523.91(10)	50 371.224 092	50 371.224 202	-3.28
39.565 229 2	38.706 802 7	94 255.01(10)	50 373.116 438	50 373.116 272	5.00
40.040 043 2	39.705 659 8	34 705.14(10)	50 374.768 900	50 374.769 001	-3.03
40.378 777 9	39.705 659 8	68 981.76(10)	50 375.912 245	50 375.912 603	-10.73
40.537 390 8	39.705 659 8	84 758.71(10)	50 376.438 507	50 376.438 268	7.18
41.038 037 8	40.704 535 0	32 138.58(10)	50 378.057 598	50 378.057 687	-2.66
41.511 322 5	40.704 535 0	76 440.13(10)	50 379.535 339	50 379.535 035	9.11
42.035 801 4	41.703 428 3	29 793.00(10)	50 381.114 174	50 381.114 248	-2.20
42.487 653 8	41.703 428 3	69 195.41(10)	50 382.428 497	50 382.428 148	10.45
43.033 286 8	42.702 339 7	27 641.05(10)	50 383.959 855	50 383.959 911	-1.70
43.334 876 0	42.702 339 7	52 272.09(10)	50 384.781 458	50 384.781 848	-11.69
44.030 435 9	43.701 269 2	25 658.58(10)	50 386.613 472	50 386.613 510	-1.15
44.317 344 3	43.701 269 2	47 549.92(10)	50 387.343 688	50 387.344 041	-10.56
44.449 084 0	43.701 269 2	57 485.49(10)	50 387.675 103	50 387.674 749	10.61
45.027 178 0	44.700 216 3	23 824.08(10)	50 389.091 776	50 389.091 796	-0.59
45.298 603 0	44.700 216 3	43 202.96(10)	50 389.738 186	50 389.738 485	-8.95
45.434 206 8	44.700 216 3	52 777.45(10)	50 390.057 557	50 390.057 237	9.58
46.279 125 7	45.699 180 6	39 226.39(10)	50 391.980 371	50 391.980 613	-7.27
46.421 829 9	45.699 180 6	48 671.25(10)	50 392.295 418	50 392.295 141	8.29
47.019 075 3	45.699 180 6	87 199.79(10)	50 393.580 591	50 393.580 576	0.46
47.259 442 2	46.698 161 3	35 615.51(10)	50 394.084 019	50 394.084 210	-5.73
47.411 481 3	46.698 161 3	45 060.07(10)	50 394.399 055	50 394.398 826	6.88
48.014 000 1	46.698 161 3	81 555.28(10)	50 395.616 405	50 395.616 371	1.00
48.240 037 0	47.697 157 4	32 359.65(10)	50 396.061 263	50 396.061 412	-4.48
48.402 721 0	47.697 157 4	41 856.84(10)	50 396.378 055	50 396.377 868	5.62
49.008 055 6	47.697 157 4	76 327.23(10)	50 397.527 864	50 397.527 823	1.22
49.221 310 7	48.696 167 8	29 441.79(10)	50 397.922 757	50 397.922 873	-3.47
49.395 189 9	48.696 167 8	38 993.03(10)	50 398.241 353	50 398.241 201	4.55
50.001 080 9	51.693 267 9	-84 739.02(10)	50 399.324 659	50 399.324 602	1.68
50.203 581 3	51.693 267 9	-74 149.39(10)	50 399.677 890	50 399.677 980	-2.67
50.992 910 4	52.692 317 5	-80 290.56(10)	50 401.015 517	50 401.015 460	1.71
51.187 095 9	52.692 317 5	-70 713.28(10)	50 401.334 981	50 401.335 052	-2.11
51.382 789 3	50.694 224 9	34 082.43(10)	50 401.653 562	50 401.653 466	2.88
52.172 036 8	50.694 224 9	71 492.88(10)	50 402.901 440	50 402.901 498	-1.71
52.377 565 3	50.694 224 9	80 963.58(10)	50 403.217 349	50 403.217 275	2.22
53.372 829 5	51.693 267 9	76 266.52(10)	50 404.695 225	50 404.695 166	1.79
54.945 809 2	53.691 371 2	51 515.52(10)	50 406.869 275	50 406.869 216	1.77

Table XXVI (*continued*)

$\nu_{F_c=1}^f$	$\nu_{F_c=1}^i$	$\nu_{f \leftarrow i}$ (MHz)	$\tilde{\nu}_{\text{exp.}}$ ( $\text{cm}^{-1}$ )	$\tilde{\nu}_{\text{th.}}$ ( $\text{cm}^{-1}$ )	$E_{\text{exp.}} - E_{\text{th.}}$ ( $h \cdot \text{MHz}$ )
55.136 175 4	53.691 371 2	59 024.72(10)	50 407.119 755	50 407.119 779	-0.72
57.119 532 8	59.685 573 4	-84 837.58(10)	50 409.583 110	50 409.583 093	0.52
59.855 484 2	58.686 577 2	36 944.08(10)	50 412.587 640	50 412.587 628	0.36
60.102 514 3	58.686 577 2	44 478.23(10)	50 412.838 952	50 412.838 897	1.66
60.348 093 5	58.686 577 2	51 874.16(10)	50 413.085 654	50 413.085 638	0.48
60.834 218 1	59.685 573 4	34 544.86(10)	50 413.565 280	50 413.565 279	0.02
61.098 322 0	59.685 573 4	42 215.38(10)	50 413.821 141	50 413.821 075	1.99
61.345 318 7	59.685 573 4	49 296.06(10)	50 414.057 327	50 414.057 318	0.28
62.094 654 6	60.684 539 9	40 115.56(10)	50 414.756 936	50 414.756 860	2.26
62.789 215 9	61.683 468 0	30 184.97(10)	50 415.383 016	50 415.383 029	-0.37
63.091 413 1	61.683 468 0	38 162.58(10)	50 415.649 121	50 415.649 035	2.57
63.340 104 8	61.683 468 0	44 637.60(10)	50 415.865 104	50 415.865 094	0.32
63.765 591 7	61.683 468 0	55 543.54(10)	50 416.228 887	50 416.228 903	-0.47
64.088 515 7	62.682 346 9	36 342.27(10)	50 416.500 284	50 416.500 193	2.71
64.337 630 3	62.682 346 9	42 530.52(10)	50 416.706 702	50 416.706 691	0.32
64.741 273 6	62.682 346 9	52 409.07(10)	50 417.036 215	50 417.036 235	-0.61
65.085 894 6	63.681 163 4	34 642.93(10)	50 417.312 856	50 417.312 753	3.09
65.335 220 6	63.681 163 4	40 556.15(10)	50 417.510 100	50 417.510 086	0.41
65.716 292 6	63.681 163 4	49 467.22(10)	50 417.807 341	50 417.807 363	-0.66
66.083 493 4	62.682 346 9	83 973.07(10)	50 418.089 076	50 418.088 968	3.26
66.332 857 1	64.679 901 1	38 704.12(10)	50 418.277 557	50 418.277 543	0.42
66.690 675 1	64.679 901 1	46 704.54(10)	50 418.544 422	50 418.544 447	-0.75
67.081 264 1	64.679 901 1	55 297.41(10)	50 418.831 049	50 418.830 934	3.45

Table XXVII: Laser spectroscopic data of the  $|\nu, L = 1, F = 1/2\rangle$  Rydberg series from three-photon laser spectroscopy as presented in Ref. [89].

$\nu_{F_c=1}$	$\tilde{\nu}_{\text{exp.}} \text{ (cm}^{-1}\text{)}$	$\tilde{\nu}_{\text{th.}} \text{ (cm}^{-1}\text{)}$	$E_{\text{exp.}} - E_{\text{th.}}$ ( $h \cdot \text{MHz}$ )	Ref.
9.066 682 8	49 110.224 85	49 108.294 862	57 859.50	[89]
9.133 826 5	49 127.256 70	49 127.849 033	-17 757.61	[89]
10.039 339 5	49 352.327 78	49 354.431 167	-63 057.88	[89]
10.062 171 4	49 360.540 57	49 359.366 654	35 193.16	[89]
11.011 692 9	49 536.123 72	49 538.225 455	-63 008.45	[89]
11.056 559 1	49 546.587 00	49 545.555 253	30 931.05	[89]
11.966 350 4	49 677.426 88	49 676.863 351	16 894.26	[89]
12.052 432 9	49 688.619 06	49 687.771 371	25 413.16	[89]
12.944 223 6	49 786.261 19	49 788.278 379	-60 473.75	[89]
13.047 997 1	49 799.135 02	49 798.654 692	14 399.87	[89]
13.849 087 5	49 867.050 59	49 871.066 544	-120 395.20	[89]
14.042 300 4	49 886.878 77	49 886.703 073	5267.23	[89]
15.034 434 3	49 957.802 87	49 957.729 204	2208.46	[89]
15.252 034 5	49 969.080 89	49 971.483 271	-72 021.44	[89]
16.024 010 7	50 015.794 93	50 015.841 139	-1385.32	[89]
16.137 499 4	50 021.255 32	50 021.831 143	-17 262.59	[89]
17.011 969 8	50 063.991 63	50 064.038 965	-1419.08	[89]
17.100 663 1	50 067.877 19	50 067.962 016	-2542.98	[89]
17.999 651 3	50 104.481 11	50 104.510 035	-867.26	[89]
18.085 019 8	50 107.684 46	50 107.700 156	-470.44	[89]
18.987 587 1	50 138.822 72	50 138.839 405	-500.08	[89]
19.076 768 5	50 141.678 94	50 141.678 608	9.81	[89]
19.975 725 4	50 168.198 20	50 168.207 912	-291.19	[89]
20.071 668 9	50 170.834 10	50 170.830 745	100.54	[89]
20.963 854 4	50 193.516 27	50 193.522 017	-172.14	[89]
21.068 134 4	50 195.991 33	50 195.987 712	108.42	[89]
23.926 157 6	50 251.523 38	50 251.524 152	-23.10	[89]
24.061 544 8	50 253.676 99	50 253.675 286	50.98	[89]
25.897 661 5	50 279.598 84	50 279.599 204	-10.90	[89]
26.058 574 0	50 281.614 62	50 281.613 661	28.67	[89]
30.807 108 3	50 327.592 29	50 327.592 670	-11.48	[89]
31.052 584 4	50 329.413 65	50 329.413 514	3.95	[89]
35.681 586 7	50 357.025 33	50 357.025 954	-18.73	[89]
36.046 447 4	50 358.762 00	50 358.761 978	0.66	[89]
36.652 864 5	50 361.533 18	50 361.533 471	-8.64	[89]
37.045 024 5	50 363.253 81	50 363.253 738	2.24	[89]
37.623 573 5	50 365.693 82	50 365.694 083	-7.88	[89]
38.043 493 8	50 367.396 14	50 367.396 029	3.25	[89]
38.594 184 1	50 369.544 25	50 369.544 345	-2.74	[89]
39.041 832 1	50 371.223 89	50 371.224 111	-6.68	[89]
39.565 260 3	50 373.116 32	50 373.116 382	-1.96	[89]
40.040 012 4	50 374.768 94	50 374.768 896	1.18	[89]
40.537 439 4	50 376.437 59	50 376.438 428	-25.21	[89]
41.038 002 0	50 378.057 57	50 378.057 573	-0.18	[89]
47.019 036 4	50 393.580 37	50 393.580 494	-3.77	[89]
50.203 547 6	50 399.677 12	50 399.677 921	-23.97	[89]
50.388 693 1	50 399.996 71	50 399.997 292	-17.58	[89]
54.146 554 7	50 405.787 31	50 405.788 226	-27.58	[89]
54.368 547 1	50 406.093 00	50 406.093 258	-7.72	[89]
55.930 278 2	50 408.138 39	50 408.137 539	25.56	[89]
56.127 188 1	50 408.382 22	50 408.383 248	-30.88	[89]
56.360 831 0	50 408.671 04	50 408.671 459	-12.63	[89]

9.  $^{171}\text{Yb P } F = 3/2$ Table XXVIII: Spectroscopic data of the  $|\nu, L = 1, F = 3/2\rangle$  Rydberg series obtained from microwave spectroscopy in an atomic beam setup as described in App. B between  $i = |\nu, L = 0, F = 1/2\rangle$  and  $f = |\nu', L = 1, F = 3/2\rangle$ .

$\nu_{F_c=1}^f$	$\nu_{F_c=1}^i$	$\nu_{f \leftarrow i}$ (MHz)	$\tilde{\nu}_{\text{exp.}}$ ( $\text{cm}^{-1}$ )	$\tilde{\nu}_{\text{th.}}$ ( $\text{cm}^{-1}$ )	$E_{\text{exp.}} - E_{\text{th.}}$ ( $h \cdot \text{MHz}$ )
28.030 810 7	27.720 640 6	94 221.66(10)	50 303.554 400	50 303.554 408	-0.25
28.071 187 8	27.720 640 6	106 260.55(10)	50 303.955 974	50 303.955 897	2.30
29.858 598 9	29.717 908 2	35 019.09(10)	50 320.129 860	50 320.129 951	-2.73
30.840 614 6	30.716 591 2	27 991.62(10)	50 327.843 909	50 327.843 771	4.12
31.015 855 6	30.716 591 2	66 958.10(10)	50 329.143 691	50 329.143 822	-3.93
31.068 418 4	30.716 591 2	78 522.04(10)	50 329.529 422	50 329.529 484	-1.86
32.800 485 7	33.712 781 1	-163 250.19(10)	50 341.219 493	50 341.219 318	5.27
33.004 400 8	32.714 030 4	53 847.84(10)	50 342.475 663	50 342.475 800	-4.10
33.066 921 8	32.714 030 4	65 261.55(10)	50 342.856 383	50 342.856 392	-0.28
33.778 286 5	34.711 550 2	-152 958.42(10)	50 347.039 143	50 347.039 054	2.64
33.998 170 8	33.712 781 1	48 388.47(10)	50 348.278 999	50 348.279 106	-3.20
34.066 263 3	33.712 781 1	59 758.58(10)	50 348.658 265	50 348.658 257	0.24
34.754 713 3	35.710 337 2	-143 820.20(10)	50 352.367 358	50 352.367 367	-0.27
34.991 584 3	34.711 550 2	43 525.38(10)	50 353.593 137	50 353.593 200	-1.91
35.065 657 1	34.711 550 2	54 867.19(10)	50 353.971 459	50 353.971 446	0.39
35.729 883 6	34.711 550 2	153 415.52(10)	50 357.258 677	50 357.258 810	-3.99
35.984 626 1	35.710 337 2	39 178.15(10)	50 358.471 526	50 358.471 541	-0.42
36.065 098 0	35.710 337 2	50 504.09(10)	50 358.849 319	50 358.849 305	0.42
36.977 281 0	36.709 141 5	35 279.35(10)	50 362.960 524	50 362.960 477	1.39
37.064 581 1	36.709 141 5	46 599.12(10)	50 363.338 110	50 363.338 099	0.35
37.677 287 3	36.709 141 5	123 844.31(10)	50 365.914 732	50 365.914 964	-6.95
37.969 534 0	37.707 963 3	31 771.80(10)	50 367.100 480	50 367.100 360	3.59
38.064 102 2	37.707 963 3	43 093.02(10)	50 367.478 115	50 367.478 108	0.21
38.650 104 3	37.707 963 3	111 416.29(10)	50 369.757 134	50 369.757 376	-7.26
38.961 370 1	38.706 802 7	28 607.17(10)	50 370.926 662	50 370.926 446	6.48
39.063 657 4	38.706 802 7	39 935.50(10)	50 371.304 535	50 371.304 535	-0.02
39.622 800 1	38.706 802 7	100 345.82(10)	50 373.319 606	50 373.319 834	-6.84
39.952 774 4	39.705 659 8	25 744.76(10)	50 374.470 014	50 374.469 651	10.89
40.063 243 3	39.705 659 8	37 083.96(10)	50 374.848 249	50 374.848 254	-0.13
40.595 747 7	39.705 659 8	90 497.21(10)	50 376.629 923	50 376.630 122	-5.95
40.943 732 5	40.704 535 0	23 151.73(10)	50 377.757 829	50 377.757 177	19.54
41.062 857 0	40.704 535 0	34 501.65(10)	50 378.136 421	50 378.136 431	-0.28
41.569 301 6	40.704 535 0	81 748.21(10)	50 379.712 397	50 379.712 554	-4.71
42.062 495 7	41.703 428 3	32 157.17(10)	50 381.193 034	50 381.193 048	-0.42
42.543 771 7	41.703 428 3	73 986.21(10)	50 382.588 301	50 382.588 413	-3.34
43.062 157 1	42.702 339 7	30 023.54(10)	50 384.039 326	50 384.039 341	-0.45
44.061 839 2	43.701 269 2	28 077.18(10)	50 386.694 148	50 386.694 166	-0.54
44.902 820 2	43.701 269 2	90 943.91(10)	50 388.791 156	50 388.791 580	-12.71
45.061 540 1	44.700 216 3	26 297.88(10)	50 389.174 293	50 389.174 312	-0.58
45.474 791 3	44.700 216 3	55 611.41(10)	50 390.152 087	50 390.152 082	0.17
45.891 339 4	44.700 216 3	84 351.63(10)	50 391.110 758	50 391.111 042	-8.51
46.061 258 1	45.699 180 6	24 667.90(10)	50 391.494 752	50 391.494 771	-0.58
46.454 692 8	45.699 180 6	50 822.88(10)	50 392.367 188	50 392.367 163	0.77
46.879 332 4	45.699 180 6	78 308.34(10)	50 393.284 005	50 393.284 209	-6.13
47.060 991 8	45.699 180 6	89 848.41(10)	50 393.668 940	50 393.668 959	-0.56
47.436 073 1	46.698 161 3	46 571.54(10)	50 394.449 473	50 394.449 430	1.28
47.866 787 7	46.698 161 3	72 758.62(10)	50 395.322 979	50 395.323 130	-4.52
48.060 739 9	46.698 161 3	84 328.11(10)	50 395.708 896	50 395.708 912	-0.47
48.418 886 7	47.697 157 4	42 790.10(10)	50 396.409 185	50 396.409 139	1.39
48.853 694 2	47.697 157 4	67 653.05(10)	50 397.238 524	50 397.238 638	-3.43
49.060 501 1	47.697 157 4	79 252.57(10)	50 397.625 442	50 397.625 455	-0.38
49.403 062 4	48.696 167 8	39 419.62(10)	50 398.255 582	50 398.255 534	1.44
50.060 274 5	51.693 267 9	-81 630.86(10)	50 399.428 335	50 399.428 343	-0.23
50.388 513 1	48.696 167 8	91 626.72(10)	50 399.997 023	50 399.996 983	1.19
50.825 818 0	52.692 317 5	-88 626.40(10)	50 400.737 464	50 400.737 522	-1.74

Table XXVIII (*continued*)

$\nu_{F_c=1}^f$	$\nu_{F_c=1}^i$	$\nu_{f \leftarrow i}$ (MHz)	$\tilde{\nu}_{\text{exp.}}$ ( $\text{cm}^{-1}$ )	$\tilde{\nu}_{\text{th.}}$ ( $\text{cm}^{-1}$ )	$E_{\text{exp.}} - E_{\text{th.}}$ ( $h \cdot \text{MHz}$ )
51.375 143 9	50.694 224 9	33 709.67(10)	50 401.641 128	50 401.641 094	1.02
51.811 015 5	50.694 224 9	54 590.95(10)	50 402.337 653	50 402.337 693	-1.21
52.362 857 6	50.694 224 9	80 288.24(10)	50 403.194 822	50 403.194 801	0.62
52.795 624 0	51.693 267 9	50 873.91(10)	50 403.848 219	50 403.848 245	-0.79
53.351 558 9	51.693 267 9	75 343.99(10)	50 404.664 453	50 404.664 443	0.31
54.763 038 5	53.691 371 2	44 227.83(10)	50 406.626 184	50 406.626 188	-0.11
55.331 564 6	53.691 371 2	66 654.24(10)	50 407.374 249	50 407.374 268	-0.60
57.058 954 5	59.685 573 4	-86 979.65(10)	50 409.511 659	50 409.511 637	0.65
59.670 694 5	58.686 577 2	31 248.46(10)	50 412.397 655	50 412.397 623	0.93
60.058 493 5	58.686 577 2	43 142.10(10)	50 412.794 384	50 412.794 348	1.08
60.293 192 0	58.686 577 2	50 225.78(10)	50 413.030 670	50 413.030 738	-2.05
60.650 308 3	59.685 573 4	29 146.52(10)	50 413.385 211	50 413.385 178	0.99
61.058 349 5	59.685 573 4	41 060.28(10)	50 413.782 611	50 413.782 573	1.14
61.286 999 1	59.685 573 4	47 629.02(10)	50 414.001 721	50 414.001 795	-2.22
62.607 585 2	61.683 468 0	25 337.93(10)	50 415.221 337	50 415.221 294	1.29
63.058 072 7	61.683 468 0	37 287.29(10)	50 415.619 924	50 415.619 875	1.48
63.275 673 9	61.683 468 0	42 963.77(10)	50 415.809 271	50 415.809 362	-2.71
63.585 247 3	61.683 468 0	50 949.20(10)	50 416.075 637	50 416.075 592	1.33
64.057 938 7	62.682 346 9	35 576.29(10)	50 416.474 734	50 416.474 681	1.57
64.270 446 9	62.682 346 9	40 864.94(10)	50 416.651 144	50 416.651 237	-2.80
64.562 262 9	62.682 346 9	48 052.49(10)	50 416.890 895	50 416.890 849	1.38
65.057 806 7	63.681 163 4	33 970.77(10)	50 417.290 436	50 417.290 380	1.65
65.265 446 3	63.681 163 4	38 904.19(10)	50 417.454 997	50 417.455 090	-2.81
65.538 640 9	63.681 163 4	45 333.94(10)	50 417.669 470	50 417.669 421	1.46
66.057 676 1	64.679 901 1	32 463.28(10)	50 418.069 385	50 418.069 322	1.89
66.260 620 1	64.679 901 1	37 069.78(10)	50 418.223 041	50 418.223 134	-2.79
66.514 397 1	64.679 901 1	42 781.05(10)	50 418.413 549	50 418.413 496	1.58
67.057 546 0	64.679 901 1	54 778.70(10)	50 418.813 747	50 418.813 681	2.00

Table XXIX: Laser spectroscopic data of the  $|\nu, L = 1, F = 3/2\rangle$  Rydberg series from three-photon laser spectroscopy as presented in Ref. [89].

$\nu_{F_c=1}$	$\tilde{\nu}_{\text{exp.}} \text{ (cm}^{-1}\text{)}$	$\tilde{\nu}_{\text{th.}} \text{ (cm}^{-1}\text{)}$	$E_{\text{exp.}} - E_{\text{th.}} \text{ (} h \cdot \text{MHz)}$	Ref.
9.066 201 1	49 110.069 61	49 108.153 006	57 458.25	[89]
9.134 588 7	49 127.481 82	49 128.068 535	-17 589.13	[89]
10.040 729 9	49 352.603 34	49 354.732 688	-63 836.24	[89]
10.061 436 7	49 360.404 48	49 359.208 359	35 858.70	[89]
11.013 410 3	49 536.393 21	49 538.507 677	-63 390.25	[89]
11.055 701 0	49 546.454 04	49 545.415 902	31 122.70	[89]
11.986 992 7	49 677.648 20	49 679.500 491	-55 530.22	[89]
12.051 503 3	49 688.494 48	49 687.654 823	25 172.18	[89]
12.946 884 4	49 786.507 30	49 788.547 553	-61 165.39	[89]
13.047 072 4	49 799.036 22	49 798.563 323	14 177.04	[89]
13.851 291 3	49 867.219 94	49 871.248 593	-120 775.88	[89]
14.041 622 7	49 886.816 33	49 886.649 352	5005.72	[89]
15.034 544 7	49 957.808 11	49 957.736 334	2151.71	[89]
15.253 671 5	49 969.183 33	49 971.584 517	-71 985.73	[89]
16.025 645 5	50 015.887 16	50 015.928 330	-1234.22	[89]
16.138 600 3	50 021.308 13	50 021.888 631	-17 403.04	[89]
17.015 531 5	50 064.155 98	50 064.197 688	-1250.48	[89]
17.101 554 0	50 067.920 72	50 068.001 112	-2410.06	[89]
18.005 097 7	50 104.689 62	50 104.714 917	-758.46	[89]
18.080 092 7	50 107.497 53	50 107.517 264	-591.48	[89]
18.994 790 6	50 139.055 45	50 139.070 223	-442.84	[89]
19.071 399 8	50 141.504 01	50 141.508 815	-143.91	[89]
19.984 633 3	50 168.444 30	50 168.453 021	-261.39	[89]
20.065 063 2	50 170.651 91	50 170.651 368	16.12	[89]
20.974 486 0	50 193.770 12	50 193.775 085	-148.94	[89]
21.060 031 5	50 195.798 60	50 195.797 431	34.90	[89]
23.942 444 3	50 251.783 99	50 251.784 859	-25.92	[89]
24.047 624 0	50 253.456 40	50 253.455 777	18.72	[89]
25.918 274 9	50 279.859 42	50 279.859 359	1.84	[89]
26.039 533 5	50 281.377 62	50 281.377 240	11.38	[89]
26.073 538 1	50 281.796 58	50 281.799 103	-75.73	[89]
30.840 619 4	50 327.843 86	50 327.843 807	1.62	[89]
31.015 842 2	50 329.143 73	50 329.143 723	0.06	[89]
31.068 415 2	50 329.526 29	50 329.529 461	-95.13	[89]
35.729 857 6	50 357.258 56	50 357.258 685	-3.85	[89]
35.984 609 6	50 358.471 57	50 358.471 463	3.08	[89]
36.065 113 2	50 358.846 45	50 358.849 376	-87.66	[89]
36.703 947 1	50 361.760 74	50 361.760 680	1.82	[89]
36.977 267 4	50 362.960 44	50 362.960 418	0.73	[89]
37.064 596 9	50 363.335 22	50 363.338 167	-88.46	[89]
37.677 235 7	50 365.914 41	50 365.914 752	-10.40	[89]
37.969 523 6	50 367.100 43	50 367.100 318	3.42	[89]
38.064 117 8	50 367.474 66	50 367.478 170	-105.29	[89]
38.650 046 7	50 369.756 83	50 369.757 157	-9.69	[89]
38.961 363 1	50 370.926 55	50 370.926 420	3.86	[89]
39.063 672 1	50 371.300 83	50 371.304 589	-112.82	[89]
39.622 741 9	50 373.319 26	50 373.319 629	-11.15	[89]
39.952 771 0	50 374.470 10	50 374.469 639	13.68	[89]
40.063 256 7	50 374.845 04	50 374.848 299	-97.80	[89]
40.595 694 0	50 376.629 52	50 376.629 946	-12.77	[89]
40.943 732 3	50 377.757 23	50 377.757 177	1.48	[89]
41.062 868 7	50 378.132 98	50 378.136 468	-104.44	[89]
46.454 707 7	50 392.366 96	50 392.367 195	-7.17	[89]
46.879 344 9	50 393.284 00	50 393.284 236	-7.17	[89]
47.060 992 8	50 393.665 20	50 393.668 961	-112.62	[89]
50.388 542 6	50 399.996 71	50 399.997 034	-9.84	[89]
50.825 830 4	50 400.737 19	50 400.737 542	-10.71	[89]
51.060 055 4	50 401.121 79	50 401.126 380	-137.57	[89]

Table XXIX (*continued*)

$\nu_{F_c=1}$	$\tilde{\nu}_{\text{exp.}} \text{ (cm}^{-1}\text{)}$	$\tilde{\nu}_{\text{th.}} \text{ (cm}^{-1}\text{)}$	$E_{\text{exp.}} - E_{\text{th.}}$ $(h \cdot \text{MHz})$	Ref.
54.341 164 5	50 406.055 61	50 406.055 834	-6.80	[89]
55.745 831 3	50 407.905 10	50 407.905 016	2.43	[89]
56.059 113 9	50 408.294 39	50 408.298 596	-126.15	[89]
56.322 692 6	50 408.624 47	50 408.624 658	-5.57	[89]

10.  $^{171}\text{Yb D } F = 3/2$ Table XXX: Laser spectroscopic data of the  $|\nu, L = 2, F = 3/2\rangle$  Rydberg series obtained from laser spectroscopy in an atomic beam setup as described in App. B.

$\nu_{F_c=1}$	$\tilde{\nu}_{\text{exp.}} \text{ (cm}^{-1}\text{)}$	$\tilde{\nu}_{\text{th.}} \text{ (cm}^{-1}\text{)}$	$E_{\text{exp.}} - E_{\text{th.}} \text{ (} h \cdot \text{MHz)}$
30.197 934 9	50 322.880 83(10)	50 322.880 692	4.04
30.249 174 5	50 323.287 55(10)	50 323.288 028	-14.39
30.287 590 2	50 323.591 84(10)	50 323.592 064	-6.63
31.192 530 5	50 330.432 60(10)	50 330.432 392	6.20
31.249 137 0	50 330.840 46(10)	50 330.840 633	-5.03
31.287 372 1	50 331.114 97(10)	50 331.115 128	-4.72
32.186 771 4	50 337.292 67(10)	50 337.292 579	2.59
32.249 105 6	50 337.701 66(10)	50 337.701 667	-0.29
32.287 186 8	50 337.950 41(10)	50 337.950 422	-0.30
33.180 645 4	50 343.543 27(10)	50 343.543 170	3.04
33.249 079 1	50 343.953 06(10)	50 343.953 050	0.20
33.287 026 2	50 344.179 13(10)	50 344.179 243	-3.41
34.174 140 5	50 349.254 37(10)	50 349.254 303	2.01
34.249 056 7	50 349.665 13(10)	50 349.664 923	6.13
34.286 885 0	50 349.871 17(10)	50 349.871 240	-2.15
35.167 245 2	50 354.486 27(10)	50 354.486 314	-1.38
35.249 037 6	50 354.897 60(10)	50 354.897 622	-0.56
35.286 759 4	50 355.086 38(10)	50 355.086 350	1.00
36.159 948 0	50 359.291 46(10)	50 359.291 332	3.84
36.249 021 4	50 359.703 48(10)	50 359.703 282	6.01
36.286 646 7	50 359.876 52(10)	50 359.876 383	4.17
37.152 237 5	50 363.714 59(10)	50 363.714 586	-0.02
37.249 007 5	50 364.127 38(10)	50 364.127 134	7.37
37.286 544 8	50 364.286 31(10)	50 364.286 299	0.31
38.144 102 4	50 367.795 59(10)	50 367.795 474	3.49
38.248 995 7	50 368.208 68(10)	50 368.208 578	3.04
39.135 531 7	50 371.568 53(10)	50 371.568 436	2.95
39.248 985 5	50 371.982 19(10)	50 371.982 057	4.03
39.286 367 6	50 372.117 55(10)	50 372.117 558	-0.14
40.126 514 2	50 375.063 67(10)	50 375.063 691	-0.71
40.248 976 7	50 375.478 08(10)	50 375.477 793	8.74
41.117 038 9	50 378.307 78(10)	50 378.307 839	-1.86
41.286 218 5	50 378.838 68(10)	50 378.838 713	-0.87
42.107 094 8	50 381.324 30(10)	50 381.324 369	-2.11
42.286 152 5	50 381.847 48(10)	50 381.847 423	1.55
43.096 670 9	50 384.134 05(10)	50 384.134 088	-1.20
43.286 091 4	50 384.650 08(10)	50 384.650 056	0.60
44.085 756 5	50 386.755 44(10)	50 386.755 479	-1.31
44.286 034 5	50 387.265 05(10)	50 387.265 009	1.34
45.074 340 5	50 389.204 89(10)	50 389.205 003	-3.36
45.285 981 5	50 389.708 69(10)	50 389.708 671	0.58
45.285 981 5	50 389.708 69(10)	50 389.708 671	0.67
46.062 412 2	50 391.497 22(10)	50 391.497 363	-4.32
46.285 932 0	50 391.995 68(10)	50 391.995 681	-0.09
47.049 960 8	50 393.645 59(10)	50 393.645 722	-3.95
47.285 885 6	50 394.139 16(10)	50 394.139 148	0.36
48.036 975 5	50 395.661 77(10)	50 395.661 894	-3.79
48.285 842 0	50 396.150 90(10)	50 396.150 836	1.78
49.023 445 5	50 397.556 34(10)	50 397.556 505	-5.07
49.285 800 9	50 398.041 36(10)	50 398.041 331	0.79
50.285 762 2	50 399.820 17(10)	50 399.820 175	-0.04
50.994 708 8	50 401.018 30(10)	50 401.018 437	-4.13
51.285 725 5	50 401.496 01(10)	50 401.495 988	0.72
51.979 480 8	50 402.602 16(10)	50 402.602 246	-2.45
52.285 690 6	50 403.076 66(10)	50 403.076 577	2.56



Table XXX (*continued*)

$\nu_{F_c=1}$	$\tilde{\nu}_{\text{exp.}} \text{ (cm}^{-1}\text{)}$	$\tilde{\nu}_{\text{th.}} \text{ (cm}^{-1}\text{)}$	$E_{\text{exp.}} - E_{\text{th.}}$ ( $h \cdot \text{MHz}$ )
52.963 665 6	50 404.097 48(10)	50 404.097 668	-5.78
53.285 657 4	50 404.569 00(10)	50 404.569 022	-0.52
53.947 252 5	50 405.511 00(10)	50 405.511 159	-4.66
54.285 625 7	50 405.979 77(10)	50 405.979 756	0.50
54.930 231 0	50 406.848 30(10)	50 406.848 597	-8.95
55.285 595 4	50 407.314 70(10)	50 407.314 637	1.76
55.912 590 7	50 408.115 18(10)	50 408.115 341	-4.67
56.285 566 2	50 408.579 03(10)	50 408.579 007	0.75
56.894 321 0	50 409.316 19(10)	50 409.316 288	-2.91
57.285 538 0	50 409.777 83(10)	50 409.777 746	2.47
57.875 411 5	50 410.455 78(10)	50 410.455 916	-4.08
58.285 510 6	50 410.915 39(10)	50 410.915 318	2.20
58.855 851 9	50 411.538 23(10)	50 411.538 331	-3.05
59.285 484 0	50 411.995 86(10)	50 411.995 815	1.24
59.835 631 8	50 412.567 36(10)	50 412.567 300	1.84
60.285 458 0	50 413.023 11(10)	50 413.022 992	3.38
60.814 740 9	50 413.546 22(10)	50 413.546 283	-1.95
61.285 432 4	50 414.000 32(10)	50 414.000 301	0.56
61.793 168 9	50 414.478 33(10)	50 414.478 467	-4.01
62.285 407 0	50 414.931 00(10)	50 414.930 918	2.46
62.770 905 7	50 415.366 84(10)	50 415.366 788	1.53
63.285 381 7	50 415.817 80(10)	50 415.817 770	0.95
63.747 941 1	50 416.213 86(10)	50 416.213 955	-2.73
64.285 356 2	50 416.663 54(10)	50 416.663 559	-0.41
64.724 265 1	50 417.022 31(10)	50 417.022 473	-4.98
65.285 330 3	50 417.470 86(10)	50 417.470 781	2.28
65.285 330 3	50 417.470 97(10)	50 417.470 781	5.69
65.699 867 8	50 417.794 43(10)	50 417.794 657	-6.87
66.285 303 6	50 418.241 77(10)	50 418.241 746	0.79
66.674 739 1	50 418.532 48(10)	50 418.532 652	-5.02
67.285 275 9	50 418.978 58(10)	50 418.978 592	-0.32
67.648 869 5	50 419.238 37(10)	50 419.238 447	-2.18
68.285 246 5	50 419.683 26(10)	50 419.683 304	-1.32
68.622 249 3	50 419.913 72(10)	50 419.913 889	-5.21
69.285 214 7	50 420.357 74(10)	50 420.357 723	0.59
69.594 869 2	50 420.560 58(10)	50 420.560 694	-3.45
70.285 179 5	50 421.003 61(10)	50 421.003 559	1.58
70.566 720 2	50 421.180 30(10)	50 421.180 459	-4.64
71.285 139 5	50 421.622 38(10)	50 421.622 404	-0.66
71.537 794 0	50 421.774 53(10)	50 421.774 672	-4.17
72.285 092 2	50 422.215 69(10)	50 422.215 741	-1.52
72.508 083 0	50 422.344 57(10)	50 422.344 720	-4.64
73.285 033 6	50 422.784 97(10)	50 422.784 950	0.49
73.477 581 5	50 422.891 79(10)	50 422.891 897	-3.29
74.284 956 6	50 423.331 28(10)	50 423.331 318	-1.01
74.446 287 1	50 423.417 25(10)	50 423.417 414	-5.07
75.284 846 2	50 423.856 01(10)	50 423.856 043	-1.02
75.284 846 2	50 423.856 10(10)	50 423.856 043	1.81
75.414 205 4	50 423.922 26(10)	50 423.922 408	-4.46
76.284 666 5	50 424.360 19(10)	50 424.360 237	-1.51
76.381 363 3	50 424.407 80(10)	50 424.407 952	-4.55
77.284 303 9	50 424.844 89(10)	50 424.844 902	-0.27
77.347 867 3	50 424.874 96(10)	50 424.875 086	-3.74
78.283 134 5	50 425.310 76(10)	50 425.310 750	0.17
78.314 338 9	50 425.324 77(10)	50 425.325 017	-7.38
79.289 989 0	50 425.762 45(10)	50 425.762 636	-5.49
80.286 622 2	50 426.193 32(10)	50 426.193 296	0.72
81.286 011 2	50 426.609 29(10)	50 426.609 338	-1.44
82.285 761 0	50 427.010 47(10)	50 427.010 455	0.51

Table XXX (*continued*)

$\nu_{F_c=1}$	$\tilde{\nu}_{\text{exp.}} \text{ (cm}^{-1}\text{)}$	$\tilde{\nu}_{\text{th.}} \text{ (cm}^{-1}\text{)}$	$E_{\text{exp.}} - E_{\text{th.}}$ ( $h \cdot \text{MHz}$ )
83.285 621 2	50 427.397 20(10)	50 427.397 257	-1.81
84.285 529 1	50 427.770 31(10)	50 427.770 392	-2.37
85.285 461 5	50 428.130 45(10)	50 428.130 489	-1.08
86.285 408 1	50 428.478 12(10)	50 428.478 144	-0.59
87.285 363 3	50 428.814 03(10)	50 428.813 922	3.21
88.285 323 7	50 429.138 38(10)	50 429.138 357	0.67
89.285 287 3	50 429.452 06(10)	50 429.451 954	3.32
90.285 252 3	50 429.755 19(10)	50 429.755 189	0.10
91.285 217 2	50 430.048 59(10)	50 430.048 513	2.30
92.285 180 5	50 430.332 36(10)	50 430.332 354	0.33
93.285 140 0	50 430.607 08(10)	50 430.607 115	-1.14
94.285 092 7	50 430.873 12(10)	50 430.873 178	-1.88
95.285 032 9	50 431.130 86(10)	50 431.130 906	-1.30
96.284 949 3	50 431.380 55(10)	50 431.380 640	-2.57
97.284 812 5	50 431.622 64(10)	50 431.622 701	-1.92
98.284 518 2	50 431.857 36(10)	50 431.857 375	-0.43
99.283 241 4	50 432.084 87(10)	50 432.084 776	2.75
101.285 898 2	50 432.520 63(10)	50 432.520 663	-1.07
102.285 595 3	50 432.728 74(10)	50 432.728 734	0.12
103.285 455 0	50 432.930 82(10)	50 432.930 825	-0.25
104.285 368 3	50 433.127 14(10)	50 433.127 141	-0.12
105.285 304 9	50 433.317 96(10)	50 433.317 895	1.88
106.285 252 6	50 433.503 29(10)	50 433.503 293	-0.04
107.285 204 9	50 433.683 53(10)	50 433.683 531	0.04
108.285 157 2	50 433.858 82(10)	50 433.858 800	0.48
109.285 104 3	50 434.029 29(10)	50 434.029 278	0.42
110.285 038 7	50 434.195 24(10)	50 434.195 139	2.93
111.284 943 5	50 434.356 60(10)	50 434.356 543	1.80
112.284 767 4	50 434.513 64(10)	50 434.513 643	0.04
113.284 220 1	50 434.666 57(10)	50 434.666 545	0.83
115.285 838 0	50 434.960 95(10)	50 434.960 894	1.54
116.285 506 9	50 435.102 28(10)	50 435.102 243	1.25
117.285 369 0	50 435.240 03(10)	50 435.240 019	0.32
118.285 284 4	50 435.374 33(10)	50 435.374 322	0.33
119.285 219 6	50 435.505 27(10)	50 435.505 265	0.15
120.285 160 7	50 435.632 93(10)	50 435.632 957	-0.72

11.  $^{171}\text{Yb D } F = 5/2$ Table XXXI: Laser spectroscopic data of the  $|\nu, L = 2, F = 5/2\rangle$  Rydberg series obtained from laser spectroscopy in an atomic beam setup as described in App. B.

$\nu_{F_c=1}$	$\tilde{\nu}_{\text{exp.}} \text{ (cm}^{-1}\text{)}$	$\tilde{\nu}_{\text{th.}} \text{ (cm}^{-1}\text{)}$	$E_{\text{exp.}} - E_{\text{th.}} \text{ (h} \cdot \text{MHz)}$
30.222 107 4	50 323.072 99(10)	50 323.073 113	-3.70
30.252 825 3	50 323.317 48(10)	50 323.316 972	15.23
30.283 070 3	50 323.556 42(10)	50 323.556 352	2.19
31.216 835 8	50 330.607 84(10)	50 330.607 951	-3.38
31.252 726 5	50 330.866 82(10)	50 330.866 445	11.16
31.282 833 3	50 331.082 77(10)	50 331.082 596	5.25
32.211 179 5	50 337.453 09(10)	50 337.453 048	1.35
32.252 647 9	50 337.725 13(10)	50 337.724 843	8.48
32.282 633 5	50 337.920 79(10)	50 337.920 725	1.82
33.205 133 3	50 343.690 06(10)	50 343.690 130	-2.01
33.252 583 9	50 343.973 97(10)	50 343.973 974	0.01
33.282 462 1	50 344.152 15(10)	50 344.152 079	2.04
34.198 690 4	50 349.389 14(10)	50 349.389 160	-0.62
34.252 530 9	50 349.684 00(10)	50 349.683 900	2.94
34.282 313 2	50 349.846 31(10)	50 349.846 341	-1.01
35.191 843 0	50 354.610 33(10)	50 354.610 310	0.69
35.252 486 4	50 354.914 97(10)	50 354.914 902	2.13
35.282 182 6	50 355.063 43(10)	50 355.063 484	-1.53
36.184 582 3	50 359.405 73(10)	50 359.405 566	4.98
36.252 448 5	50 359.719 20(10)	50 359.719 071	3.99
36.282 067 0	50 359.855 30(10)	50 359.855 342	-1.34
37.176 899 2	50 363.820 04(10)	50 363.820 030	0.44
37.252 415 8	50 364.141 70(10)	50 364.141 606	2.87
37.281 964 1	50 364.267 03(10)	50 364.266 902	3.98
38.168 784 2	50 367.893 01(10)	50 367.892 985	0.87
38.252 387 5	50 368.221 71(10)	50 368.221 879	-5.18
38.281 871 9	50 368.337 20(10)	50 368.337 357	-4.67
39.160 227 4	50 371.658 89(10)	50 371.658 776	3.37
39.252 362 6	50 371.994 16(10)	50 371.994 314	-4.72
39.281 788 8	50 372.100 87(10)	50 372.100 982	-3.31
40.151 218 9	50 375.147 57(10)	50 375.147 534	1.06
40.252 340 7	50 375.488 97(10)	50 375.489 115	-4.44
40.281 713 6	50 375.587 71(10)	50 375.587 852	-4.11
41.141 748 4	50 378.385 76(10)	50 378.385 784	-0.60
41.252 321 2	50 378.732 71(10)	50 378.732 868	-4.61
41.281 645 2	50 378.824 38(10)	50 378.824 448	-1.95
42.131 805 8	50 381.396 99(10)	50 381.396 950	1.17
42.252 303 7	50 381.748 93(10)	50 381.749 055	-3.83
42.281 582 8	50 381.834 05(10)	50 381.834 157	-3.21
43.121 380 5	50 384.201 83(10)	50 384.201 781	1.54
43.252 288 0	50 384.558 36(10)	50 384.558 475	-3.58
43.281 525 6	50 384.637 59(10)	50 384.637 699	-3.21
44.110 462 1	50 386.818 74(10)	50 386.818 708	1.01
44.252 273 8	50 387.179 49(10)	50 387.179 602	-3.26
44.281 473 1	50 387.253 39(10)	50 387.253 481	-2.62
45.099 040 2	50 389.264 30(10)	50 389.264 149	4.53
45.252 260 9	50 389.628 75(10)	50 389.628 895	-4.43
45.281 424 5	50 389.697 75(10)	50 389.697 900	-4.46
46.087 104 2	50 391.552 86(10)	50 391.552 768	2.78
46.252 249 1	50 391.920 91(10)	50 391.921 050	-4.22
46.281 379 6	50 391.985 44(10)	50 391.985 604	-5.00
47.074 643 6	50 393.697 80(10)	50 393.697 693	3.28
47.252 238 2	50 394.069 09(10)	50 394.069 227	-4.08
47.281 337 8	50 394.129 54(10)	50 394.129 706	-5.05
48.061 647 8	50 395.710 75(10)	50 395.710 707	1.20

Table XXXI (*continued*)

$\nu_{F_c=1}$	$\tilde{\nu}_{\text{exp.}} \text{ (cm}^{-1}\text{)}$	$\tilde{\nu}_{\text{th.}} \text{ (cm}^{-1}\text{)}$	$E_{\text{exp.}} - E_{\text{th.}}$ ( $h \cdot \text{MHz}$ )
48.252 228 2	50 396.085 12(10)	50 396.085 238	-3.56
48.281 298 9	50 396.141 85(10)	50 396.141 978	-3.88
49.048 106 2	50 397.602 47(10)	50 397.602 409	1.96
49.252 218 9	50 397.979 58(10)	50 397.979 705	-3.74
49.281 262 5	50 398.032 86(10)	50 398.033 010	-4.49
50.034 008 4	50 399.382 47(10)	50 399.382 355	3.55
50.252 210 3	50 399.762 11(10)	50 399.762 205	-2.78
50.281 228 4	50 399.812 28(10)	50 399.812 348	-2.04
51.019 343 7	50 401.059 20(10)	50 401.059 179	0.61
51.252 202 3	50 401.441 26(10)	50 401.441 392	-4.03
51.281 196 3	50 401.488 49(10)	50 401.488 618	-3.91
52.004 101 7	50 402.640 73(10)	50 402.640 695	1.16
52.252 194 7	50 403.024 98(10)	50 403.025 097	-3.54
52.281 165 9	50 403.069 53(10)	50 403.069 629	-3.11
52.988 271 7	50 404.134 02(10)	50 404.133 992	0.96
53.252 187 6	50 404.520 31(10)	50 404.520 425	-3.33
53.281 137 2	50 404.562 30(10)	50 404.562 464	-4.85
53.971 843 3	50 405.545 57(10)	50 405.545 511	1.83
54.252 180 9	50 405.933 69(10)	50 405.933 830	-4.31
54.281 109 9	50 405.973 46(10)	50 405.973 560	-3.08
54.954 806 1	50 406.881 24(10)	50 406.881 117	3.71
55.252 174 5	50 407.271 09(10)	50 407.271 190	-2.87
55.281 083 8	50 407.308 66(10)	50 407.308 777	-3.43
55.937 149 4	50 408.146 25(10)	50 408.146 157	2.77
56.252 168 3	50 408.537 77(10)	50 408.537 864	-2.69
56.281 058 8	50 408.573 36(10)	50 408.573 459	-2.99
56.918 863 1	50 409.345 49(10)	50 409.345 516	-0.78
57.252 162 5	50 409.738 58(10)	50 409.738 747	-4.97
57.281 034 7	50 409.772 38(10)	50 409.772 488	-3.19
57.899 936 5	50 410.483 64(10)	50 410.483 664	-0.85
58.252 156 8	50 410.878 15(10)	50 410.878 316	-5.02
58.281 011 5	50 410.910 23(10)	50 410.910 330	-3.12
58.880 359 5	50 411.564 71(10)	50 411.564 697	0.37
59.252 151 3	50 411.960 57(10)	50 411.960 677	-3.22
59.280 988 9	50 411.990 93(10)	50 411.991 080	-4.62
59.860 121 6	50 412.592 41(10)	50 412.592 374	1.01
60.252 145 9	50 412.989 48(10)	50 412.989 595	-3.55
60.280 966 8	50 413.018 42(10)	50 413.018 493	-2.28
60.839 212 6	50 413.570 18(10)	50 413.570 148	1.01
61.252 140 6	50 413.968 47(10)	50 413.968 532	-2.01
61.280 945 2	50 413.995 91(10)	50 413.996 022	-3.48
61.817 622 3	50 414.501 21(10)	50 414.501 199	0.39
62.252 135 4	50 414.900 51(10)	50 414.900 673	-4.99
62.280 923 7	50 414.926 76(10)	50 414.926 845	-2.58
62.795 340 5	50 415.388 44(10)	50 415.388 458	-0.54
63.252 130 2	50 415.788 85(10)	50 415.788 954	-3.01
63.280 902 4	50 415.813 80(10)	50 415.813 891	-2.70
63.772 357 0	50 416.234 62(10)	50 416.234 629	-0.29
64.252 125 0	50 416.635 95(10)	50 416.636 084	-4.15
64.280 880 9	50 416.659 71(10)	50 416.659 861	-4.38
64.748 661 8	50 417.042 16(10)	50 417.042 209	-1.41
65.252 119 6	50 417.444 49(10)	50 417.444 566	-2.28
65.280 859 2	50 417.467 13(10)	50 417.467 254	-3.65
65.724 245 0	50 417.813 50(10)	50 417.813 512	-0.29
66.252 114 2	50 418.216 64(10)	50 418.216 716	-2.39
66.280 836 8	50 418.238 32(10)	50 418.238 379	-1.76
66.699 096 6	50 418.550 70(10)	50 418.550 677	0.64
67.252 108 5	50 418.954 62(10)	50 418.954 678	-1.68
67.280 813 7	50 418.975 27(10)	50 418.975 377	-3.19

Table XXXI (*continued*)

$\nu_{F_c=1}$	$\tilde{\nu}_{\text{exp.}} \text{ (cm}^{-1}\text{)}$	$\tilde{\nu}_{\text{th.}} \text{ (cm}^{-1}\text{)}$	$E_{\text{exp.}} - E_{\text{th.}}$ ( $h \cdot \text{MHz}$ )
67.673 206 8	50 419.255 69(10)	50 419.255 691	0.06
68.252 102 5	50 419.660 33(10)	50 419.660 442	-3.31
68.280 789 2	50 419.680 10(10)	50 419.680 232	-3.88
68.646 566 1	50 419.930 42(10)	50 419.930 396	0.65
69.252 096 1	50 420.335 80(10)	50 420.335 853	-1.52
69.280 763 1	50 420.354 69(10)	50 420.354 785	-2.94
69.619 165 0	50 420.576 50(10)	50 420.576 505	-0.19
70.252 089 0	50 420.982 52(10)	50 420.982 627	-3.11
70.280 734 4	50 421.000 64(10)	50 421.000 749	-3.24
70.590 994 4	50 421.195 61(10)	50 421.195 613	-0.23
71.252 081 2	50 421.602 33(10)	50 421.602 361	-0.89
71.280 702 2	50 421.619 68(10)	50 421.619 716	-0.99
71.562 045 5	50 421.789 30(10)	50 421.789 203	2.80
72.280 664 9	50 422.213 11(10)	50 422.213 168	-1.73
72.532 310 3	50 422.358 80(10)	50 422.358 661	4.03
73.252 061 6	50 422.766 61(10)	50 422.766 552	1.61
73.280 620 0	50 422.782 50(10)	50 422.782 489	0.36
73.501 781 9	50 422.905 36(10)	50 422.905 279	2.45
74.252 048 5	50 423.313 63(10)	50 423.313 687	-1.77
74.280 563 4	50 423.328 93(10)	50 423.328 966	-1.21
74.470 455 4	50 423.430 22(10)	50 423.430 264	-1.21
75.252 031 5	50 423.839 07(10)	50 423.839 154	-2.59
75.280 487 2	50 423.853 70(10)	50 423.853 801	-2.93
75.438 330 4	50 423.934 77(10)	50 423.934 747	0.66
76.252 007 8	50 424.344 01(10)	50 424.344 080	-2.08
76.280 374 9	50 424.358 04(10)	50 424.358 115	-2.36
76.405 416 4	50 424.419 80(10)	50 424.419 793	0.24
77.251 971 2	50 424.829 45(10)	50 424.829 519	-2.15
77.280 184 9	50 424.842 88(10)	50 424.842 943	-1.76
77.371 751 4	50 424.886 42(10)	50 424.886 409	0.29
78.251 905 0	50 425.296 40(10)	50 425.296 454	-1.73
78.279 774 3	50 425.309 11(10)	50 425.309 213	-3.15
78.337 485 4	50 425.335 47(10)	50 425.335 589	-3.49
79.251 740 1	50 425.745 63(10)	50 425.745 784	-4.75
79.278 197 6	50 425.757 36(10)	50 425.757 443	-2.52
79.303 623 3	50 425.768 67(10)	50 425.768 637	1.08
80.250 590 1	50 426.178 04(10)	50 426.178 005	0.98
80.262 526 9	50 426.183 10(10)	50 426.183 073	0.70
80.283 970 1	50 426.192 17(10)	50 426.192 171	-0.15
81.225 075 3	50 426.584 48(10)	50 426.584 409	2.10
81.252 738 0	50 426.595 57(10)	50 426.595 733	-5.00
81.281 919 7	50 426.607 59(10)	50 426.607 666	-2.27
82.187 661 7	50 426.971 84(10)	50 426.971 743	2.94
82.252 375 3	50 426.997 22(10)	50 426.997 296	-2.40
82.281 452 5	50 427.008 68(10)	50 427.008 758	-2.26
83.148 828 5	50 427.345 16(10)	50 427.345 161	-0.15
83.252 273 1	50 427.384 60(10)	50 427.384 580	0.53
83.281 245 7	50 427.395 58(10)	50 427.395 594	-0.44
84.108 947 0	50 427.705 42(10)	50 427.705 463	-1.20
84.252 223 8	50 427.758 17(10)	50 427.758 177	-0.30
84.281 125 8	50 427.768 78(10)	50 427.768 778	0.17
85.068 089 3	50 428.053 27(10)	50 428.053 287	-0.39
85.252 193 9	50 428.118 57(10)	50 428.118 712	-4.34
85.281 045 2	50 428.128 89(10)	50 428.128 926	-1.21
86.026 274 8	50 428.389 21(10)	50 428.389 213	-0.07
86.252 173 2	50 428.466 69(10)	50 428.466 783	-2.72
86.280 985 2	50 428.476 54(10)	50 428.476 633	-2.71
86.983 507 1	50 428.713 79(10)	50 428.713 780	0.34
87.252 157 5	50 428.802 96(10)	50 428.802 957	0.25

Table XXXI (*continued*)

$\nu_{F_c=1}$	$\tilde{\nu}_{\text{exp.}} \text{ (cm}^{-1}\text{)}$	$\tilde{\nu}_{\text{th.}} \text{ (cm}^{-1}\text{)}$	$E_{\text{exp.}} - E_{\text{th.}}$ ( $h \cdot \text{MHz}$ )
87.280 937 2	50 428.812 42(10)	50 428.812 461	-1.38
87.939 783 8	50 429.027 55(10)	50 429.027 498	1.47
88.252 144 7	50 429.127 71(10)	50 429.127 769	-1.85
88.280 896 5	50 429.136 80(10)	50 429.136 945	-4.43
88.895 099 5	50 429.330 80(10)	50 429.330 846	-1.51
89.252 133 7	50 429.441 72(10)	50 429.441 725	-0.18
89.280 860 2	50 429.450 52(10)	50 429.450 588	-2.01
89.849 447 9	50 429.624 27(10)	50 429.624 277	-0.21
90.252 123 8	50 429.745 23(10)	50 429.745 304	-2.29
90.280 826 3	50 429.753 70(10)	50 429.753 869	-4.99
90.802 821 7	50 429.908 30(10)	50 429.908 220	2.43
91.252 114 3	50 430.039 01(10)	50 430.038 957	1.69
91.280 793 3	50 430.047 17(10)	50 430.047 237	-1.88
91.755 213 8	50 430.183 19(10)	50 430.183 078	3.49
92.252 104 8	50 430.323 07(10)	50 430.323 113	-1.16
92.280 759 6	50 430.331 06(10)	50 430.331 119	-1.70
92.706 616 8	50 430.449 24(10)	50 430.449 237	0.13
93.252 094 9	50 430.598 11(10)	50 430.598 176	-2.01
93.280 723 5	50 430.605 81(10)	50 430.605 921	-3.47
93.657 023 8	50 430.707 07(10)	50 430.707 060	0.41
94.252 084 0	50 430.864 48(10)	50 430.864 531	-1.52
94.280 682 6	50 430.871 96(10)	50 430.872 024	-1.89
94.606 428 9	50 430.956 93(10)	50 430.956 892	1.24
95.252 071 1	50 431.122 50(10)	50 431.122 540	-1.20
95.280 632 9	50 431.129 69(10)	50 431.129 790	-3.02
95.554 828 1	50 431.199 09(10)	50 431.199 062	0.75
96.252 054 7	50 431.372 42(10)	50 431.372 549	-3.75
96.252 054 7	50 431.372 53(10)	50 431.372 549	-0.52
96.280 567 1	50 431.379 50(10)	50 431.379 563	-2.02
96.280 567 1	50 431.379 51(10)	50 431.379 563	-1.69
96.502 221 6	50 431.433 82(10)	50 431.433 881	-1.87
96.502 221 6	50 431.433 88(10)	50 431.433 881	0.02
97.252 031 4	50 431.614 74(10)	50 431.614 883	-4.25
97.252 031 4	50 431.614 85(10)	50 431.614 883	-1.06
97.280 468 0	50 431.621 57(10)	50 431.621 665	-2.80
97.280 468 0	50 431.621 62(10)	50 431.621 665	-1.45
97.448 621 0	50 431.661 58(10)	50 431.661 649	-2.01
97.448 621 0	50 431.661 64(10)	50 431.661 649	-0.18
98.251 992 7	50 431.849 76(10)	50 431.849 853	-2.73
98.251 992 7	50 431.849 82(10)	50 431.849 853	-1.10
98.280 285 8	50 431.856 33(10)	50 431.856 397	-1.97
98.280 285 8	50 431.856 44(10)	50 431.856 397	1.19
98.394 076 2	50 431.882 58(10)	50 431.882 659	-2.53
98.394 076 2	50 431.882 72(10)	50 431.882 659	1.95
99.251 906 5	50 432.077 99(10)	50 432.077 746	7.37
99.279 781 8	50 432.084 12(10)	50 432.084 000	3.66
99.338 849 1	50 432.097 28(10)	50 432.097 236	1.30
100.251 477 0	50 432.298 78(10)	50 432.298 779	0.03
100.273 489 7	50 432.303 62(10)	50 432.303 572	1.50
100.288 693 5	50 432.306 97(10)	50 432.306 881	2.67
101.221 297 3	50 432.507 02(10)	50 432.507 005	0.35
101.252 644 8	50 432.513 62(10)	50 432.513 636	-0.36
101.281 772 3	50 432.519 83(10)	50 432.519 792	1.05
102.163 149 0	50 432.703 64(10)	50 432.703 577	1.83
102.252 290 9	50 432.721 89(10)	50 432.721 900	-0.35
102.281 251 8	50 432.727 83(10)	50 432.727 843	-0.30
103.103 307 4	50 432.894 46(10)	50 432.894 447	0.25
103.252 210 8	50 432.924 18(10)	50 432.924 200	-0.54
103.281 065 4	50 432.929 90(10)	50 432.929 950	-1.65

Table XXXI (*continued*)

$\nu_{F_c=1}$	$\tilde{\nu}_{\text{exp.}} \text{ (cm}^{-1}\text{)}$	$\tilde{\nu}_{\text{th.}} \text{ (cm}^{-1}\text{)}$	$E_{\text{exp.}} - E_{\text{th.}}$ ( $h \cdot \text{MHz}$ )
104.042 245 0	50 433.080 00(10)	50 433.079 928	2.05
104.252 173 3	50 433.120 61(10)	50 433.120 714	-3.07
104.280 963 4	50 433.126 33(10)	50 433.126 289	1.35
104.980 033 3	50 433.260 23(10)	50 433.260 237	-0.25
105.252 150 0	50 433.311 65(10)	50 433.311 657	-0.20
105.280 894 3	50 433.317 19(10)	50 433.317 066	3.73
105.916 689 7	50 433.435 55(10)	50 433.435 569	-0.48
106.252 132 8	50 433.497 15(10)	50 433.497 236	-2.51
106.280 840 4	50 433.502 54(10)	50 433.502 486	1.57
106.852 217 1	50 433.606 15(10)	50 433.606 107	1.23
107.252 118 6	50 433.677 70(10)	50 433.677 648	1.55
107.280 793 4	50 433.682 72(10)	50 433.682 747	-0.95
107.786 613 7	50 433.772 11(10)	50 433.772 026	2.62
108.252 105 4	50 433.853 26(10)	50 433.853 084	5.28
108.280 748 2	50 433.858 15(10)	50 433.858 038	3.43
108.719 876 1	50 433.933 45(10)	50 433.933 492	-1.28
109.252 091 9	50 434.023 71(10)	50 434.023 725	-0.36
109.280 700 3	50 434.028 84(10)	50 434.028 538	9.02
109.652 001 1	50 434.090 79(10)	50 434.090 663	3.79
110.252 076 6	50 434.190 07(10)	50 434.189 743	9.95
110.280 643 6	50 434.194 57(10)	50 434.194 419	4.53
110.582 987 7	50 434.243 91(10)	50 434.243 692	6.48
111.252 056 9	50 434.351 71(10)	50 434.351 304	12.18
111.280 566 5	50 434.355 94(10)	50 434.355 846	2.71
111.512 841 8	50 434.392 76(10)	50 434.392 725	0.96
112.252 026 6	50 434.508 49(10)	50 434.508 565	-2.16
112.280 438 5	50 434.512 98(10)	50 434.512 972	0.22
112.441 592 2	50 434.538 11(10)	50 434.537 905	6.11
113.251 964 3	50 434.661 75(10)	50 434.661 674	2.35
113.280 130 5	50 434.665 92(10)	50 434.665 928	-0.11
113.369 381 4	50 434.679 55(10)	50 434.679 387	5.02
114.251 695 9	50 434.810 84(10)	50 434.810 750	2.71
114.277 548 2	50 434.814 58(10)	50 434.814 553	0.84
114.298 470 0	50 434.817 83(10)	50 434.817 629	5.99
115.218 487 8	50 434.951 39(10)	50 434.951 239	4.61
115.281 686 3	50 434.960 32(10)	50 434.960 300	0.47
116.143 219 2	50 435.082 43(10)	50 435.082 346	2.46
116.281 146 8	50 435.101 88(10)	50 435.101 634	7.47
117.066 107 8	50 435.210 28(10)	50 435.210 107	5.06
117.280 975 1	50 435.239 53(10)	50 435.239 421	3.20